



Irradiation-assisted Stress Corrosion Cracking of PWR Irradiated Type 347 Stainless Steel (NSUF CINR 19-16567)

September 2023

Changing the World's Energy Future

Micheal R. Ickes, Gary S. Was, Kai Sun, Abdullah Sinjilawi, Lijin Dong



INL is a U.S. Department of Energy National Laboratory operated by Battelle Energy Alliance, LLC

DISCLAIMER

This information was prepared as an account of work sponsored by an agency of the U.S. Government. Neither the U.S. Government nor any agency thereof, nor any of their employees, makes any warranty, expressed or implied, or assumes any legal liability or responsibility for the accuracy, completeness, or usefulness, of any information, apparatus, product, or process disclosed, or represents that its use would not infringe privately owned rights. References herein to any specific commercial product, process, or service by trade name, trade mark, manufacturer, or otherwise, does not necessarily constitute or imply its endorsement, recommendation, or favoring by the U.S. Government or any agency thereof. The views and opinions of authors expressed herein do not necessarily state or reflect those of the U.S. Government or any agency thereof.

Irradiation-assisted Stress Corrosion Cracking of PWRirradiated Type 347 Stainless Steel (NSUF CINR 19-16567)

Micheal R. Ickes, Gary S. Was, Kai Sun, Abdullah Sinjilawi, Lijin Dong

September 2023

**Idaho National Laboratory
Idaho Falls, Idaho 83415**

<http://www.inl.gov>

**Prepared for the
U.S. Department of Energy
Under DOE Idaho Operations Office
Contract DE-AC07-05ID14517**

Irradiation-assisted Stress Corrosion Cracking of PWR- irradiated Type 347 Stainless Steel

Final Report for NSUF Project 19-16567



RT-TR-22-25
Revision 0

Irradiation-assisted Stress Corrosion Cracking of PWR-irradiated Type 347 Stainless Steel

Michael R. Ickes*
Westinghouse Electric Company - Materials & Chemistry

Gary S. Was
University of Michigan

Kai Sun
University of Michigan

Abdullah Sinjlawi
University of Michigan

Lijin Dong
University of Michigan

September 2022

Reviewer: Raymond Simmen*
Westinghouse Electric Company - Materials & Chemistry

Approved: John Lyons*, Manager
Westinghouse Electric Company - Materials & Chemistry

This document may contain technical data subject to the export control laws of the United States. In the event that this document does contain such information, the Recipient's acceptance of this document constitutes agreement that this information in document form (or any other medium), including any attachments and exhibits hereto, shall not be exported, released or disclosed to foreign persons whether in the United States or abroad by recipient except in compliance with all U.S. export control regulations. Recipient shall include this notice with any reproduced or excerpted portion of this document or any document derived from, based on, incorporating, using or relying on the information contained in this document.

*Electronically approved records are authenticated in the electronic document management system.

Westinghouse Electric Company LLC
1000 Westinghouse Drive
Cranberry Township, PA 16066, USA

© 2022 Westinghouse Electric Company LLC
All Rights Reserved

TABLE OF CONTENTS

LIST OF TABLES	iv
LIST OF FIGURES	v
Acronyms & Abbreviations	xi
1 EXECUTIVE SUMMARY	1-1
2 BACKGROUND AND MOTIVATION	2-1
3 SPECIMEN MATERIAL AND FABRICATION	3-1
4 METHODOLOGY	4-1
4.1 IASCC INITIATION TESTING / 4-POINT BEND INTERRUPTED TEST	4-1
4.2 SCANNING ELECTRON MICROSCOPY CHARACTERIZATION OF CRACK INITIATION	4-3
4.3 OXIDE THICKNESS ROLE ON THE IASCC QUANTIFICATION	4-3
4.4 FINITE ELEMENT ANALYSIS (FEA)	4-3
4.5 TESTING SYSTEMS	4-4
4.6 INITIATION STRESS DETERMINATION AND THE CRACKING CRITERIA	4-5
4.7 TRANSMISSION ELECTRON MICROSCOPY ANALYSIS OF IG CRACKING	4-7
4.7.1 Sample Preparation	4-7
4.7.2 Microscopy and microchemistry characterization by TEM	4-9
5 RESULTS	5-1
5.1 FOUR-POINT BEND TEST RESULTS OF 347 SS IN KOH WATER CHEMISTRY	5-1
5.1.1 Sample loading history	5-1
5.1.1 <i>Characterization of cracks</i>	5-5
5.2 FOUR-POINT BEND TEST RESULTS OF 347 SS IN LIOH WATER CHEMISTRY	5-14
5.2.1 <i>Sample loading history</i>	5-14
5.2.2 <i>Crack characterization</i>	5-18
5.3 THE INCLINATION ANGLES OF THE CRACKED GBS	5-27
5.4 OXIDATION BEHAVIOR ON SURFACE AND AT GRAIN BOUNDARIES	5-27
5.5 MICROSTRUCTURE AND MICROCHEMISTRY OF NEUTRON IRRADIATED SAMPLES	5-31
5.5.1 Dislocation loops	5-31
5.5.2 Precipitates	5-31
5.5.3 Radiation induced segregation (RIS)	5-35
5.5.4 Voids	5-38
5.6 MICROSTRUCTURE AND MICROCHEMISTRY OF IG CRACKS IN NEUTRON IRRADIATED AND STRAINED SAMPLES	5-39
5.6.1 Sample D28-H-1 (26.4 dpa in LiOH)	5-39
5.6.2 Sample D28-H-3 (26.4 dpa in KOH)	5-41
5.6.3 Sample S-R2C6-T-1 (7.8 dpa in KOH)	5-45
5.6.4 Sample S-R2C6-T-4 (7.8 dpa in LiOH)	5-49
6 DISCUSSION	6-1
6.1 EFFECT OF DAMAGE LEVEL AND ENVIRONMENT ON IASCC INITIATION	6-1
6.2 EFFECT OF MICROSTRUCTURE ON IASCC INITIATION	6-2
6.2.1 IG cracking and GB oxidation	6-3

7	CONCLUSIONS	7-1
8	REFERENCES	8-1

LIST OF TABLES

Table 3-1: Chemistry of Baffle-former Bolt Materials (from References 7 and 10)	3-3
Table 3-2: Radioisotopic Content of Baffle-former Bolt Samples.....	3-3
Table 3-3: Sample ID designation for five sampling locations, dpa and calculated irradiated YS.	3-9
Table 3-4: Final Irradiated 4-point Specimen Identities, Dimensions, and Dose Rates.....	3-19
Table 3-5: TEM Specimens Prepared from Baffle-former Bolt Material	3-20
Table 4-1: The input parameters for the FEA simulation.....	4-4
Table 4-2: The summary of water parameters and strain rate for the four-point bend	4-5
Table 4-3: FIB liftouts from the three neutron irradiated materials.	4-7
Table 5-1: Crack statistics for the sample exposed to the KOH environment.	5-6
Table 5-2: Statistics of cracks in samples D28-H-2, D28-H-1, S-R6C6-H-3, S-R6C6-H-6, S-R6C6-T- 2and S-R2C6-T-4 after crack initiation in LiOH.	5-18
Table 5-3: The summary of the surface oxide film of the selected samples and conditions.....	5-30
Table 5-4: Summary of microstructures of neutron irradiated 347SS at different doses.	5-39
Table 5-5: Summary of cracked GBs studied in the neutron irradiated and strained Type 347 samples.	5-53

LIST OF FIGURES

Figure 2-1: Intact Baffle-former Bolt (Left) and Failed Type 347SS Baffle-former Bolts in a U.S. 4-loop Down-flow PWR	2-1
Figure 3-1: Left - Specimen Geometry (Dimensions in millimeters) Right – Specimens Inside 12.7mm Diameter Baffle-former Bolt Shank (conceptual sketch).....	3-1
Figure 3-2: Areas to be investigated by this experiment shown in green boxes, relative to data generated by testing Type 316 O-rings irradiated in PWRs (Figure adapted from Reference 15)...	3-2
Figure 3-3: Baffle-former bolt (left) showing cross-section of 4-point bend specimen milled into the threaded end, and (right) the 4-point bend specimens cut free from the bolt.	3-4
Figure 3-4: Machining of 4-point bend samples from unirradiated practice bolt	3-4
Figure 3-5: Practice 4-point bend samples (unpolished) from unirradiated practice bolt.....	3-5
Figure 3-6: Approximate locations for specimen machining for Salem 1 bolt D28. The 18 dpa sampling location is at the end of the threaded portion of the bolt, obscured by the nut used for ID purposes.	3-5
Figure 3-7: Approximate locations for specimen machining for DC Cook 2 S-R6C6	3-6
Figure 3-8: Approximate location for specimen machining for DC Cook 2 S-R2C6.....	3-6
Figure 3-9: Tormach CNC Machine Installed in Cell M	3-7
Figure 3-10: View within CNC machine, within M Cell, showing milling of 4-point bend cross section into threaded end of bolt	3-7
Figure 3-11: View within CNC machine, within M Cell, showing 4 point bend specimens being cut free from the bolt.....	3-8
Figure 3-12: Yield stress of 347SS as a function of dpa.	3-9
Figure 3-13: A surface SEM scanning showing the morphology of the metallic inclusions in the SS347 used in this study; (a) NbC inclusion, (b) MnS inclusion and (c), EDX elemental analysis of the NbC inclusion, and (d) MnS inclusion.	3-10
Figure 3-14: Effect of electropolishing showing difference between (left) as polished specimen and (right) specimen after 15 seconds of electropolishing	3-11
Figure 3-15: Effect of electropolishing showing difference between (right) as polished specimen and (left) specimen after 60 seconds of electropolishing, with the etching of stringers indicated by red arrows.....	3-11
Figure 3-16: Tube to contain 5 4-point bend specimens in membrane boxes.....	3-12
Figure 3-17: 5 Tubes (to each contain 5 4-point bend specimens in membrane boxes) Arranged in Foam for Insertion into Cask	3-12
Figure 3-18: Cask Packaging	3-13
Figure 3-19: Sample for TEM Lamella Extraction in Protective Case	3-14

Figure 3-20: Specimen (left) before and (right) after wide-area ion beam polishing	3-15
Figure 3-21: Selection of carbon deposition regions, attempting to center grain boundaries under the mask prior to ion milling for lamella preparation	3-15
Figure 3-22: Trenches cut around carbon deposits	3-16
Figure 3-23: Six undercut lamellas	3-16
Figure 3-24: Undercut lamella containing some apparent inclusions	3-17
Figure 3-25: Lamella attached to lift-out needle prior to placement on grid (light optical image).....	3-17
Figure 3-26: Lamella placed on grid (light optical image)	3-17
Figure 3-27: Lamella deposited on grid after final thinning (viewed via SEM).....	3-18
Figure 4-1: Schematic of the 4PB loading fixture, (a) a side view of a conceptual design the loading fixture, (b) The IM2 loading fixture and one of the tested samples, (c) SEM images of an example of side view, surface view without oxidation, and surface view with after 4PB testing, and (d) a side view of the loading fixture with dimensions.	4-1
Figure 4-2: SEM image of one of the tested samples that showing the area that scanned with the SEM to detect the IASCC. Each box in the grid represents a $5.04 \times 3.78 \mu\text{m}^2$ image and the grid contain 293 images.	4-3
Figure 4-3: Images of the autoclave test system and water loop. a) control panel front, b) control panel back with plumbing and sensors, and c) load frame, motor, and autoclave.....	4-5
Figure 4-4: Intensity profile (right) across an oxidized grain boundary (left).	4-6
Figure 4-5: Intensity profile (right) across cracked grain boundary (left). Red arrows indicate intensity profile peaks associated with exposed corners of the grain.	4-6
Figure 4-6: (a) and (b) show the two lamellas from the material D28H6 on the position 2 and 3 of the FIB grid; (c) and (d) show the two lamellas after having been further thinned.	4-7
Figure 4-7: (a) and (b) show the two lamellas from the material R2C6T3 on the position 2 and 5 of the FIB grid; (c) and (d) show the two lamellas after having been further thinned (The liftout on the position 3 was missing).....	4-8
Figure 4-8: (a), (b) and (c) show the three lamellas from the material R6C6H5 on the position 2, 3 and 5 of the FIB grid; (d), (e) and (f) show the three lamella after having been further thinned.	4-8
Figure 5-1: Load versus LVDT displacement for the samples tested in KOH water chemistry. The IASCC initiation in (a) D28-H-3_26.4 were observed after straining to 0.6YS, (b) S-R6C6-H-4_18.4 were observed after straining to 0.6YS (c) S-R6C6-T-5_11.5 were observed after straining to 0.6YS (d) S-R6C6-T-3_11.5 were observed after straining to 0.8YS (e) S-R2C6-T-1_7.8 were observed after straining to 0.6YS (f) S-R2C6-T-2_7.8 were observed after straining to 0.8YS (g) D28-T-2_16.5 were observed after straining to 0.7YS, and (h) S-R6C6-T-3_11.5 were observed after straining to 0.8YS.	5-3
Figure 5-2: Morphologies of 4PB samples after final bending tests in the KOH water chemistry.....	5-4

- Figure 5-3: A representative crack from sample D28-H-3_26.4 (a) BSE image at 0.6 YS, (b) BE image of the same region at 0.7YS, (c) and (d) magnified SE image of the crack initiation site. ...5-7
- Figure 5-4: A representative crack from sample S-R6C6-H-4_18.4 at 0.6 YS. (a) BSE image, (b) SE image of the same region, (c) magnified picture of the crack initiation sites (Red Box in (b)).5-8
- Figure 5-5: Representative cracks from sample S-R6C6-T-5_11.5 at 0.6 YS. (a) BSE image (b) SE image of the same region, (c) and (d) magnified SE image of the crack initiation sites.5-9
- Figure 5-6: Representative cracks from sample S-R6C6-T-3_11.5 at 0.6 YS. (a) BSE image (b) SE image of the same region, (c) and (d) magnified SE image of the crack initiation sites.5-10
- Figure 5-7: The largest crack from sample S-R2C6-T-1_7.8 dpa at 0.6 YS.5-11
- Figure 5-8: (a) the total equivalent stresses at the surface of a non-uniform 4PB samples (S-R6C6-T-1_7.8 simulated) with a change in thickness of 20 μm between short edges, (b) the equivalent stresses profile along the transverse edge, and (c) the transverse equivalent stresses as a function of distance for uniform (dashed blue and green lines) and the non-uniform thickness (solid red for the loading condition in (a) and (b) and solid black for another loading condition).5-12
- Figure 5-9: A representative crack from sample S-R2C6-T-2 at 0.8 YS. (a) BSE image, (b) SE image of the same region, and (c) a magnified SE image of the crack initiation site.5-13
- Figure 5-10: A representative crack from sample D28-T-2 at 0.7 YS. (a) BSE image, (b) magnified SE image of the same region, and (c) a magnified SE image of the crack initiation site, (d) a higher-magnification view of the yellow box in (c).5-14
- Figure 5-11: Load versus LVDT displacement for the samples tested in the LiOH water chemistry. The IASCC initiation in (a) D28-H-1_26.4 were observed after straining to 0.8YS, (b) D28-H-2_26.4 were observed after straining to 0.8YS (c) S-R6C6-H-3_18.4 were observed after straining to 0.6YS (d) S-R6C6-H-6_18.4 were observed after straining to 0.6YS (e) S-R6C6-T-2_11.5 were observed after straining to 0.8YS (f) S-R2C6-T-4_7.8 were observed after straining to 0.7YS (g) D28-T-1_16.5 were observed after straining to 0.6YS.5-16
- Figure 5-12: Morphologies of four-point bend samples after final bending tests in LiOH water chemistry.5-17
- Figure 5-13: A representative crack from sample D28-H-2 at 0.8 YS in LiOH. (a) BSE image, (b) magnified BSE image, (c) SE image of the same region, and (d) magnified SE image of the crack initiation site.5-19
- Figure 5-14: A representative crack from sample D28-H-1 at 0.8 YS in LiOH. (a) BSE image, (b) magnified BSE image, (c) SE image of the same region, and (d) magnified SE image of the crack initiation site.5-20
- Figure 5-15: A representative crack from sample S-R6C6-H-3 at 0.6 YS in LiOH. (a) BSE image, (b) magnified BSE image, (c) SE image of the same region, and (d) magnified SE image of the crack initiation site.5-21

- Figure 5-16: A representative crack from sample S-R6C6-H-6 at 0.6 YS in LiOH. (a) BSE image, (b) magnified BSE image, (c) SE image of the same region, and (d) magnified SE image of the crack initiation site. 5-22
- Figure 5-17: A representative crack from sample S-R6C6-T-2 at 0.8 YS in LiOH. (a) BSE image, (b) magnified BSE image, (c) SE image of the same region, and (d) magnified SE image of the crack initiation site. 5-23
- Figure 5-18: A representative crack from sample S-R2C6-T-4 at 0.7 YS in LiOH. (a) BSE image, (b) magnified BSE image, (c) SE image of the same region, and (d) magnified SE image of the crack initiation site. 5-24
- Figure 5-19: A representative crack from sample D28-T-1 at 0.8 YS in LiOH. (a) BSE image, (b) SE image of the same region, and (c) a magnified SE image of the crack initiation site. 5-25
- Figure 5-20: BSE (left) and SEM (right) images of specimen S-R2C6-T2 after oxide removal. 5-26
- Figure 5-21: The comparison of trace inclination angle of cracks for testes in PWR KOH and PWR LiOH water chemistries. 5-27
- Figure 5-22: The surface morphology and EDX analyses of the surface oxides of the sample S-R6C6-T-3 in KOH water chemistry. 5-28
- Figure 5-23: The surface morphology and EDX analyses of the surface oxides of the sample D-28-H-2 in LiOH water chemistry. 5-29
- Figure 5-24: TEM-HAADF analysis for the inner layer surface oxide film thickness measurement of (a) D28-H-1_26.5 in LiOH and (b) D28-H-3_26.5 in KOH. The dashed yellow lines indicating the locations of measurements. 5-30
- Figure 5-25: (a), (b) and (c) are rdDF images taken from the 8 dpa, 18 dpa and 26 dpa irradiated samples, respectively, using the $\frac{1}{2}\{311\}$ diffraction showing dislocation loops in the materials. The insets are SAED patterns showing the $\{311\}$ 2B condition for the rdDF imaging. 5-31
- Figure 5-26: Ni-maps (a-c) and Si-maps (d-f) collected from the 347-alloy materials irradiated by neutron at dose levels of a-d: 8 dpa, b-e: 18 dpa and c-f: 26 dpa, respectively. 5-32
- Figure 5-27: S-, P-, Nb-, and Mn-maps collected from the 347-alloy material irradiated to neutron at dose levels of a-d: 8 dpa, e-h: 18 dpa and i-l: 26 dpa, respectively. 5-33
- Figure 5-28: (a) rdDF image of a large precipitate in the 26 dpa irradiated sample, (b)-(k) are Nb-, Ni-, C-, N-, Cr-, Fe-, Si-, P-, S- and Mn-maps collected from the precipitate, respectively. 5-34
- Figure 5-29: (a)-(b) STEM-BF images of a large precipitate in the 26 dpa irradiated sample, (c)-(l) are Ni-, Si-, S-, P-, Nb-, Mn-, Fe-, Cr-, C- and N-maps collected from the precipitate, respectively. 5-34
- Figure 5-30: (a) STEM-BF image of a HAGB in the 8 dpa irradiated sample, (b)-(j) are Ni-, Si-, S-, P-, Nb-, N-, Mn-, Cr-, and Fe-maps, respectively. 5-35
- Figure 5-31: (a) STEM-BF image of a HAGB in the 8 dpa irradiated sample with an arrow drawn for element profiles; (b) displays Ni-, Si-, S-, P-, Nb-, N-, Mn-, Cr-, and Fe-profiles along the arrow drawn in (a); (c) displays magnified P-, S-, Mn- and P-profiles shown in (b). 5-35

- Figure 5-32: (a) STEM-BF image of a HAGB in the 18 dpa irradiated sample, (b)-(j) are Ni-, Si-, P-, Nb-, S-, N-, Cr-, Fe- and Mn -maps, respectively. 5-36
- Figure 5-33: (a) STEM-BF image of a HAGB in the 18 dpa irradiated sample with an arrow drawn for element profiles; (b) displays Ni-, Si-, S-, P-, Nb-, N-, Mn-, Cr-, and Fe-profiles along the arrow drawn in (a); (c) displays magnified P-, S-, Mn- and P-profiles shown in (b). 5-36
- Figure 5-34: (a) and (b) are STEM-HAADF and BF images of a TB in the 18 dpa irradiated sample, (b)-(j) are Ni-, Si-, S-, P-, Nb-, Mn-, Fe- and Cr -maps, respectively. 5-37
- Figure 5-35: (a) and (b) STEM-HAADF and BF images of a HAGB in the 26 dpa irradiated sample, (c)-(j) are Ni-, Si-, S-, P-, Nb-, Mn, Fe-, and Cr-maps, respectively. 5-37
- Figure 5-37: (a) –(c) BF images showing voids in 8 dpa, 18 dpa and 26 dpa irradiated samples, respectively. 5-38
- Figure 5-38: (a) is a STEM-HAADF image of a cracked GB in the 26.4 dpa irradiated and strained in LiOH sample, (b)-(f) are corresponding Fe-, Cr-, Ni-, O-, and C-maps, respectively. ... 5-39
- Figure 5-39: (a) and (b) are STEM-HAADF and BF images of the cracked GB shown in Figure 5-38 in the 26.4 dpa irradiated and strained in LiOH sample, (c)-(f) are corresponding Fe-, Ni-, O-, and Cr-maps, respectively. 5-40
- Figure 5-40: (a) and (b) are STEM-HAADF and BF images of the crack-tip region of the cracked GB shown in Figure 5-38 in the 26.4 dpa irradiated and strained in LiOH sample, (c)-(f) are corresponding Fe-, Cr-, Ni-Si-, P-, Nb-, S- and O-maps, respectively. 5-41
- Figure 5-41: (a) is a STEM-HAADF image of cracked GB in the 26.4 dpa irradiated and strained in KOH sample, (b)-(f) are corresponding Cr-, Fe-, Ni-, O- and Nb-maps, respectively. 5-41
- Figure 5-42: (a) and (b) are STEM-HAADF and BF images of the cracked GB shown in Fig. 19 in the 26.4 dpa irradiated and strained in KOH sample, (c)-(f) are corresponding Fe-, Ni-, O-, and Cr-maps, respectively. 5-42
- Figure 5-43: (a) is a STEM-HAADF image of the crack-tip region of the cracked GB shown in Fig. 19 in the 26.4 dpa irradiated and strained in KOH sample, (b)-(f) are corresponding Fe-, Cr-, Ni-, S- and O-maps, respectively. 5-43
- Figure 5-44: (a) is a series of STEM-BF images taken along a cracked GB in the 26.4 dpa irradiated and strained in KOH sample, (b)-(d) are corresponding series of O-, Ni- and Nb-maps, respectively. 5-44
- Figure 5-45: (a) and (b) are STEM-HAADF and BF images taken from a long-cracked GB in the 26.4 dpa irradiated and strained in KOH sample, (c)-(g) are corresponding series of Fe-, Cr-, Ni-, O-, and Nb-maps, respectively. 5-45
- Figure 5-46: (a) and (b) are STEM-HAADF and BF images of a cracked GB in the 7.8 dpa irradiated and strained in KOH sample, (c)-(f) are corresponding Fe-, Ni-, O-, and Cr-maps, respectively. 5-46
- Figure 5-47: (a) are overlaid O-, Fe, Cr- and Ni-element maps of a cracked in the 7.8 dpa irradiated and strained in KOH sample with an arrow drawn for extracting element profiles along the

- arrow; (b) displays corresponding Fe-, Ni-, O-, and Cr-element profiles, respectively. 5-47
- Figure 5-48: (a) and (b) are STEM-HAADF and BF images taken from a long-cracked GB in the 7.8 dpa irradiated and strained in KOH sample, (c)-(g) are corresponding series of Fe-, Cr-, Ni-, O-, and Nb-maps, respectively. 5-48
- Figure 5-49: (a) and (b) are STEM-HAADF and BF images taken from a long-cracked GB in the 7.8 dpa irradiated and strained in KOH sample, (c)-(g) are corresponding series of Fe-, Cr-, Ni-, O-, and Nb-maps, respectively. 5-49
- Figure 5-50: (a) is a STEM-HAADF of a cracked GB in the 7.8 dpa irradiated and strained in LiOH sample, (c)-(f) are corresponding Fe-, Ni-, O-, and Cr-maps, respectively. 5-50
- Figure 5-51: (a) is a STEM-HAADF of a cracked GB in the 7.8 dpa irradiated and strained in LiOH sample, (c)-(f) are corresponding Fe-, Ni-, O-, and Cr-maps, respectively. 5-50
- Figure 5-52: (a) a STEM-HAADF image showing a long-cracked GB; and (b)~(e) are STEM-LAADF, BF, and HAADF images and O-map, respectively, taken from a long-cracked GB in the 7.8 dpa irradiated and strained in LiOH sample. 5-51
- Figure 6-1: Stress as a percent of the irradiated yield strength versus displacement damage for crack initiation in austenitic stainless steels in PWR primary water environments. Data for 347SS in this study are offset along the abscissa to avoid overlap. The solid line is a power-law fit of this study data points and the dashed line is the literature data points. 6-3
- Figure 6-2: (a) Crack numbers and densities in both water chemistries, average length (b) as function of the damage level, (c) as a function of the fraction of the irradiated YS, and (d) the crack depth as a function of damage level. 6-5

Acronyms & Abbreviations

4PB	4-point bend
BF	Bright field
BSE	Back scattered electron
CMTR	Certified material test report
DB	Deformation band
DC	Dislocation channel
DCC2	D.C. Cook Unit 2
DF	Dark field
dpa	Displacements per atom
EDS	Energy dispersive X-ray spectroscopy
EELS	electron energy loss spectroscopy
FIB	Focused ion beam
GB	Grain boundary
IASCC	Irradiation-assisted stress corrosion cracking
IG	Intergranular
LVDT	Linear voltage displacement transducer
RIS	Radiation-induced segregation
S1	Salem Unit 1
SS	Stainless Steel
STEM	Scanning Transmission Electron Microscope
TEM	Transmission Electron Microscope
YS	Yield stress

1 EXECUTIVE SUMMARY

This document serves as the final report for NSUF Project 19-16567 (Reference 1) and its supporting contracts (References 2 and 3). It documents completion of testing of specimens fabricated as previously described in Reference 4.

At a high level, the purpose of the testing is to generate data to support continued operation of light water reactors (LWR) and provide further understanding of irradiation-assisted stress corrosion crack (IASCC) initiation in baffle-former bolt materials. Baffle-former bolts that had been extracted from commercial pressurized water reactors (PWRs) were machined into miniature 4-point bend specimens and TEM samples at the Westinghouse Churchill Site hot cell facility. These samples were then shipped to the University of Michigan to undergo IASCC initiation testing in simulated PWR primary coolant containing either LiOH or KOH additions.

Overall, 15 samples were tested, 8 in water with KOH additions and 7 in water with LiOH additions, until indications of cracking were observed. Crack initiation stress was similar in both water environments at 50-60% of the irradiated yield stress. Post-test examination of the cracking sites, including scanning electron microscopy and transmission electron microscopy, demonstrated that the crack initiation mechanism and crack initiation rates were similar between the two different water chemistries. A grain boundary oxidation and oxide fracture mechanism was observed to be responsible for crack initiation.

This document was created and verified in accordance with the Westinghouse test plan (Reference 5) and the Westinghouse Global Management System.

2 BACKGROUND AND MOTIVATION

This project is intended to support continued operation of light water reactors by furthering understanding of IASCC. In 2016, substantial degradation of Type 347SS baffle-former bolts was observed in pressurized water reactors (PWRs) (Reference 6). The failures were attributed to IASCC (Reference 7), with some examples shown in Figure 2-1. The baffle-former bolts are located inside the reactor near the core. Their inspection and replacement require the reactor to be shut down, vessel head to be opened up, and the fuel removed. The work must be conducted in a radiologically controlled area, and results in some amount of radiation dose to personnel. Because the extent of degradation observed in 2016 was not anticipated, the affected power plants underwent extended refueling and maintenance outages at considerable cost. Extended maintenance outages are often quoted to cost greater than one million dollars per day in equipment, personnel, and lost generation costs. Better prediction of IASCC allows for proactive rather than reactive maintenance activities, which can be performed with less impact on the duration of maintenance outages, thus improving economics and reliability of PWR operations. IASCC inspections are conducted as required at every operating light water reactor; while a majority of light water reactors throughout the world have reported IASCC-related degradation to some extent, all light water reactors are affected by the inspection requirements.

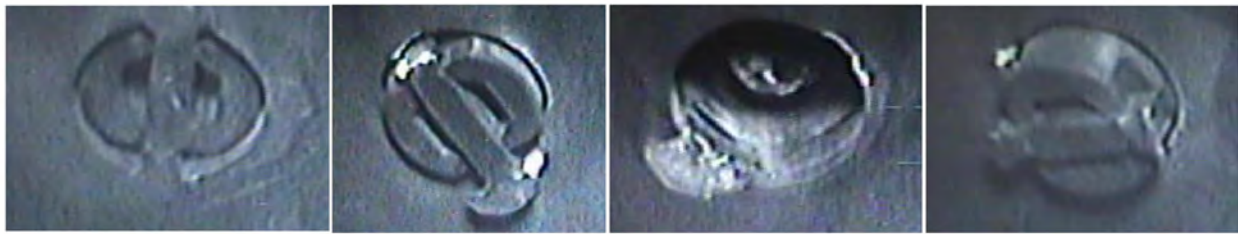


Figure 2-1: Intact Baffle-former Bolt (Left) and Failed Type 347SS Baffle-former Bolts in a U.S. 4-loop Down-flow PWR

Some U.S. nuclear power plants are also considering a change in primary coolant water chemistry as a potential cost savings measure. Currently, the primary coolant water contains additions of boron (added as boric acid) to assist in controlling the nuclear reaction, and a lithium hydroxide addition to maintain the pH balance, under operating conditions of 500-600°F and 2,500 psi pressure. The change would be to use potassium hydroxide in place of lithium hydroxide, as lithium prices have increased and concerns over the supply chain security of lithium have been raised (Reference 8). Lithium must also be processed to remove lithium 6, which has a large neutron absorption cross-section and so is undesirable for use in PWRs. In addition to providing an economical alternative to lithium, the use of potassium may also result in less aggressive water chemistry as potassium remains in the exterior oxide layer on the metal surface while lithium has been observed to penetrate into the inner oxide layer and along grain boundaries (Reference 9). Therefore, investigating IASCC and the use of KOH in PWR coolant is an opportunity to improve the economics of PWR operations by reducing material and maintenance costs.

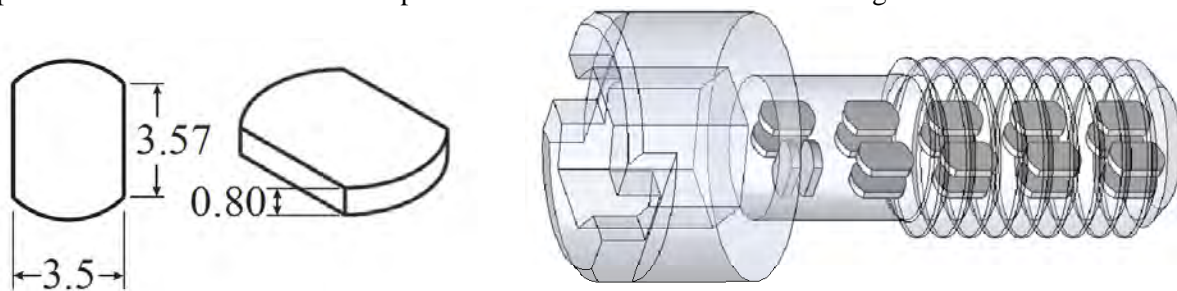
This project utilized a recently developed miniature 4-point bend test specimen design in combination with the Type 347SS baffle-former bolt material from the affected PWRs. This unique specimen design allowed multiple samples to be extracted from a single baffle-former bolt, allowing an unprecedented amount of IASCC initiation data to be collected from this material. The use of Type 347SS material is crucial because most IASCC initiation data has been collected from tests on cold-worked Type 316 flux thimble tube material, which has not been observed to fail by IASCC in service. This project couples the

advantages of the miniature 4-point bend specimen with the critical PWR-irradiated Type 347SS material to provide novel data on IASCC behavior with direct benefits to the operating PWR fleet.

3 SPECIMEN MATERIAL AND FABRICATION

The Westinghouse workscope within this project is to generate sub-sized IASCC initiation test specimens and corresponding transmission electron microscopy (TEM) samples from PWR-irradiated Type 347SS baffle-former bolts.

The IASCC initiation test specimens are small disks (Figure 3-1) which enable multiple specimens to be cut from the shank of a baffle-former bolt at the same location along its length. This will result in sets of specimens with effectively equivalent radiation dose and service conditions. This specimen geometry has previously been successfully implemented in IASCC testing of Type 316 stainless steel (Reference 19) providing new information on the specific sites at which cracks initiated and the relation between deformation and cracking. Specimens from each set will be tested in lithium hydroxide and in potassium hydroxide environments, allowing for a direct comparison of the effects of these environments at each dpa level. A second test in KOH is planned at each dose level as such testing in KOH is first-of-a-kind.



**Figure 3-1: Left - Specimen Geometry (Dimensions in millimeters)
Right – Specimens Inside 12.7mm Diameter Baffle-former Bolt Shank (conceptual sketch)**

The radiation dose varies in a predictable fashion along the axis of each baffle former bolt. Specimens of a range of fluences were created for testing, allowing the effects of radiation dose on IASCC initiation to be examined. The range of radiation damage and stress investigated by the tests is shown in Figure 3-2. By allowing many specimens to be cut from the same piece of bolt, heat-to-heat effects on the cracking behavior are eliminated. Because the radiation dose to such material increases as power plants age, this understanding will allow for improved prediction of IASCC-related degradation.

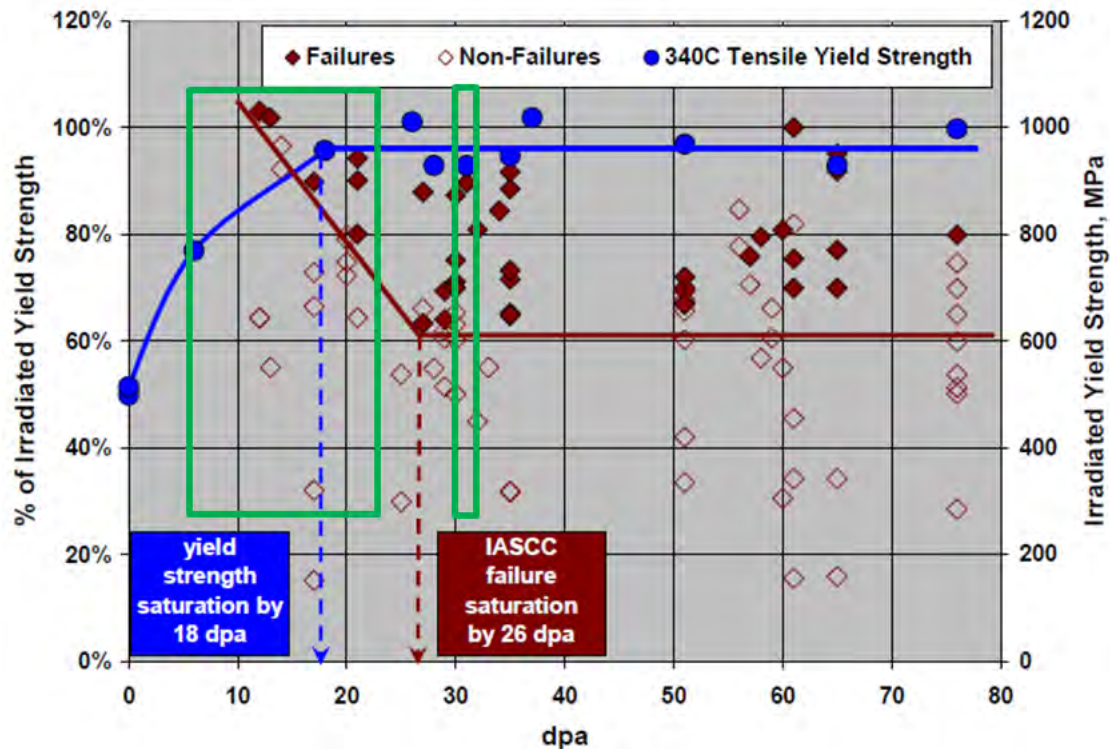


Figure 3-2: Areas to be investigated by this experiment shown in green boxes, relative to data generated by testing Type 316 O-rings irradiated in PWRs (Figure adapted from Reference 15)

The material used for testing will be material from baffle-former bolts extracted from commercial PWRs. The bolt material was procured to ASTM A193 (Reference 11). While certified material test reports (CMTRs) are available for baffle-former bolts installed at the PWRs they were extracted from, as a bulk item precise traceability for a bolt at a specific, installed location to a specific heat or CMTR was not maintained. Ultimately the bolts used for the experiment were Salem 1 (S1) bolt D28, DC Cook 2 (DCC2) S-R6C6, and DC Cook 2 S-R2C6.

These baffle-former bolts were previously characterized as part of industry failure analysis (Reference 10) and are in storage at the Westinghouse Churchill Hot Cell Facility in the High Level Cell. The materials were owned by Westinghouse and existed as fractured (due to IASCC) bolts or whole bolts. Radiation levels of the bolt pieces are in the range of 200-1200 rem per hour on contact.

The baffle-former bolts installed at S1 were fabricated from Type 347 stainless steel in 1967. Certified Material Test Report (CMTR) chemical composition data are shown in Table 3-1. The material was procured as 16 mm bar, which underwent a hot-heading (or hot forging) process to form the 24 mm diameter bolt head, grinding operations to create the 13 mm bolt shank, and a cold rolling process to create the threads. Bolt D28 from S1 was in service from 1977 to 2019. The chemical composition of similar baffle former bolts from S1 was measured using optical emissions spectroscopy in Reference 7 and this data is shown for bolts B83, D2, and D92 in Table 3-1.

The original baffle-former bolt material at DCC2 is also Type 347 stainless steel of similar composition and vintage to the bolts from S1 (including same fabricator and steel supplier), however these bolts were fabricated by machining rather than by hot heading. The original DCC2 bolts were in service from 1978

to 2010. Chemical composition of similar bolts from DCC2 were measured by mass spectroscopy in Reference 10 for bolts N-R4C4, E-R4C6, W-R3C5, and S-R5C7 in Table 3-1.

Isotopic content of the baffle-former bolts in millicuries per gram is shown in Table 3-2.

Table 3-1: Chemistry of Baffle-former Bolt Materials (from References 7 and 10)

Heat / Bolt	Fe	Ni	Cr	Mn	Mo	Nb	Ta	Co	Si	C	P	S	N	Ti
ASTM A193 (11)	-	9.00-13.00	17.00-19.00	2.00 max	-	Cb + Ta \geq 10 x C content		-	1.00 max	-	0.045 max	0.030 max	-	-
CMTR X11014	Bal	10.46	18.10	1.63	0.33	0.96	0.0X ⁽²⁾							
CMTR 10879	Bal	10.68	17.95	1.34	0.33	0.70	0.06							
CMTR 39653	Bal	9.80	18.46	1.83	0.19	0.81	0.0X ⁽²⁾							
B83	68.14	10.40	17.76	1.28	0.30	0.74	0.00	0.07	0.91					
D2	67.21	10.35	17.81	1.48	0.26	0.94	0.00	0.06	1.25					
D92	68.35	10.21	17.76	1.26	0.26	0.68	0.00	0.06	0.94					
N-R4C4	69.4	10	17.5	1.7	0.1	1.1	0.1	<0.08	0.47	0.05	0.037	0.023	0.04	0.1
E-R4C6	66.9	10.9	19.2	1.7	0.1	0.8	-	<0.08	0.47	0.05	0.034	0.020	0.04	0.2
W-R3C5	66.4	11.2	19.7	1.7	0.1	0.8	-	<0.08	0.47	0.05	0.034	0.021	0.04	-
S-R5C7	66.8	10.9	19.6	1.7	0.1	0.8	-	<0.08	0.47	0.05	0.034	0.020	0.04	-

Notes:

- (1) All values given in weight percent.
- (2) Last digit for amount of tantalum is not visible on CMTR.

Table 3-2: Radioisotopic Content of Baffle-former Bolt Samples

Radioisotopic content in millicuries per gram:			
1.02E-02	C-14	1.42E-02	Nb-94
1.01E-03	Co-58	1.45E-08	Nb-95
4.20E+01	Co-60	5.52E-02	Ni-59
5.11E-09	Cr-51	7.20E+00	Ni-63
3.44E+01	Fe-55	5.62E-02	Ta-182
8.51E-07	Fe-59	3.79E-05	Tc-99
2.67E-02	H-3	8.68E-09	Zr-95
5.51E-01	Mn-54		

Similar baffle-former bolts have been previously characterized as part of failure analysis (References 10, 12) and as part of industry research efforts (Reference 13, 14). Such characterizations have included fractography (in the case of failed bolts), metallography, mechanical testing, and TEM.

Machining in the hot cell was necessitated due to the high radiation fields of the bolts. The M Cell was chosen for this purpose. A Tormach PCNC 440 machine was used to machine the specimens. This was accomplished by milling the cross section of the four-point bend specimen into the baffle-former bolt and then using a fine saw blade to cut individual specimens free. Computer-aided drawing (CAD) sketches of the result of such a process on a bolt are shown in Figure 3-3. This process was slightly different from the proposed cutting diagram in Figure 3-1, and considered an improvement because it allows six specimens to be cut from a single location along the bolt. In the project proposal, 24 tests were proposed. It was decided to cut 6 specimens from each of 5 locations to allow for a spare at each location should a sample become damaged during preparation; such a spare could also be used as a starting point for transmission electron microscopy (TEM) specimen preparation.

Practice machining was conducted on unirradiated material using the same model computer-numeric control (CNC) machine and same CNC program that was to be used for the irradiated material (Figure 3-4). This process was found to consistently produce acceptably-sized specimens (Figure 3-5).

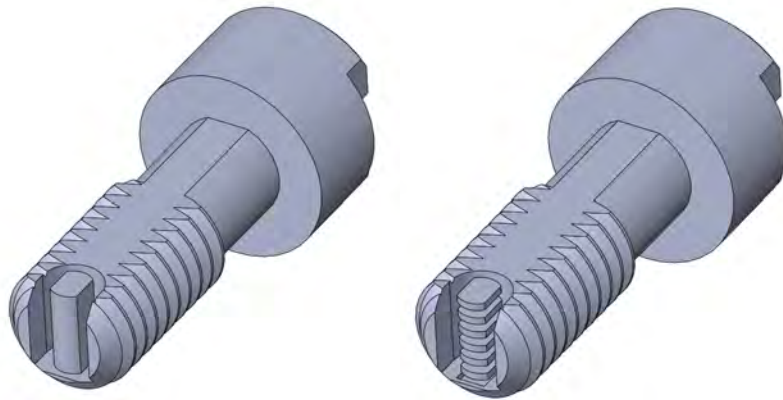


Figure 3-3: Baffle-former bolt (left) showing cross-section of 4-point bend specimen milled into the threaded end, and (right) the 4-point bend specimens cut free from the bolt.

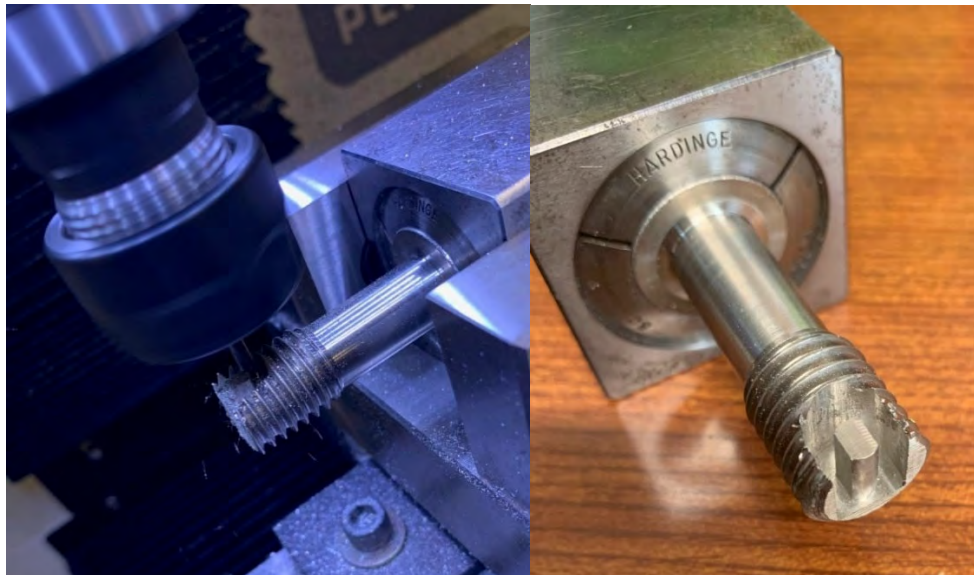


Figure 3-4: Machining of 4-point bend samples from unirradiated practice bolt

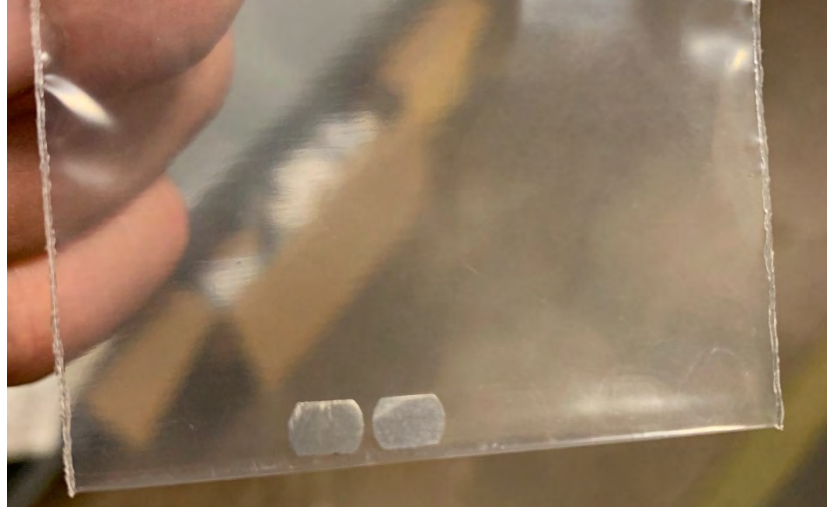


Figure 3-5: Practice 4-point bend samples (unpolished) from unirradiated practice bolt

To provide the range of radiation damage levels appropriate to the experiment, samples were cut from Salem Unit 1 bolt D28, D.C. Cook Unit 2 S-R2C6, and D.C. Cook Unit 2 S-R6C6 from the approximate locations shown in Figure 3-6, Figure 3-7, and Figure 3-8. This was achieved by installing the Tormach CNC machine into the M Cell (Figure 3-9). Machining was monitored by video camera installed inside the CNC machine; key steps of the machining process can be seen in Figure 3-10 and Figure 3-11.

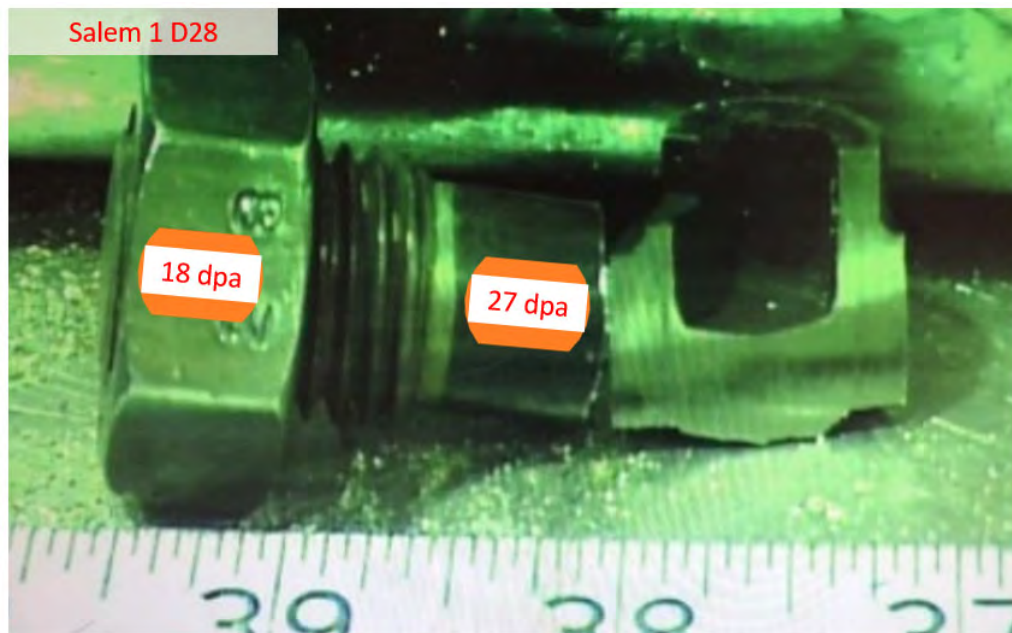


Figure 3-6: Approximate locations for specimen machining for Salem 1 bolt D28. The 18 dpa sampling location is at the end of the threaded portion of the bolt, obscured by the nut used for ID purposes.

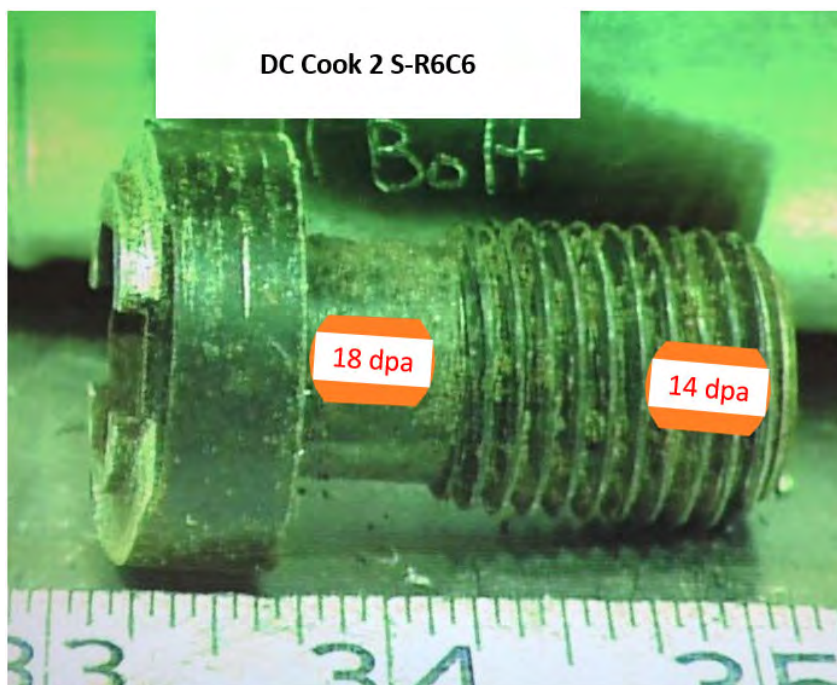


Figure 3-7: Approximate locations for specimen machining for DC Cook 2 S-R6C6

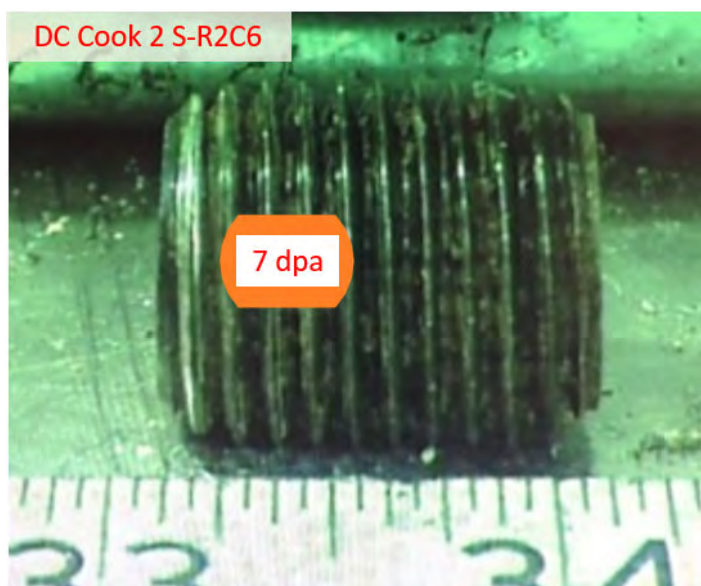


Figure 3-8: Approximate location for specimen machining for DC Cook 2 S-R2C6

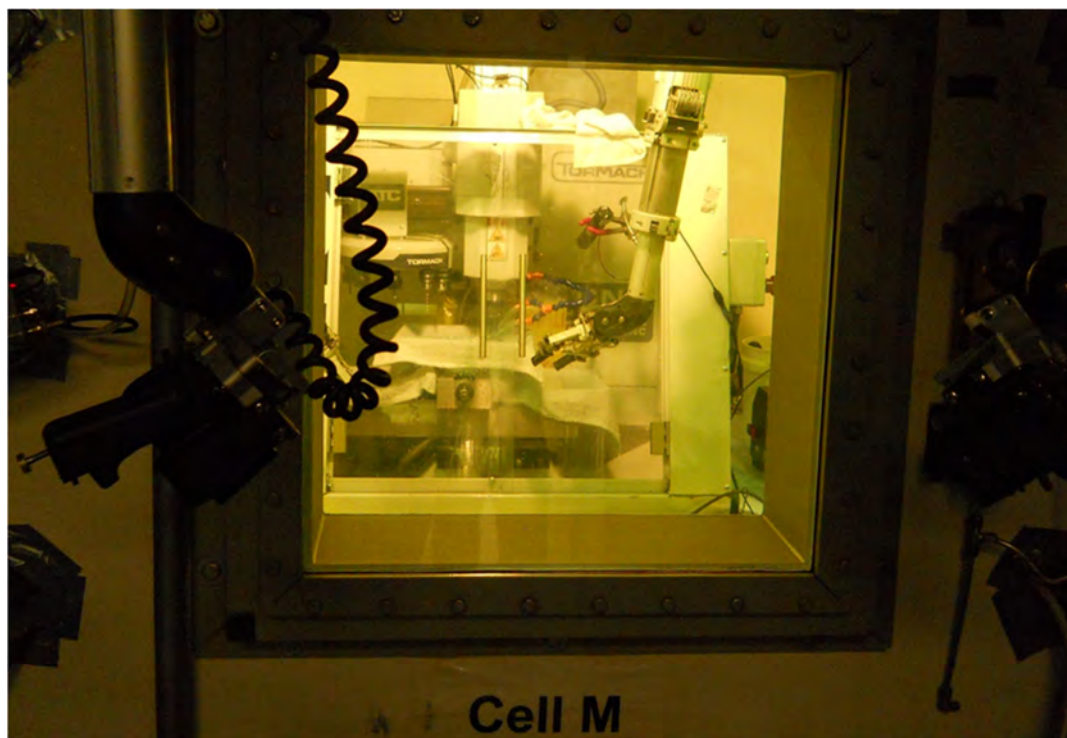


Figure 3-9: Tormach CNC Machine Installed in Cell M

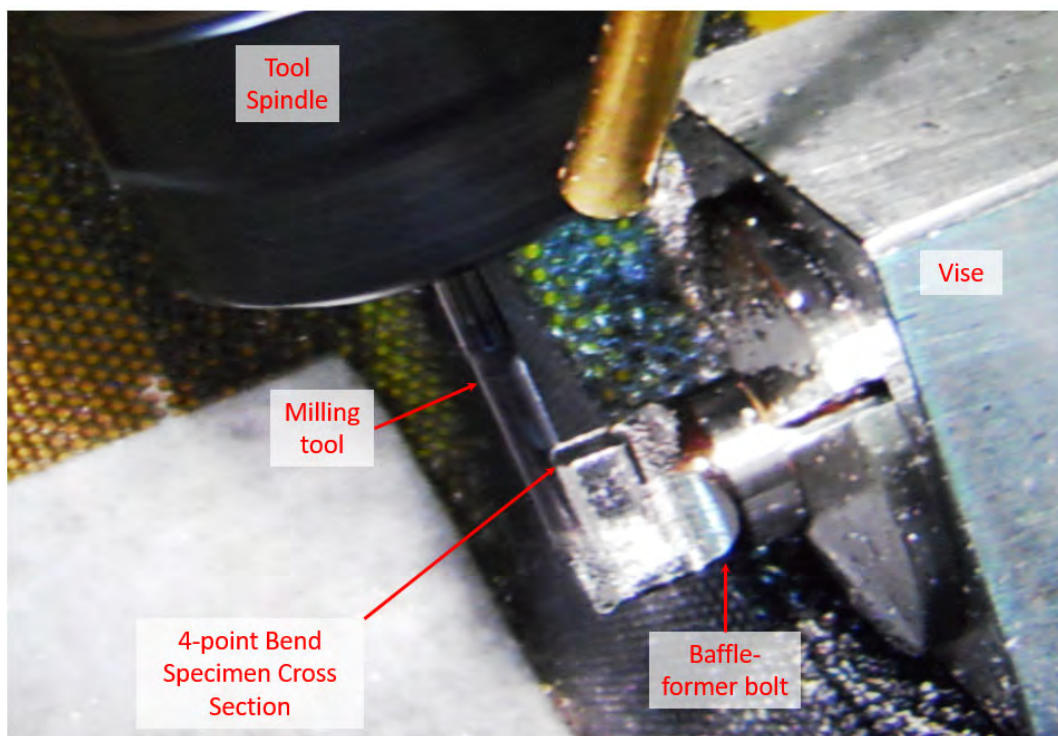


Figure 3-10: View within CNC machine, within M Cell, showing milling of 4-point bend cross section into threaded end of bolt

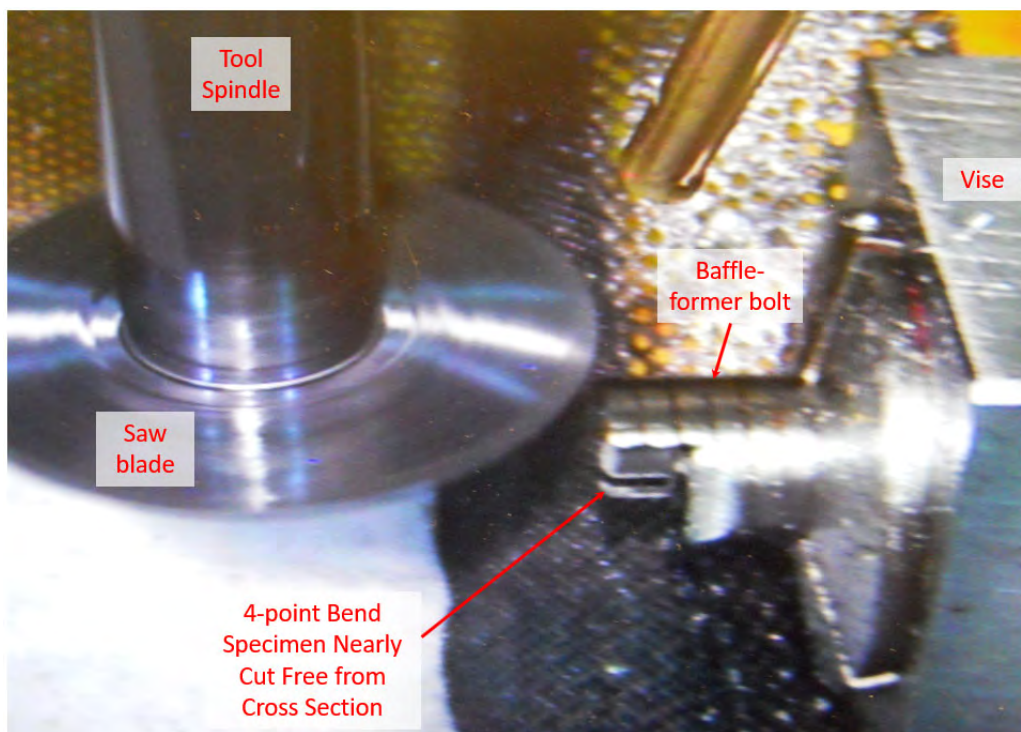


Figure 3-11: View within CNC machine, within M Cell, showing 4 point bend specimens being cut free from the bolt

After the 4-point bend specimens were cut free, the specimens were deburred. The specimens were then temporarily mounted in Konductomet® specimen holders, and then fastened in place using a small amount of Crystalbond. This allowed polishing of the specimens using typical metallographic polishing equipment. The specimens were polished to a final stage using oxide polishing suspension (OPS, colloidal silica). The resulting samples were identified using the bolt name, -T or -H for specimens machined at the threads or head of the bolt, respectively, followed by a sequential number indicating the sequence the specimens were cut from the bolt. As six specimens were cut through the diameter of a given bolt, specimens -1 and -6 would be near the OD of the bolt while specimens -3 and -4 would be nearer the center of the bolt diameter. The last part of the sample ID is the dose, in dpa, preceded by an underscore. The naming convention is then:

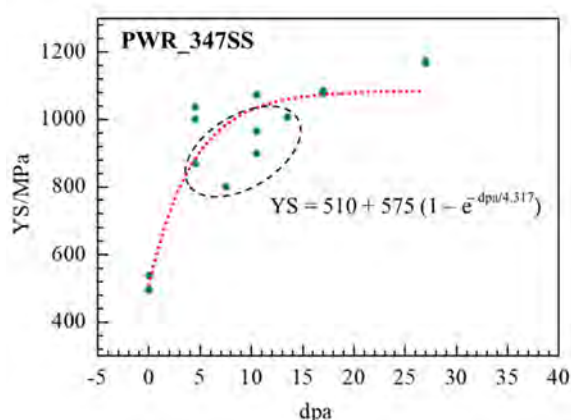
[Bolt ID]-[T]hread or [H]ead-[Sequential number, 1 through 6]_[irradiation damage in dpa].

Sample IDs, doses, and yield strength (YS) are listed in Table 3-3: . The dpa of each sample was calculated according the fluence gradient along the bolt (Reference 16). Since no data on the irradiated yield strength are available for these exact samples, literature data (References 7, 13) on the irradiation hardening of 347 SS were reviewed and plotted to create a empirical equation of yield stress as a function of dose as shown in Figure 3-12. The irradiated YS of each sample was estimated using this equation and listed in Table 3-3: for the dpa values provided.

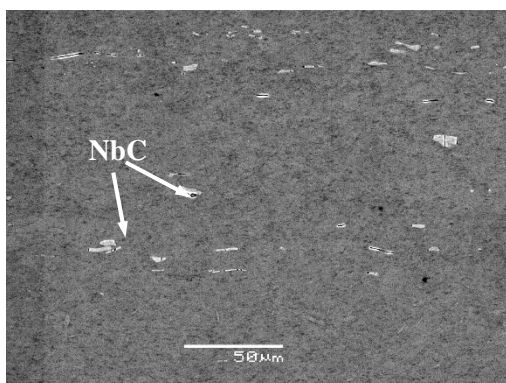
Table 3-3: Sample ID designation for five sampling locations, dpa and calculated irradiated YS.

Sample ID*	dpa	Irradiated YS/MPa	Source Reactor
S-R2C6-T_7.8	7.8	996	D.C. Cook Unit 2
S-R6C6-T_11.5	11.5	1050	D.C. Cook Unit 2
S-R6C6-H_18.4	18.4	1082	D.C. Cook Unit 2
D28-T_16.5	16.5	1077	Salem Unit 1
D28-H_26.4	26.4	1089	Salem Unit 1

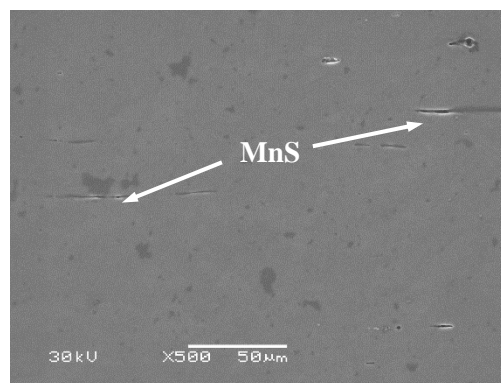
* Sample ID ended with the dpa level the sample has (i.e. _7.8 means 7.8 dpa) for simplicity while comparing results.

**Figure 3-12: Yield stress of 347SS as a function of dpa.**

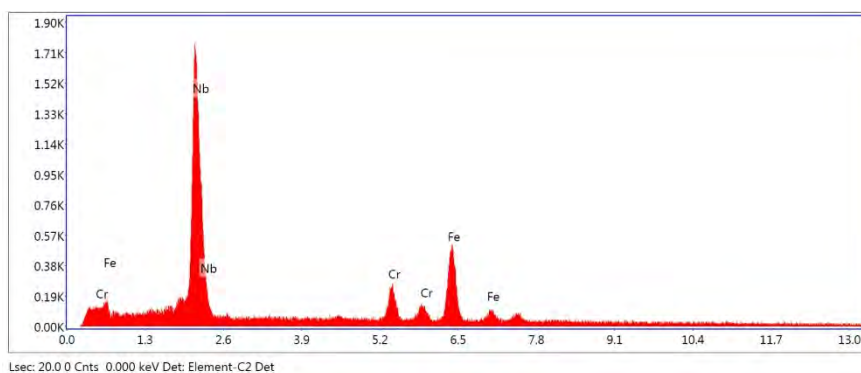
The grain size for this alloy was measured to be size number 9 (14.1 μm) according to ASTM E112-13 (Reference 17). The electrochemically polished surface was examined by SEM and the typical morphology is shown in Figure 3-13. Many metallic inclusions in blocky and elongated laths shape were observed in the 347 SS. The blocky shape inclusions are niobium carbides (NbC) as revealed by the EDX analysis while the stringer-like inclusions are manganese sulfides (MnS), which preferentially dissolved during electropolishing while the NbC were immune.



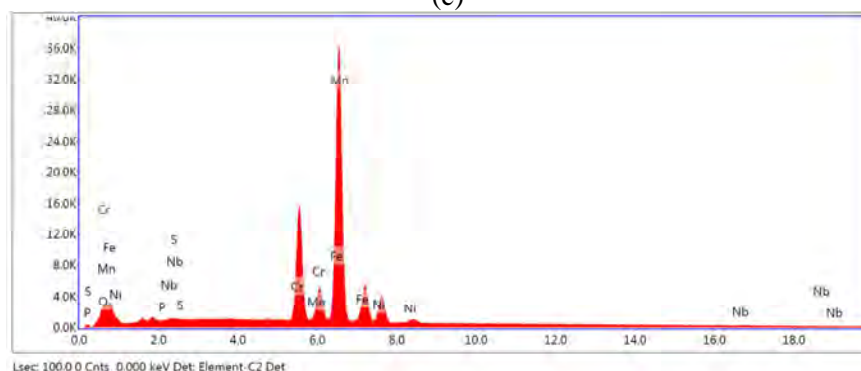
(a)



(b)



(c)



(d)

Figure 3-13: A surface SEM scanning showing the morphology of the metallic inclusions in the SS347 used in this study; (a) NbC inclusion, (b) MnS inclusion and (c), EDX elemental analysis of the NbC inclusion, and (d) MnS inclusion.

After mechanical polishing, the specimens were electropolished to remove any residual cold work or other remnants of the mechanical process to provide a high-quality surface to allow for examination of crack initiation sites. The specification ASTM B912 (Reference 18) gives a typical electropolishing solution recipe as a 1:1 mix of 96% sulfuric acid and 85% orthophosphoric acid, which was used for this project. The applied current was 2 amps. As the OPS polish leaves a very minimal amount of residual cold work, 15 seconds of electropolishing was determined to be sufficient to remove it. This practice was in line with recommendations from the University of Michigan. On practice specimens, the effect of the 15 second electropolish treatment was observed to both clean the specimens and remove a small amount of material. Material removal was selective towards vertices, and so removal of material was apparent when the grain boundaries in the polished surface were not visible afterwards (Figure 3-14). Longer electropolishing times (45-60 seconds) appeared to show selective attack of stringer-like inclusions of the material (Figure 3-15), which is undesirable.

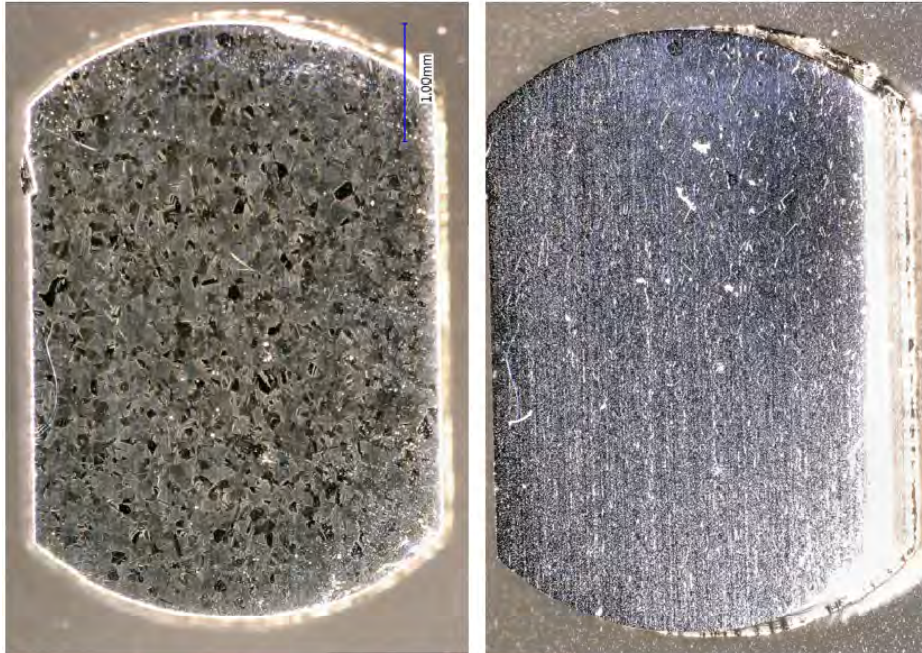


Figure 3-14: Effect of electropolishing showing difference between (left) as polished specimen and (right) specimen after 15 seconds of electropolishing

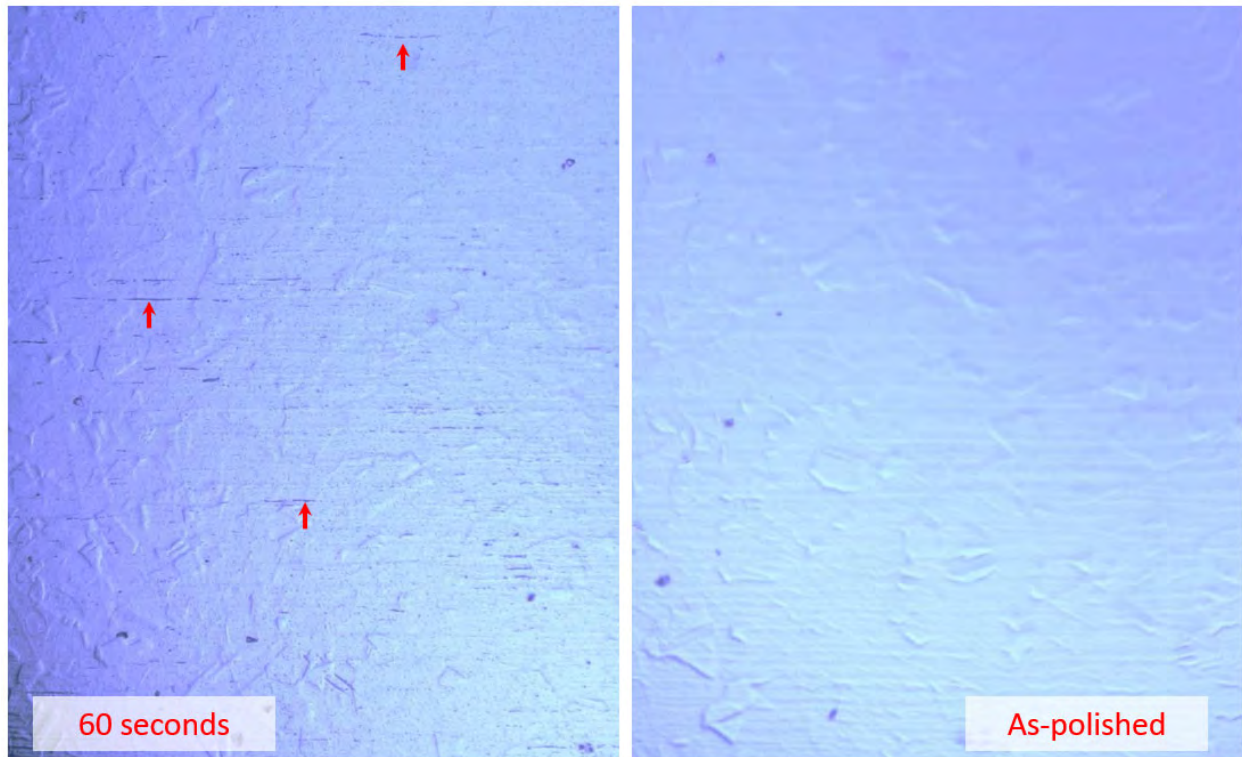


Figure 3-15: Effect of electropolishing showing difference between (right) as polished specimen and (left) specimen after 60 seconds of electropolishing, with the etching of stringers indicated by red arrows

The specimens remained in the Konductomet specimen holder during the electropolishing process. This allowed for easier handling during the electropolishing process. The specimens were then removed from the temporary mounts, cleaned in acetone, and subsequently placed in membrane boxes that were left open to facilitate photographing and minimize handling. The boxes were then closed and sealed to prevent exposure or contamination. First, the 5 specimens of each material condition were put into a tube (Figure 3-16). The five tubes of five specimens each were then placed into a piece of foam (Figure 3-17) used to center the materials when placed into the cask (Figure 3-18).



Figure 3-16: Tube to contain 5 4-point bend specimens in membrane boxes



Figure 3-17: 5 Tubes (to each contain 5 4-point bend specimens in membrane boxes) Arranged in Foam for Insertion into Cask

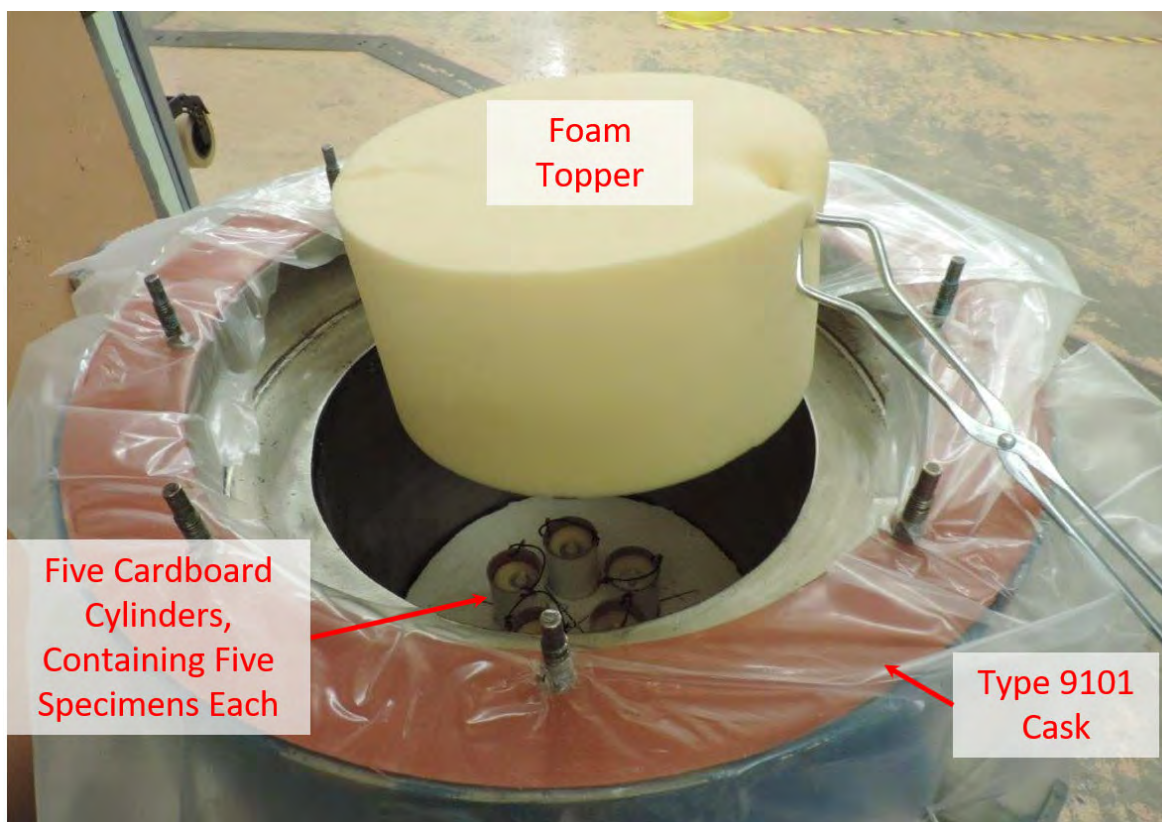


Figure 3-18: Cask Packaging

Of the 6 pieces that were removed from each baffle-former bolt location, 5 specimens were designated for 4-point bend testing while the 6th was used for preparing TEM specimens. This 6th 4-point bend specimen (of each material condition) was cut further into small pieces (roughly quarters), and one small piece was then mounted in Konductomet inside of a stainless steel tube (to allow for easier handling and breaking out of the larger metallographic mount), polished to OPS, and electropolished (Figure 3-19). TEM samples were prepared by focused ion beam (FIB) preparation of TEM lamella using the Tescan LYRA-3 GMU FIB/SEM (dual beam FIB with an Orsay Physics Canion FIB column) in the Westinghouse Churchill Site Electron Optics laboratory. The ExpressLO LLC *ex situ* liftout system was used for placing the cut lamella onto ExpressLO proprietary TEM grids.

First, to better identify grain boundaries, each sample was further polished using the ion beam at a current of 1 nA over a wide area (a view field of approximately 460 μm). Due to differential milling rate of grains at different orientations, the grain structure became apparent (Figure 3-20). Areas of interest were selected, aligning a grain boundary with the center of where the specimen was to be extracted (Figure 3-21), and a carbon mask ($\sim 20\mu\text{m} \times 2\mu\text{m}$, 1 μm thick) was deposited over these areas to protect them from the ion beam. Trenches were then cut on both sides of the carbon deposits (Figure 3-22), surfaces polished (typically at or below 1 nA), and undercut (Figure 3-23). As is seen from the undercut lamella (Figure 3-24), it was usually possible to identify multiple grain boundaries and sometimes inclusions. The lamella surfaces were then further polished to remove redeposition after undercutting, and the final tabs milled away, which allowed the lamella to rest unattached at the bottom of its trench. The sample was then removed from the FIB/SEM and placed on the stage of the *ex situ* system. Once placed, the lamella was extracted from the trenches (Figure 3-25) and placed on a copper grid with numbered slots (Figure 3-26). Once all lamellas were transferred to a grid, it was placed back in the SEM and carbon was deposited on

the edges to further secure the specimen (Figure 3-27). Final thinning to electron transparency was then completed. Each lamella was thinned at 30 kV and ~100-120 pA, followed by a final polish at 5 kV at 40-50 pA.

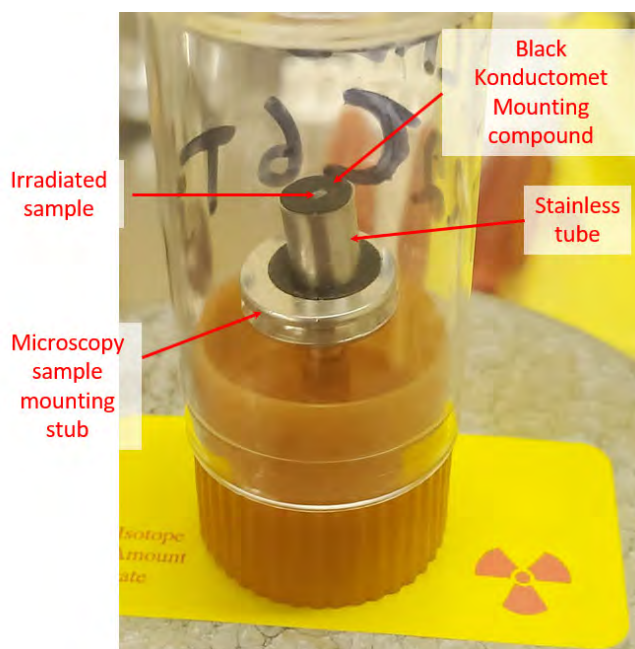


Figure 3-19: Sample for TEM Lamella Extraction in Protective Case

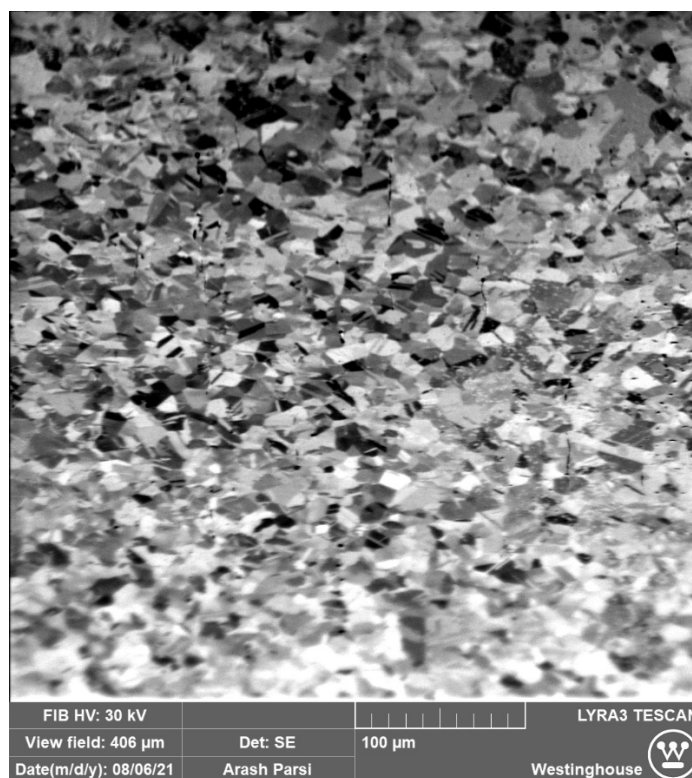
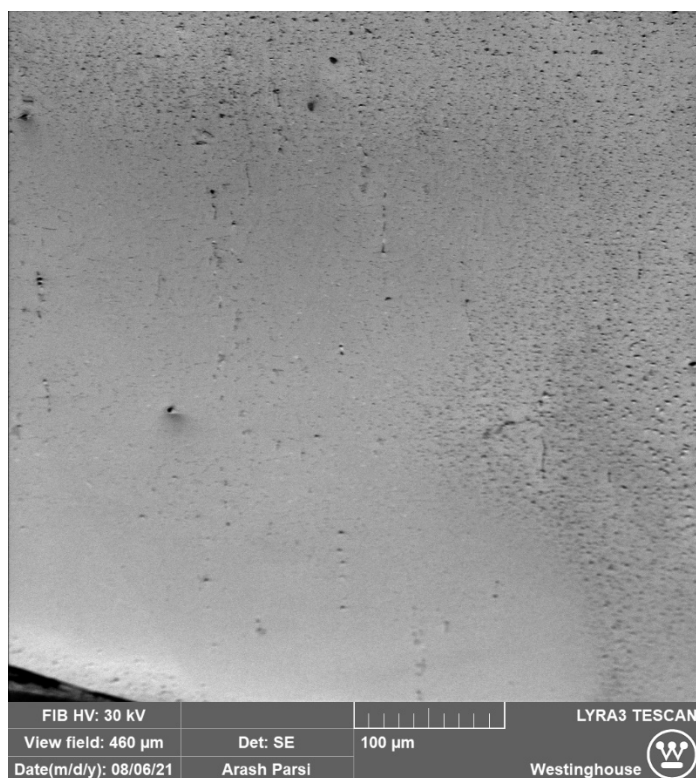


Figure 3-20: Specimen (left) before and (right) after wide-area ion beam polishing

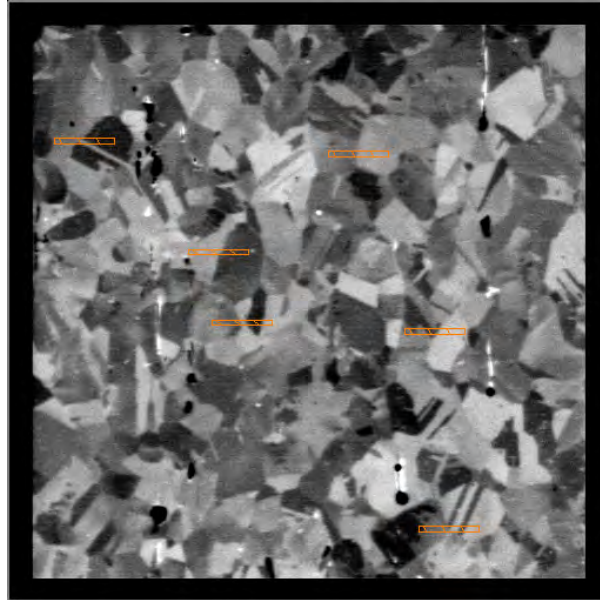


Figure 3-21: Selection of carbon deposition regions, attempting to center grain boundaries under the mask prior to ion milling for lamella preparation

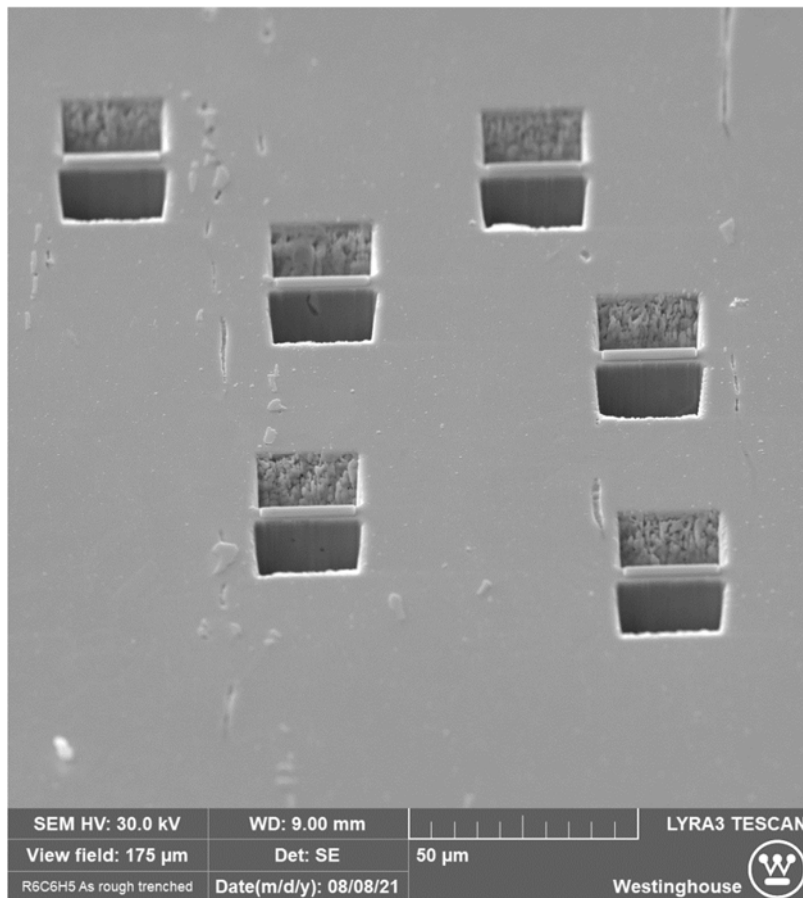


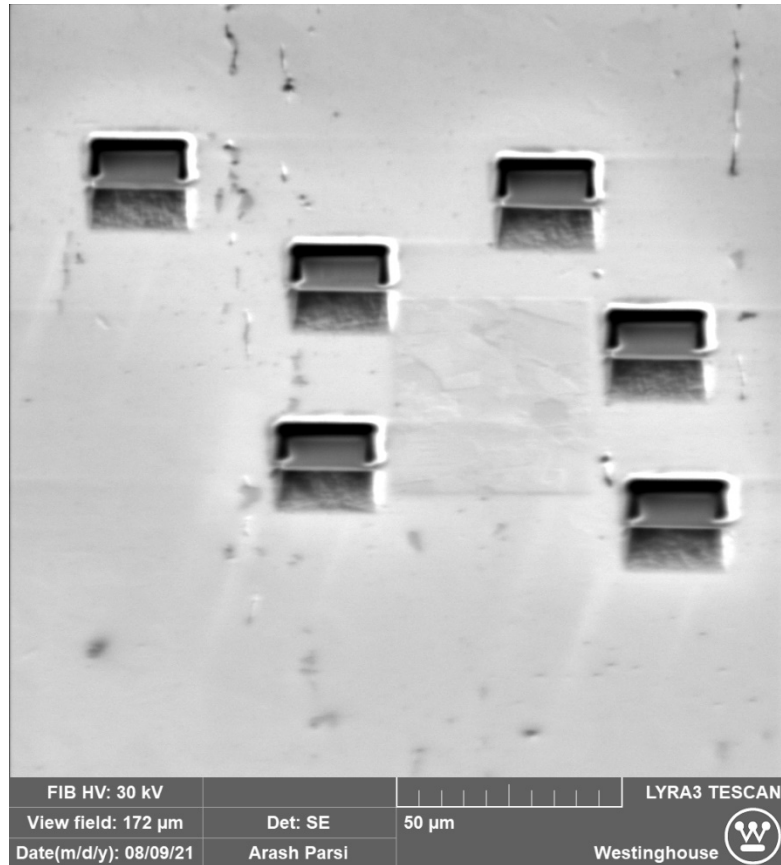
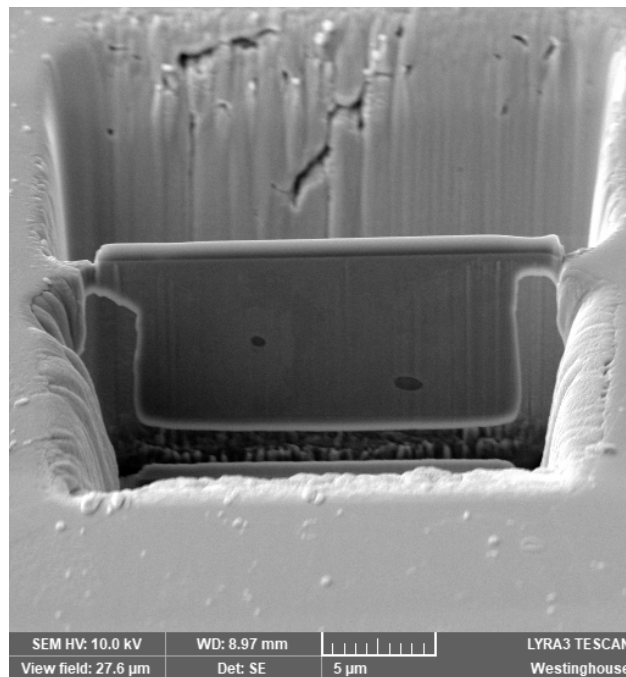
Figure 3-22: Trenches cut around carbon deposits**Figure 3-23: Six undercut lamellas**

Figure 3-24: Undercut lamella containing some apparent inclusions

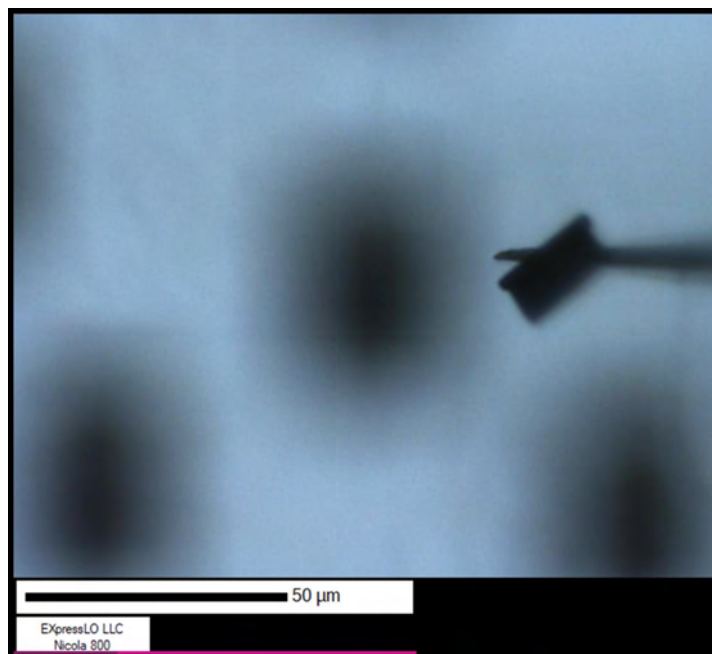


Figure 3-25: Lamella attached to lift-out needle prior to placement on grid (light optical image)

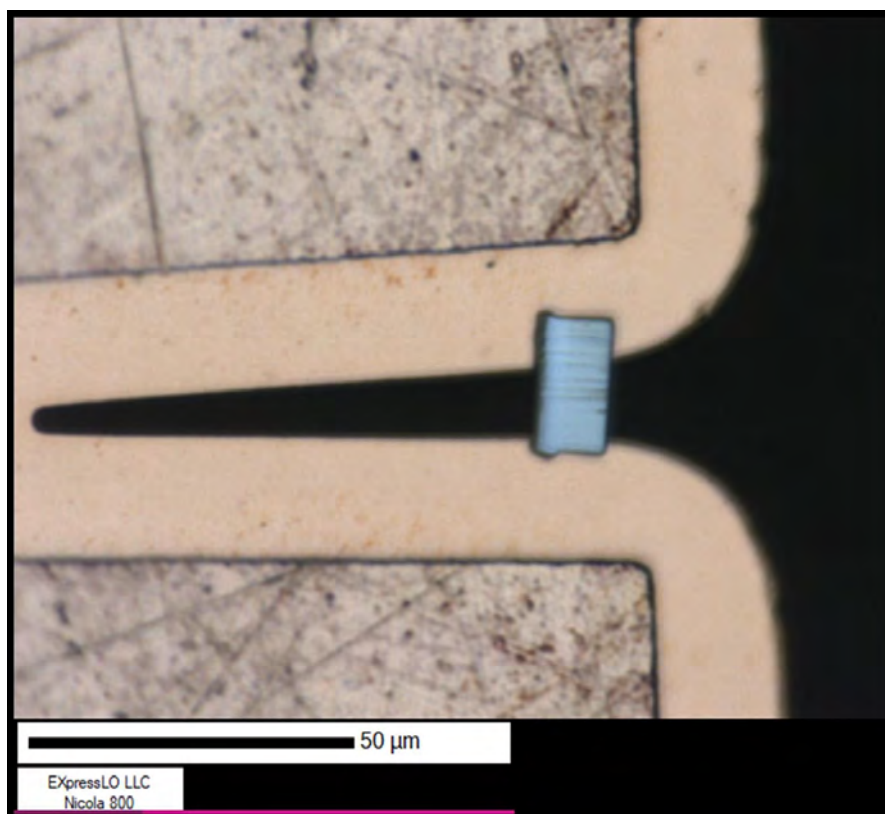


Figure 3-26: Lamella placed on grid (light optical image)

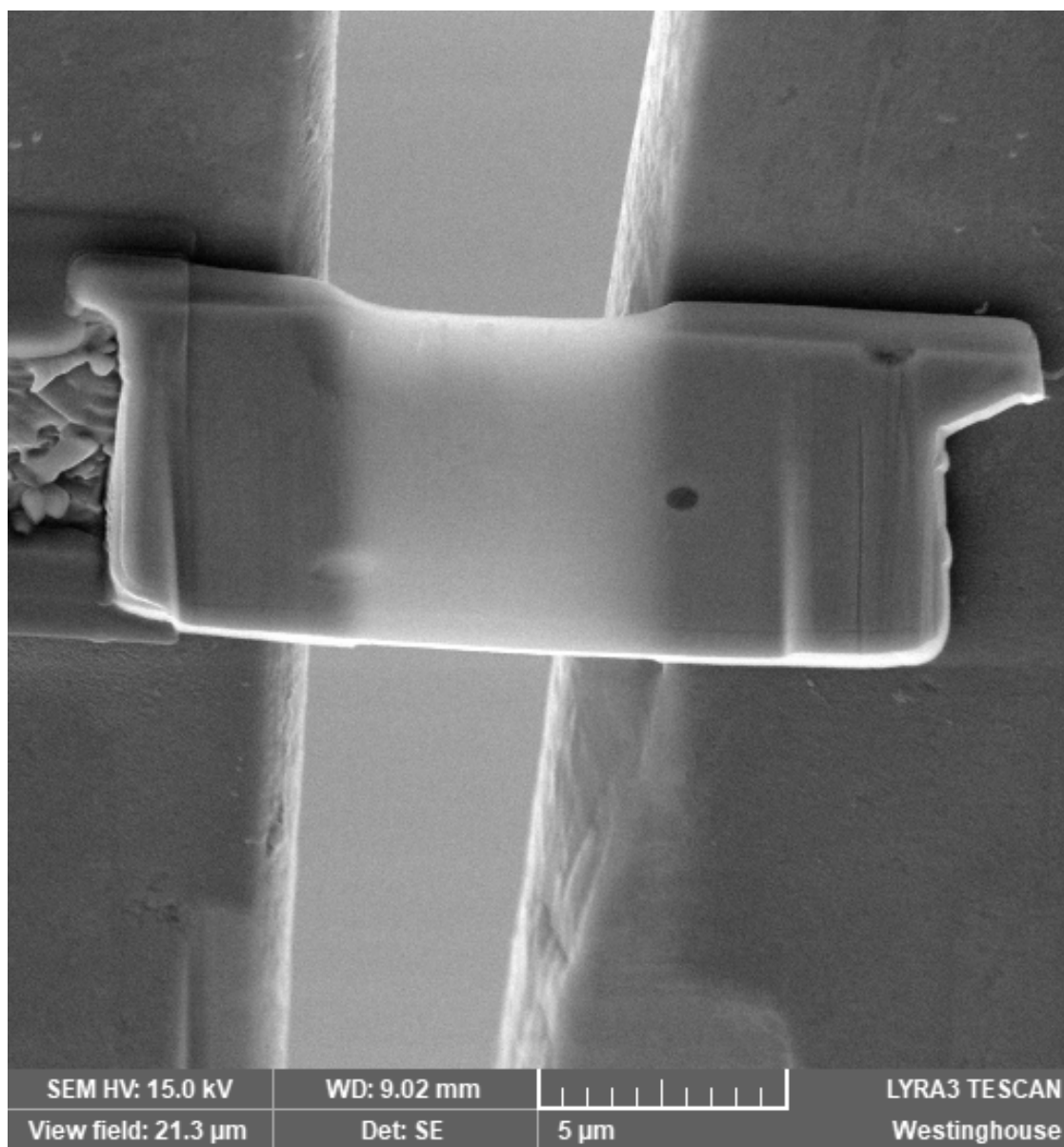


Figure 3-27: Lamella deposited on grid after final thinning (viewed via SEM)

The final length, width, and dose rates of each 4-point bend specimen is recorded in Table 3-4. The dose (dpa) in this table reflects the best-estimate for the as-machined location. As previously discussed, the five specimens with the best surface of the six were selected for testing, while the sixth was used for TEM specimen generation. TEM specimens shipped to University of Michigan are recorded in Table 3-5.

Table 3-4: Final Irradiated 4-point Specimen Identities, Dimensions, and Dose Rates

#	Specimen	Length (mm) [Target 5mm]	Width (mm) [Target 3.5mm]	Dose rate on contact (R/hr.)	Dose rate at 30 cm (mR/hr.)	Best Estimate on dose (dpa)
1	D28-H-1	5.05	3.49	16.2	83	26.4
2	D28-H-2	5.05	3.51	16.2	93	26.4
3	D28-H-3	5.05	3.49	15.6	90	26.4
4	D28-H-4	5.05	3.51	15.1	100	26.4
5	D28-H-5	5.05	3.51	16.1	90	26.4
6	D28-T-1	5.05	3.51	14.5	93	16.5
7	D28-T-2	5.05	3.51	14.1	84	16.5
8	D28-T-3	5.05	3.51	13.9	85	16.5
9	D28-T-4	5.05	3.52	14.8	81	16.5
10	D28-T-5	5.05	3.51	14.2	83	16.5
11	S-R6C6-H-1	5.05	3.48	5.6	33	18.4
12	S-R6C6-H-2	5.03	3.48	5.6	33	18.4
13	S-R6C6-H-3	5.03	3.47	5.5	34	18.4
14	S-R6C6-H-4	5.03	3.48	5.3	36	18.4
15	S-R6C6-H-6	5.08	3.52	5.2	34	18.4
16	S-R6C6-T-1	5.05	3.51	4.8	34	11.5
17	S-R6C6-T-2	5.07	3.49	4.76	35.8	11.5
18	S-R6C6-T-3	5.07	3.51	4.7	29.9	11.5
19	S-R6C6-T-5	5.07	3.51	4.75	32.7	11.5
20	S-R6C6-T-6	5.08	3.51	4.76	29.4	11.5
21	S-R2C6-T-1	5.07	3.52	3.1	24	7.8
22	S-R2C6-T-2	5.09	3.53	3.2	23	7.8
23	S-R2C6-T-4	5.07	3.54	3.5	26	7.8
24	S-R2C6-T-5	5.07	3.56	3.3	26	7.8
25	S-R2C6-T-6	5.11	3.56	3.6	24	7.8

Table 3-5: TEM Specimens Prepared from Baffle-former Bolt Material

Specimen used for Lamella Extraction	Irradiation Level (dpa)	Number of Lamella	Positions on Grid
D28-H-6	26	1 intact (1 damaged)	2, 3
S-R2C6-T-3	8	3	2, 3, 5
S-R6C6-H-5	18	3	2, 3, 5

The 4-point bend specimens were shipped from Westinghouse Churchill Site and received at the University of Michigan on October 27, 2020. The TEM specimens were shipped from Westinghouse Churchill Site and received at the University of Michigan on September 2nd, 2021. No difficulties or irregularities were encountered in either shipment.

4 METHODOLOGY

4.1 IASCC INITIATION TESTING / 4-POINT BEND INTERRUPTED TEST

An interrupted load 4-point bend (4PB) test type was performed to determine the IASCC initiation stress in the sample for each dose level. The method, developed by Stephenson et al. Reference 19, was adopted in this study because it creates a decreasing tensile stress profile through the sample thickness, limiting the growth of the crack and preventing the sample from a through-thickness cracking. Also, the miniature size of the sample helps to overcome the limited amount of such materials exposed to various neutron fluxes and other environmental conditions in PWRs. The setup of loading fixture with the miniature 4PB sample develop a uniform strain area of $0.5 \times 3.5 \text{ mm}^2$ in the center of the convex surface therefore this was the area of interested that was considered as an effective region and thus it was only characterized by the SEM for the IASCC quantification purposes. The loading fixture made of a heat-treated Inconel 718 as shown schematically in Figure 4-1. More details about the loading fixture and sample design and the test procedure can be found in reference 19.

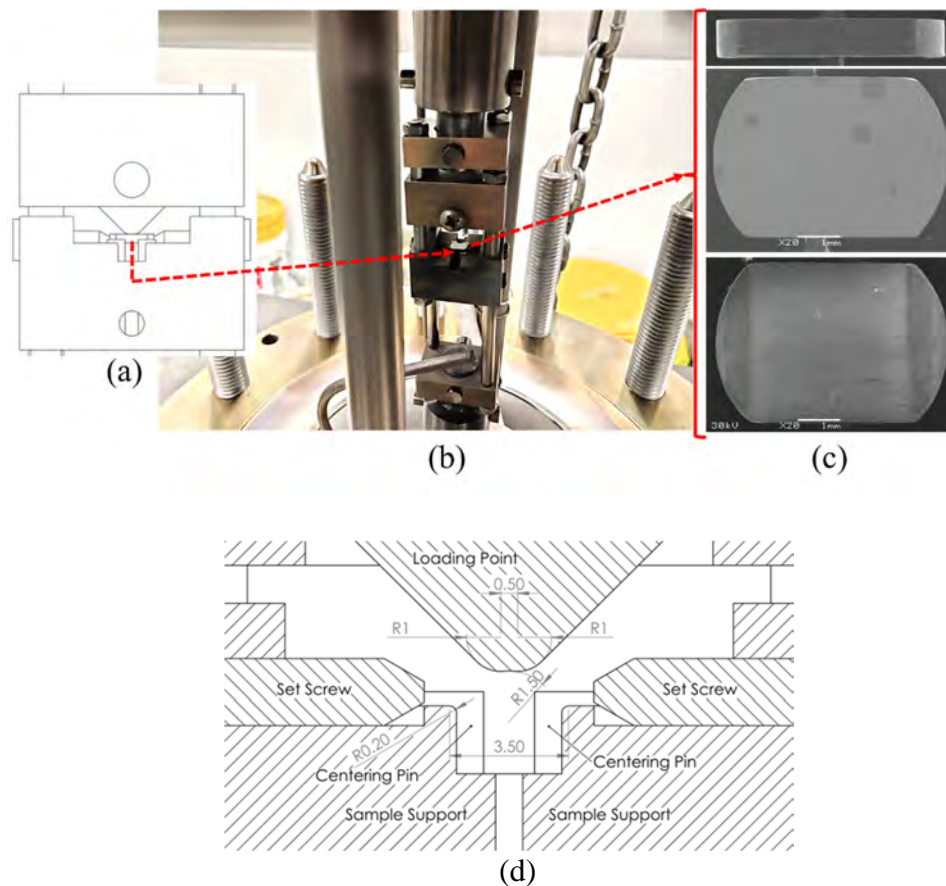


Figure 4-1: Schematic of the 4PB loading fixture, (a) a side view of a conceptual design the loading fixture, (b) The IM2 loading fixture and one of the tested samples, (c) SEM images of an example of side view, surface view without oxidation, and surface view with after 4PB testing, and (d) a side view of the loading fixture with dimensions.

A servo motor was used to apply the load (as a displacement) during 4PB tests to create an effective stress on the sample surface which was limited within the elastic region. The correlation between the applied load and stress was obtained by straining 0.8 mm thick 304SS bend samples with various cold worked levels up to yield. The equation was then established as follows Reference19:

$$\sigma_{eff} = 1.174 \times P, \quad (1)$$

where σ_{eff} is the effective surface stress in MPa formed in the uniform strain region of the convex surface and P is the applied load, in N, on the 4PB sample.

However, this type testing is strongly dependent on the sample thickness. In the case where the thickness varies from one edge of the sample to the other (Reference 20), the applied load will cause a variation in stress on the sample, making it difficult to determine the stress to initiate a crack. The thickness of the sample was ensured to be fixed at 0.8 mm along the transverse direction, however, for samples having a uniform thickness greater than 0.82 mm, the applied load was corrected by the following equation:

$$P_c = \left(\frac{T}{0.8} \right)^2 \times P \quad (2)$$

where P_c is the corrected applied load in N on the four-point bend sample, T is the thickness of the sample in mm and P is the calculated load in N according to Eqn. (1).

The 4PB tests are conducted in an interrupted mode in which the sample is strained at a nominal rate of $4.3 \times 10^{-8} \text{ s}^{-1}$ to an initial applied stress at 40% of the irradiated YS. This low strain rate was used to simulate a slow strain rate test. Test interruptions are employed when the samples are strained to 40%, 50%, 60%, 70% and 80% of the irradiated YS or until cracks initiate. If crack initiation is not observed at 40% of the irradiated YS for the sample with highest dose, the initial stress was adjusted to 50% or 60% for subsequent tests on other samples with lower dose. The uniform strain region after each interruption was examined by the SEM (JEOL JSM-6480) to determine if cracks were initiated by the previous straining step. To further investigate the development of cracks after initiation, some of the samples were strained an additional straining step.

The applied load started from the tare load and then increased to the target load and returned back to the initial setpoint when the target load was achieved (Servo-motor load is released and only tare load is applied). The tare load on the sample with a system pressure of 2000 psi was about 25 - 30% of the yield stress.

The surface deflection was calculated through the deduction of the crosshead displacement from the loading correction factor (Reference 19). After the examination at each interruption, the specimens were loaded to the previous target stress with a higher strain rate of $4.3 \times 10^{-6} \text{ s}^{-1}$ and then switched back to the nominal strain rate ($4.3 \times 10^{-8} \text{ s}^{-1}$) up to the target load. The load on each sample was measured by a load cell that was connected to the pull rod made of Inconel 718. All data for load, temperature, pressure, and conductivity were recorded every 40 seconds using the LabVIEW® program.

4.2 SCANNING ELECTRON MICROSCOPY CHARACTERIZATION OF CRACK INITIATION

Scanning Electron Microscopy was used to identify and quantify cracks in the sample after each interrupted 4PB test. Cracks were first identified by their contrast in the back-scattering electron (BSE) images and then carefully verified at the secondary electron (SEI) mode at the same location. The constant strain region on the sample ($0.5 \times 3.5 \text{ mm}^2$) was first scanned using a macro script that automatically scans the region using BSE mode at 1000x magnification to generate 293 images of ($5.04 \times 3.78 \text{ }\mu\text{m}^2$) as shown in Figure 4-2. These images were carefully analyzed to detect any oxidized GBs or cracks. If cracks were detected, the suspected areas were carefully scanned using high magnification to confirm the existence of IASCC.

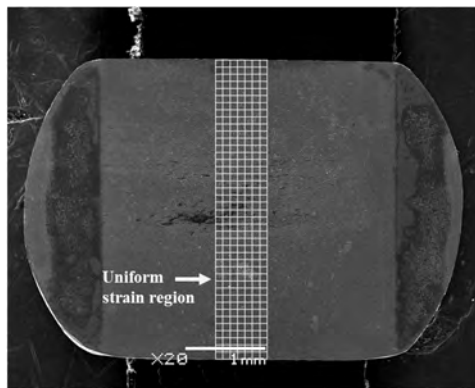


Figure 4-2: SEM image of one of the tested samples that showing the area that scanned with the SEM to detect the IASCC. Each box in the grid represents a $5.04 \times 3.78 \text{ }\mu\text{m}^2$ image and the grid contain 293 images.

Once IASCC is confirmed, selected samples were shipped to the Oak Ridge National Laboratory (ORNL) LAMDA lab, where selected cracks had been machined out of the 4PB samples as lift-outs using Focused Ion Beam (FIB) and then these FIB lift-outs loaded at the Lamella for the TEM analysis.

4.3 OXIDE THICKNESS ROLE ON THE IASCC QUANTIFICATION

The thick oxide film on the surface may lead to an underestimation of the crack initiation stress. To investigate the effect of the oxide on the ability to observe cracks, one of the lowest dose samples was subjected to an oxide removal procedure after crack initiation to compare the crack identified before and after oxide removal. The procedure consisted of two subsequent soaks in water-based solutions: 100 g/L sodium hydroxide with 30 g/L potassium permanganate, and 100 g/L ammonium oxalate. Both solutions were heated to $\sim 95 \text{ }^\circ\text{C}$ and sample was soaked for 5 minutes in each, rinsing and ultrasonically cleaning after each step. The process was repeated for three times until the whole oxide film was removed.

4.4 FINITE ELEMENT ANALYSIS (FEA).

ANSYSTM finite element analysis (FEA) was used to analyze the equivalent stresses distribution at the surface of the sample under both uniform and a non-uniform thickness conditions. Several assumptions were made when creating boundary conditions for the FEA model. Loading points and supports were assumed as round cylinders with a length of 4.0 mm, extending beyond the bend sample width. The widely

spaced below-sample supports were placed 3.5 mm apart, just less than the maximum allowable spacing based on the sample geometry. Loading points and below-sample supports were created as non-deformable rigid bodies, and the contact type between all bodies was defined as frictional with a coefficient of friction equals to 0.2 and the mesh size was 0.04 mm to ensure higher accuracy. Three material conditions were compared in the simulation; one represents the real (experimental) conditions as mechanical properties of S-R2C6-T samples were adopted and the remaining two were used as a reference to validate the simulation results. The simulation input parameters of the materials are summarized in the Table 4-1.

Table 4-1: The input parameters for the FEA simulation

Parameter	Yield Strength (MPa)	Young's Modulus (MPa)	Tangent Modulus (MPa)	Poisson's Ration	Friction Coefficient
Value	996	195000	10000	0.29	0.2

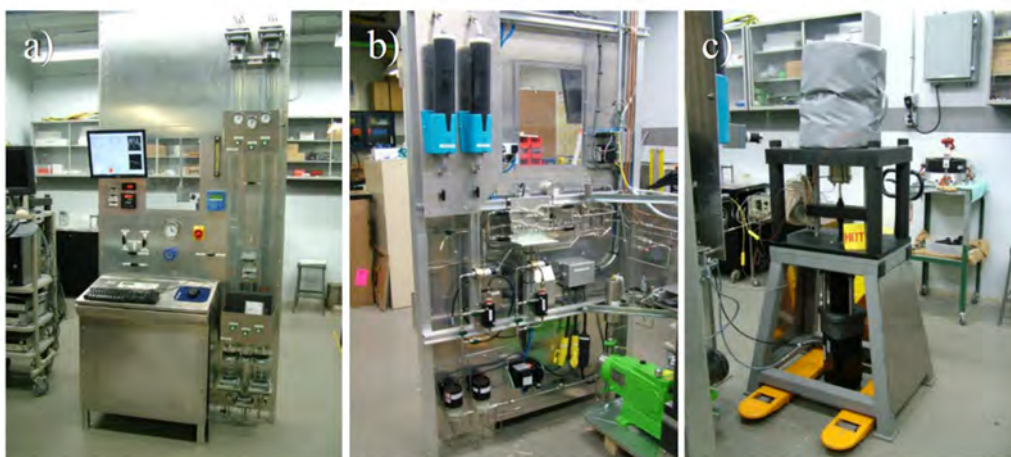
FEA used mainly to evaluate the stress profile at the surface of a sample in case it has a non-uniform thickness along the transverse direction. The sample which was used in the FEA was assumed to have a uniform thickness of 0.8 mm while the other which simulate the non-uniform thickness had a linear profile thickness of 0.02 mm difference between the edges along the transverse direction.

4.5 TESTING SYSTEMS

The 4PB tests were conducted in simulated PWR environments with KOH or LiOH chemistry at the University of Michigan's Irradiated Materials Testing Laboratory (IMTL). Two systems were used for this purpose: IM2 and IM3 (shown in Figure 4-3). These systems allow for mechanical testing of neutron-irradiated materials in specially designed refreshed-water autoclave systems. Each system has two sub-loops such that one is used for conditioning the water at both low temperature and pressure while the second loop is used to simulate the LWR system at high temperature and pressure. Both LiOH and KOH are fully soluble at part per million by weight (ppm) levels in the simulated PWR water. To obtain the same pH level between KOH and LiOH water chemistries, the mole concentrations of $[\text{OH}^-]$ must be kept the same. Therefore, the PWR primary water environment with LiOH was prepared by high-purity water with 1000 ppm of Boron (B) as H_3BO_3 and 2 ppm of Lithium (Li) as LiOH, resulting in a pH of 6.5 – 6.8 and a conductivity of 21.0 $\mu\text{S}/\text{cm}$ at room temperature. Also, the equivalent KOH test environment has a similar pH but a conductivity of 33.0 $\mu\text{S}/\text{cm}$ which was stabilized by addition of 1000 ppm of B as H_3BO_3 and 12.0 ppm of Potassium (K) as KOH. The water conductivity in both water systems were continuously controlled using ion exchangers saturated with K and B for the KOH experiment and Li and B for the LiOH experiment. All four-point bend tests were conducted at 320 °C with a dissolved hydrogen of 35 cc/kg. Pressure and conductivity were monitored at the autoclave inlet and outlet, and the temperature was monitored by a thermocouple in the water with a probe located at the sample height level. The summary of the testing water parameters is listed in Table 4-2.

Table 4-2: The summary of water parameters and strain rate for the four-point bend .

Parameter	PWR-LiOH	PWR-KOH
Temperature (°C)	320	
Pressure (MPa)	13.7 (~ 2000 psi)	
Inlet Conductivity (μS/cm)	21	33
H ₂ concentration (cc/Kg)	35	
O ₂ concentration (cc/Kg)	<5	
Boron as H ₃ BO ₃ (ppm)	1000	
Lithium LiOH (ppm)	2	0
Potassium as KOH (ppm)	0	12
pH at room temperature	6.5 – 6.8	
Nominal strain rate	$4.3 \times 10^{-8} \text{ s}^{-1}$	

**Figure 4-3: Images of the autoclave test system and water loop. a) control panel front, b) control panel back with plumbing and sensors, and c) load frame, motor, and autoclave.**

4.6 INITIATION STRESS DETERMINATION AND THE CRACKING CRITERIA

The stress level at which IASCC initiates was determined by the stress to create an observable crack at a magnification in the SEM of 5000x. However, since the stress is incremented in units of 0.1YS, the crack may have formed at any stress above the last increment at which no crack was observed and the stress at which it was observed. Therefore, the crack initiation stress is reported as the stress at which the crack was observed, with an error bar down to 0.1YS below that stress. The initiation stress correction is a conservative process to ensure accuracy while reporting the results.

Since the surface oxide relatively thick in all samples, it was not easy to detect microstructural features that may participate in the initiation process. Tracking the oxidized GBs was complicated for the same reason. In most cases, cracks appeared after the latest straining step but it was often difficult to distinguish between the crack and the oxidized GBs. Therefore, the criterion for the cracking was simple such as any straight, thick, and bold line that can be seen clearly in both the BSE and SEI modes will be considered as a crack, otherwise, it is an oxidized GB. It was noted that many oxidized GBs can be clearly seen in BSE mode, but switching to SEI mode revealed little, as only a compact oxide film can be seen at the same position. In the case of cracking, a straight bold line can be seen in both SEM modes (and in SEI at magnification $< X5000$). So by considering the thick surface oxide, the bold line that penetrates the thick surface layer should be a crack.

A quantitative process was also used to aid in crack determination. Intensity profiles were created going across suspect grain boundaries. Figure 4-4 shows such a profile for an uncracked, but oxidized grain boundary. Figure 4-5 shows the profile of a cracked grain boundary, with characteristic peaks in the profile emphasized by arrows.

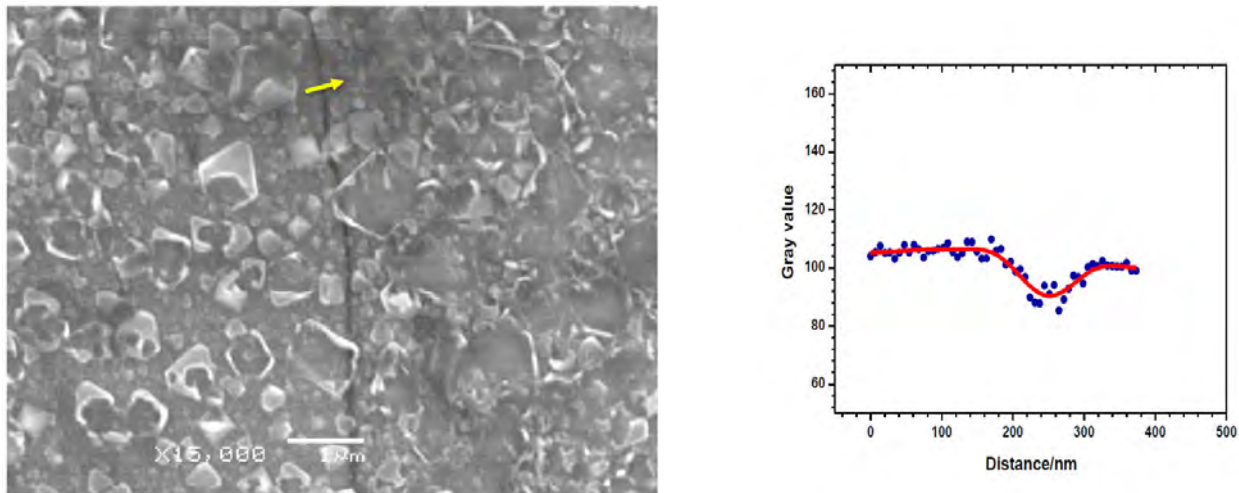


Figure 4-4: Intensity profile (right) across an oxidized grain boundary (left).

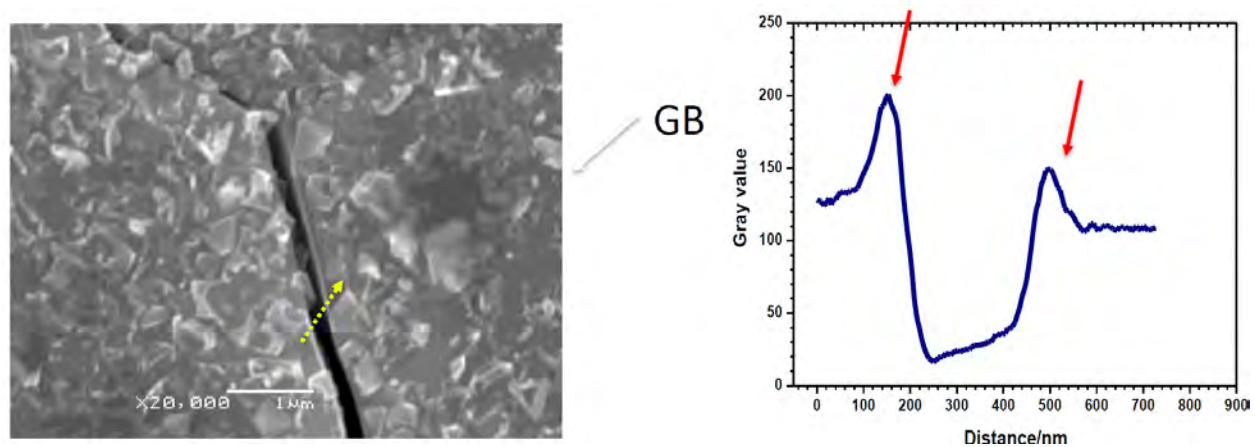


Figure 4-5: Intensity profile (right) across cracked grain boundary (left). Red arrows indicate intensity profile peaks associated with exposed corners of the grain.

4.7 TRANSMISSION ELECTRON MICROSCOPY ANALYSIS OF IG CRACKING

4.7.1 Sample Preparation

Two groups of 347 alloy samples were studied; one that was not strained in water and was used to characterize the irradiated microstructure, and a group that was strained to the point of crack initiation and was used to characterize the oxidized and/or cracked grain boundaries. Three neutron irradiated samples were used to characterize the irradiated microstructure; R2C6T3 (8 dpa), R6C6H5 (18 dpa) and D28H6 (26 dpa). Four neutron irradiated samples were used to characterize oxidized grain boundaries and/or cracks; D28-H-1 (26.4 dpa in LiOH) and D28-H-3 (26.4 dpa in KOH), and S-R2C6-T-1 (7.8 dpa in KOH) and S-R2C6-T-4 (7.8 dpa in LiOH), respectively. Three FIB liftout grids were received from Westinghouse with 8 liftouts attached (see details in Table 4-3). Those FIB-lift out lamella were further thinned after having been checked in a TEM (Figure 4-6 through Figure 4-8).

Table 4-3: FIB liftouts from the three neutron irradiated materials.

Materials	dpa	# Lamella	Positions on Grid
D28H6	26	1 intact (1 damaged)	2, 3
R2C6T3	8	3	2, 3, 5
R6C6H5	18	3	2, 3, 5

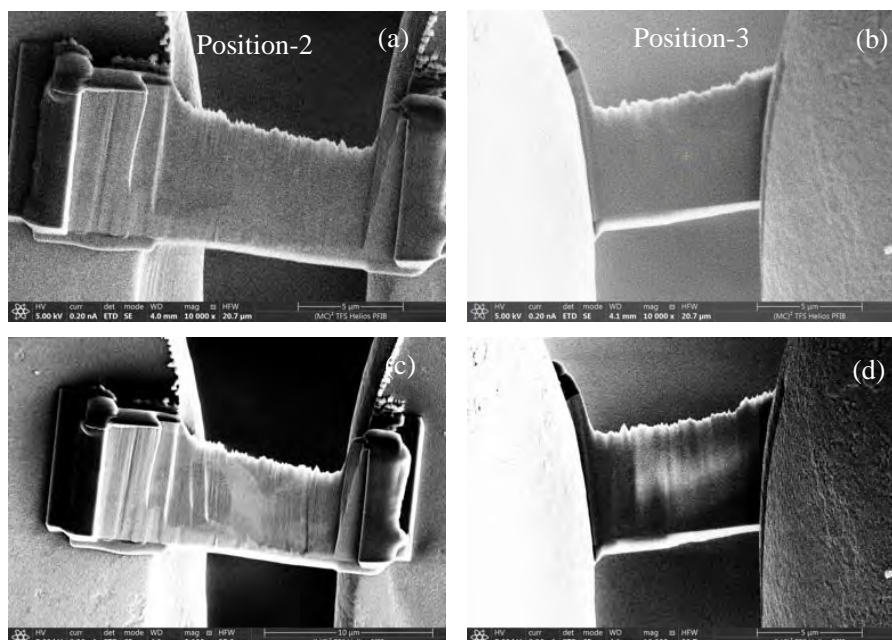


Figure 4-6: (a) and (b) show the two lamellas from the material D28H6 on the position 2 and 3 of the FIB grid; (c) and (d) show the two lamellas after having been further thinned.

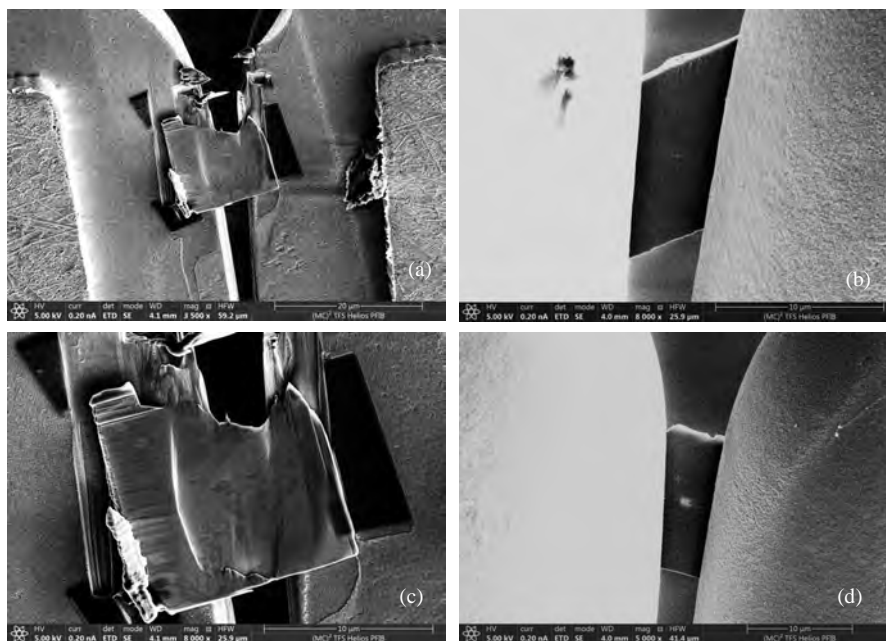


Figure 4-7: (a) and (b) show the two lamellas from the material R2C6T3 on the position 2 and 5 of the FIB grid; (c) and (d) show the two lamellas after having been further thinned (The liftout on the position 3 was missing).

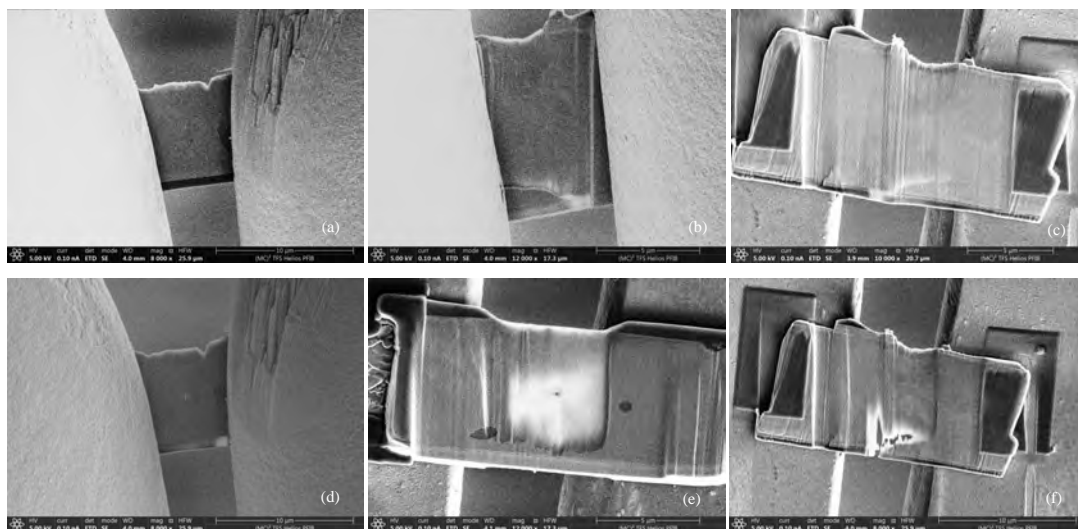


Figure 4-8: (a), (b) and (c) show the three lamellas from the material R6C6H5 on the position 2, 3 and 5 of the FIB grid; (d), (e) and (f) show the three lamella after having been further thinned.

The lift-outs from the neutron irradiated and strained materials were first cut and transferred to FIB grids with thickness of $\sim 1.5 \mu\text{m}$ at 30 keV at LAMDA facility in ORNL using a FEI Versa FIB-SEM. The lift-outs were further thinned at the Michigan Center for Materials Characterization (MC2) at the UM using a

Thermo-Fisher Helios 650 Xe Plasma FIB-SEM at 30 keV down to about 150nm and were finally thinned at 5 keV to reduce FIB damages induced at high beam energy.

4.7.2 Microscopy and microchemistry characterization by TEM

A Thermo-Fisher TF 30 TEM operated in CTEM mode at 300 keV was used for Frank loops imaging using a rel-rod dark-field (rdDF) technique with $g = 1/2\{311\}$ (Reference 19). The number of loops from such a DF image (1024 pixels x1024 pixels) were counted using Gatan DigitalMicrograph software from which the total loop number was obtained by multiplying the counted number by a factor of 2. The sizes of the loops were measured from a DF image. Loop sizes smaller than 4 nm were excluded as it was difficult to separate them from the precipitates or FIB damages/redepositions, and they constituted no more than 10% of the total loop population. A Talos F200 at MC2 with both operated in STEM mode at 200keV was used for imaging the precipitates and radiation induced segregation (RIS) at grain boundaries (GBs). The Talos is equipped with four 30mm² SDD EDS detectors that can give strong X-ray signals for STEM spectrum imaging using X-ray signals (STEM-SI EDS). The thickness of the liftout foils was measured using electron energy loss spectroscopy (EELS) in the Talos.

5 RESULTS

5.1 FOUR-POINT BEND TEST RESULTS OF 347 SS IN KOH WATER CHEMISTRY.

5.1.1 Sample loading history

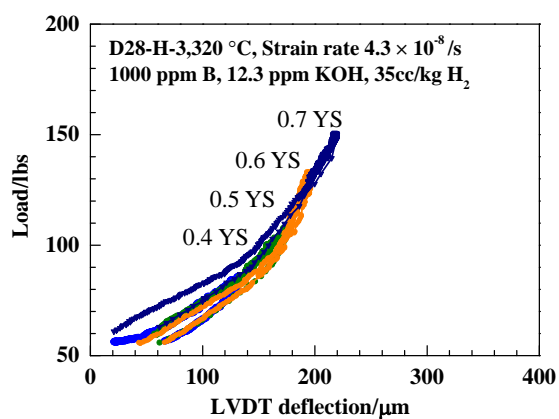
Eight samples were tested in KOH water chemistry. The data of the load versus LVDT displacement (or crosshead displacement) were collected after each interrupted 4PB test, as shown in Figure 5-1. Since IASCC is likely to initiate at low YS loads when the damage level is high, the sample D28-H-3_26.4 was strained first in a KOH environment to 0.4YS as shown in Figure 5-1(a). The post-experiment SEM characterization showed no detectable oxidized grain boundaries (GBs) or crack initiation in the uniform strain region. Therefore, further straining to 0.5YS was performed and no evidence of cracks initiation was observed there as well. The sample was then strained to 0.6YS and 9 cracks were observed at this loading level. Although the IASCC in this sample was found at 0.6YS, an additional load increment to 0.7YS was performed to understand the crack evolution with load. This additional increment resulted in another 13 cracks that were observed at the sample surface.

Figure 5-1(b) shows the interrupted test results of S-R6C6-H-4_18.4. Since no cracks were found at 0.4YS whereas several IASCCs initiated at 0.6YS in the D28-H-2_26.4, the sample that has higher damage level (dpa), then the sample S-R6C6-H-4_18.4 was strained first at 0.5YS and no IASCC initiation were observed. However, 3 cracks were found after straining to 0.6YS.

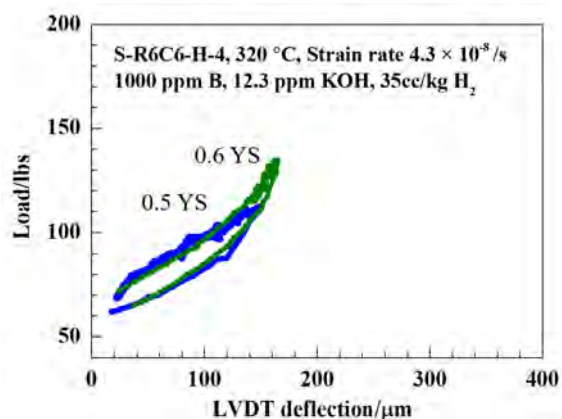
All 4PB interrupted tests followed the same procedure and the IASCC initiation was observed at: 0.6YS in S-R6C6-T-5_11.5 as shown in Figure 5-1(c), 0.8YS in S-R6C6-T-3_11.5 as shown in Figure 5-1(d), 0.6YS in S-R2C6-T-1_7.8 as shown in Figure 5-1(e), 0.8YS in S-R2C6-T-2_7.8 as shown in Figure 5-1(f), and 0.7YS in D28-T-2 as shown in Figure 5-1(h).

The SEM was used to determine and track the oxidized GBs, dislocation channels (DCs), or cracks. It was important to track all microstructural features that are responsible in cracking initiation at each loading step. However, this was not achievable in this study due to the relatively thick surface oxide film. The thickness of the oxide was believed to underestimate the crack quantification process. Therefore, to determine the actual crack density, one of the samples (S-R2C6-T-2_7.8, with five cracks observed after straining to 0.8YS) was subjected to an oxide removal process. SEM analysis after the oxide removal showed another 2 cracks at the surface raising the cracks number to 7 which indicates that the SEM observation on the oxidized surface is still a valid method of determining the IASCC initiation stress level, which is the main purpose of this study, but it may not represent the accurate crack density on the sample's surface.

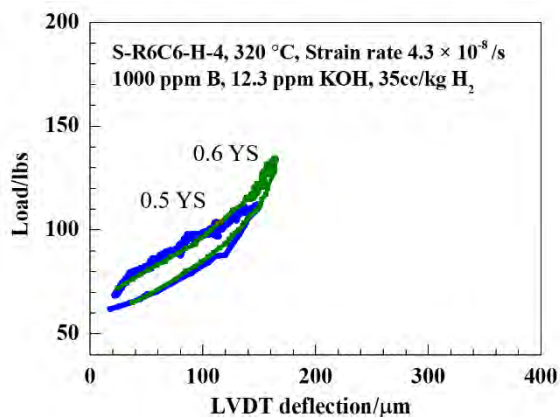
Figure 5-2 shows the distribution of the detected cracks in the eight 4PB samples tested in the KOH environment. The size of cracks is small (a few microns) which makes the SEM scanning at low magnification difficult. Therefore, a careful observation at high magnification (>1000X) was adopted to best quantify the IASCC initiation. The cracks in the figure are distributed in the uniform region and were highlighted by a yellow line. It should be noted that the uniform distribution of cracks supports the uniformity of thickness of the sample across the transverse direction, while samples exhibiting a density of cracks at one edge indicates a nonuniform thickness and therefore a potentially uneven stress distribution across the sample. This result also supports the FEA analysis that showed that the maximum equivalent stresses are concentrated at one edge (thicker one) as this region might have undergone plastic deformation especially at higher YS stress levels.



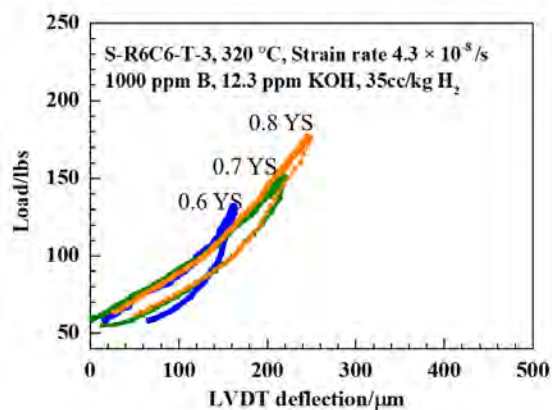
(a)



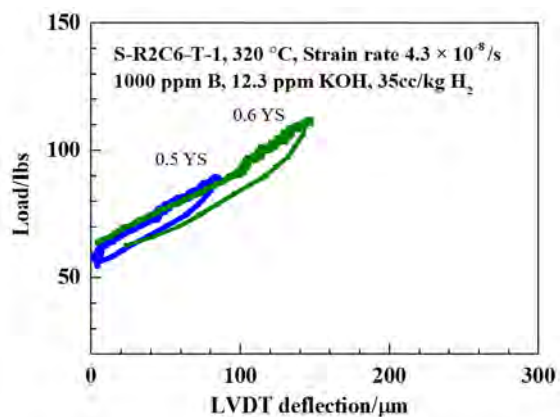
(b)



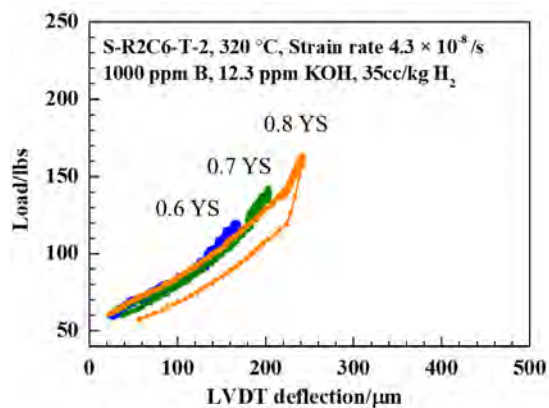
(c)



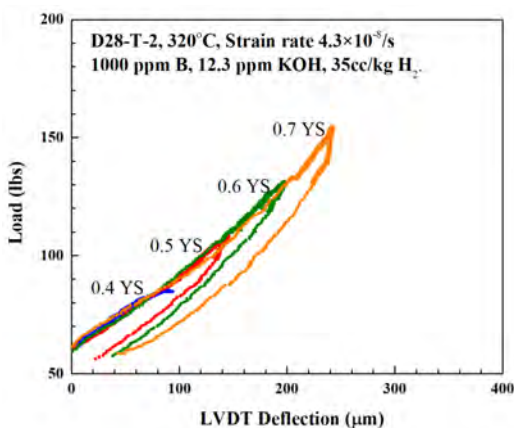
(d)



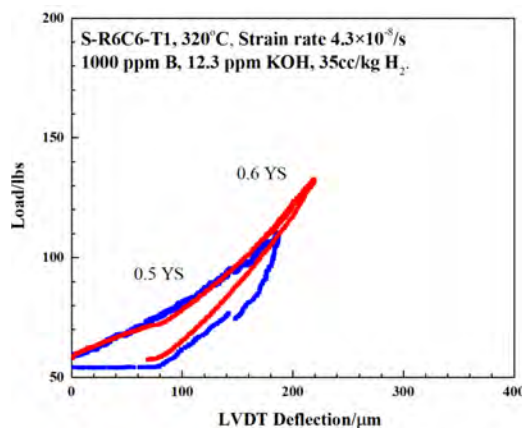
(e)



(f)



(g)



(h)

Figure 5-1: Load versus LVDT displacement for the samples tested in KOH water chemistry. The IASCC initiation in (a) D28-H-3_26.4 were observed after straining to 0.6YS, (b) S-R6C6-H-4_18.4 were observed after straining to 0.6YS (c) S-R6C6-T-5_11.5 were observed after straining to 0.6YS (d) S-R6C6-T-3_11.5 were observed after straining to 0.8YS (e) S-R2C6-T-1_7.8 were observed after straining to 0.6YS (f) S-R2C6-T-2_7.8 were observed after straining to 0.8YS (g) D28-T-2_16.5 were observed after straining to 0.7YS, and (h) S-R6C6-T-3_11.5 were observed after straining to 0.8YS.

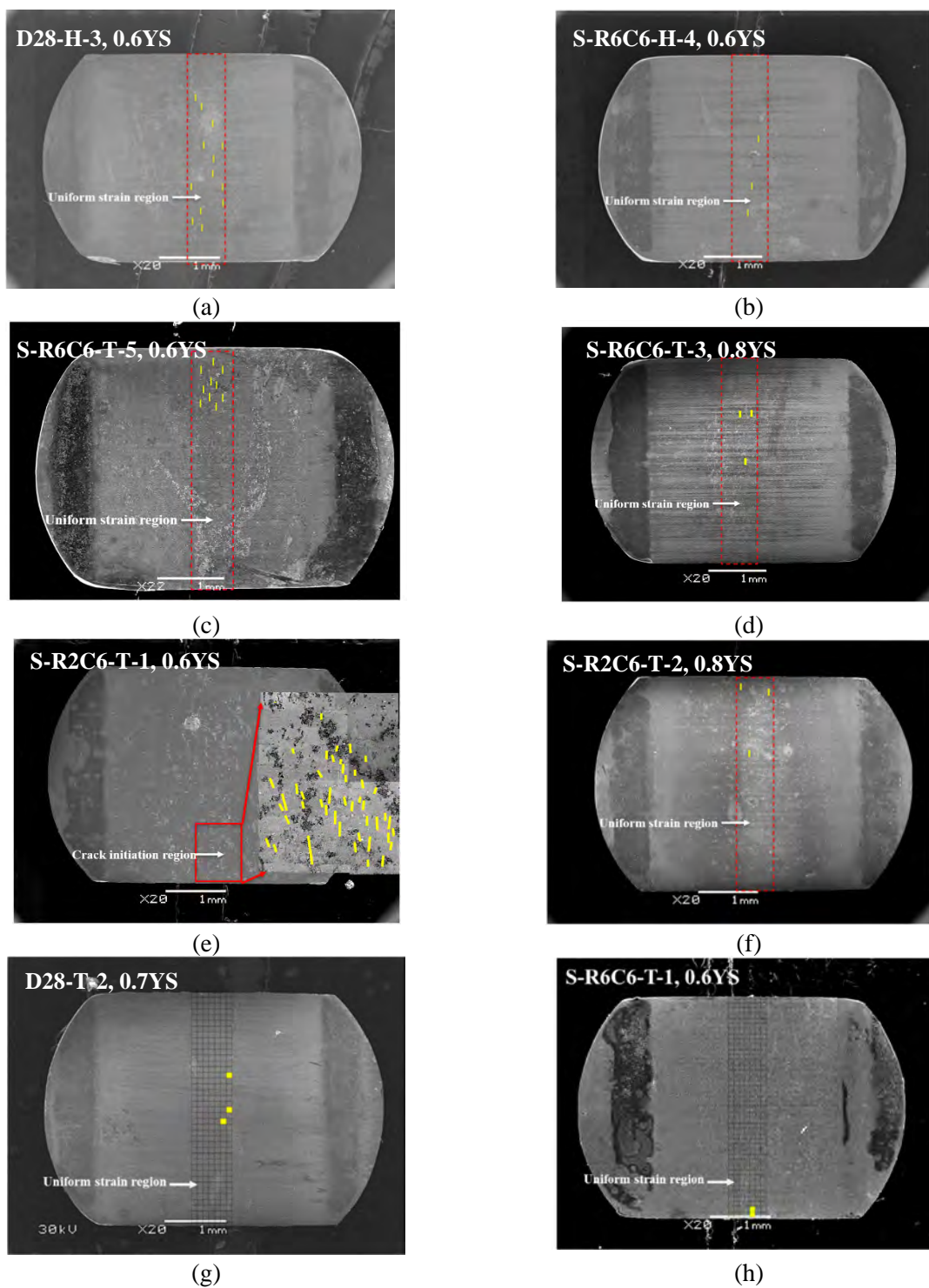


Figure 5-2: Morphologies of 4PB samples after final bending tests in the KOH water chemistry.

5.1.1 Characterization of cracks

Table 5-1 summarizes the crack initiation stress, number of cracks, average crack length, crack density, and crack length per unit area in samples tested in the KOH water chemistry.

The average crack length in D28-H-3_26.4 is 24.7 ± 2 μm , which is typically larger than the grain size of 347SS in this study, indicating that the cracks may have initiated in the previous step but were too shallow to be observed using the SEM. Alternatively, they could have initiated in the early stage of the last straining step. For the sample S-R6C6-H-4_18.4, the average crack length and density are 16.2 ± 1.2 μm and 1.7 $\mu\text{m}/\text{mm}^2$, respectively, which are smaller than those detected in D28-H-3_26.4. Furthermore, 10 cracks initiated from the oxidized grain boundaries on S-R6C6-T-5_11.5 with average crack length of 10.7 ± 0.21 μm , indicating the initiated cracks were restricted to one or two grains. The repeat sample at 11.5 dpa showed higher stress initiation as expected and the average crack length and density at 0.8 YS are 9.0 μm and 15.3 ± 3.1 $\mu\text{m}/\text{mm}^2$, respectively. Another repeat sample (S-R6C6-T-1_11.5) that has a non-uniform thickness showed again a lower stress initiation at 0.6YS with only one crack was observed at the thicker edge with length of 5.5 μm and density of 0.6 $\mu\text{m}/\text{mm}^2$. One of the samples with lowest irradiation level in this study (S-R2C6-T-1, 7.8 dpa) was first strained to 0.5YS, resulting in no IASCC initiation in the constant strain region. After straining to 0.6YS, 40 IG cracks were observed in one edge only. The average crack length was 40.8 μm . This result showed the effect of the thickness non-uniformity on the cracking behavior during the straining event. A repeat test was performed on S-R2C6-T-2_7.8 that had a more uniform thickness, and as expected, IASCC initiation stress increased to 0.8 YS and the average crack length is less than 10 μm indicating the crack did not grow substantially.

Figure 5-3 shows a representative crack from sample D28-H-3_26.4 that initiated at 0.6YS and its evolution after straining to 0.7YS. The crack is IG, which is the dominant cracking mode in all samples, and at an angle of 70° to the applied stress. As a higher load was applied to this sample, the crack width and length were increased according to the BSE images. Unfortunately, microstructural features such DCs was not observed due to the thick surface oxide film.

Table 5-1: Crack statistics for the sample exposed to the KOH environment.

Sample ID Parameter	D28-H-3		S-R6C6- H-4	D28-T-2	S-R6C6- T-3	S-R6C6- T-5	S-R6C6- T-3	S-R2C6- T-1	S-R2C6- T-2
Average thickness (mm)	0.8		0.8	0.8	0.8	0.81	0.81	0.735-0.765	0.8
Damage level (dpa)	26.4		18.4	16.5	11.5	11.5	11.5	7.8	7.8
Yield stress (MPa)	1089		1082	1077	996	1050	1050	996	996
Crack initiation Stress	0.6		0.6	0.7	0.6	0.6	0.8	0.6	0.8
Applied stress (% YS)	0.6	0.7	0.6	0.7	0.6	0.6	0.8	0.6	0.8
Number of cracks	9	13	3	3	1	10	3	40	5
Average crack length (μm)	24.7 ±2.0	45.6 ±1.5	16.2±1.2	9±0.30	5.5±0.19	10.7±0.21	9.0±0.32	45.8±0.54	8.23±0.5
Crack density (#cracks/mm²)	5.2	7.4	1.7	1.74	0.6	5.8	1.7	26.2	2.9
Crack length/unit area (μm/mm²)I	133.7 ±33.6	337.6 ±28.9	27.6 ±5.4			70.0±1.9	15.3±3.1	3338.8 ±227.8	23.5±2.5

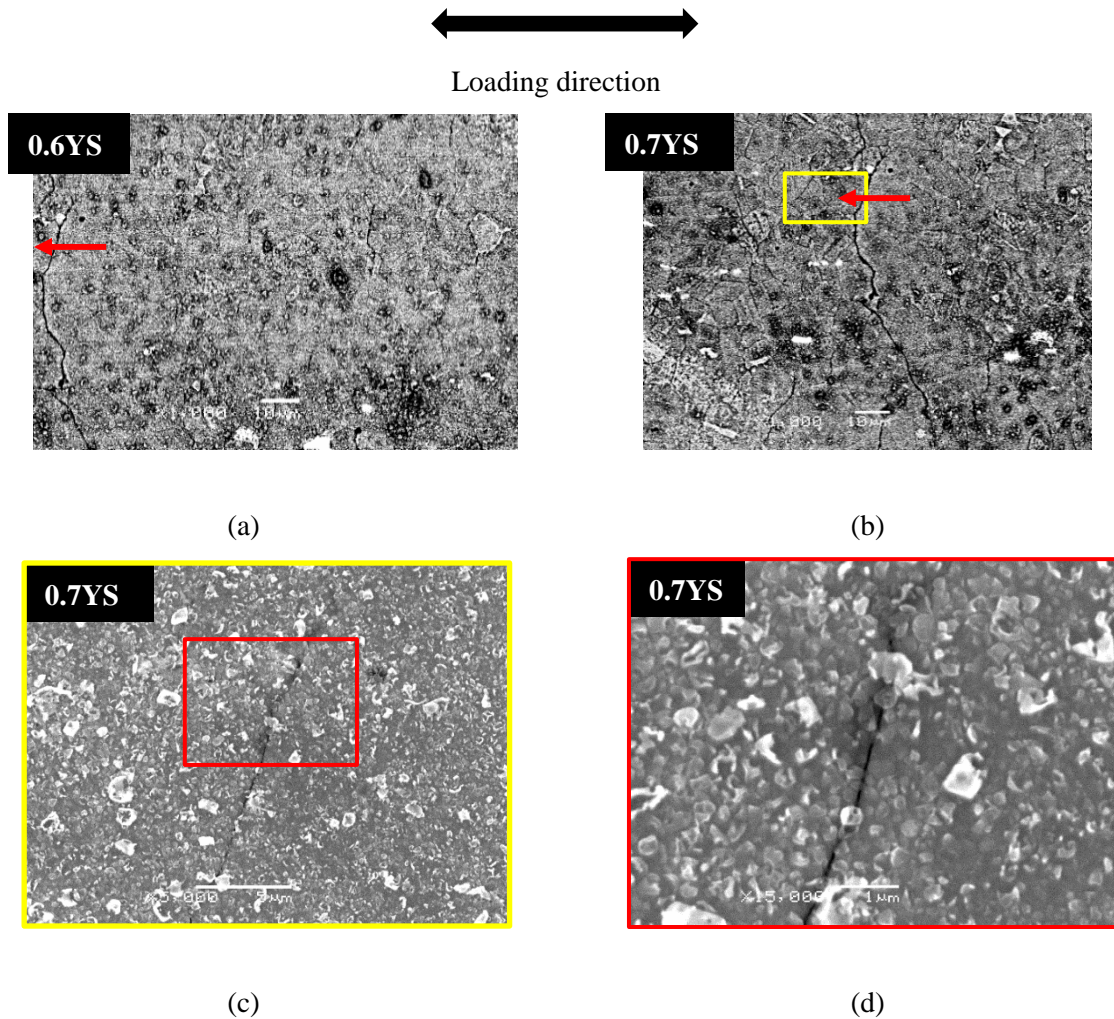


Figure 5-3: A representative crack from sample D28-H-3_26.4 (a) BSE image at 0.6 YS, (b) BE image of the same region at 0.7YS, (c) and (d) magnified SE image of the crack initiation site.

Another IASCC example can be seen in Figure 5-4 which was initiated at 0.6YS in S-R6C6-H-4_18.4. Figure 5-5 shows a region containing more than one initiated crack in S-R6C6-T-5_11.5 in KOH water chemistry at 0.6YS. The cracks are shallow and restricted to one grain. Interestingly, these cracks did not combine though the adjacent grain boundary was severely oxidized, as shown in Figure 5-5 (c) and (d). The triple junctions of the cracks were heavily oxidized.

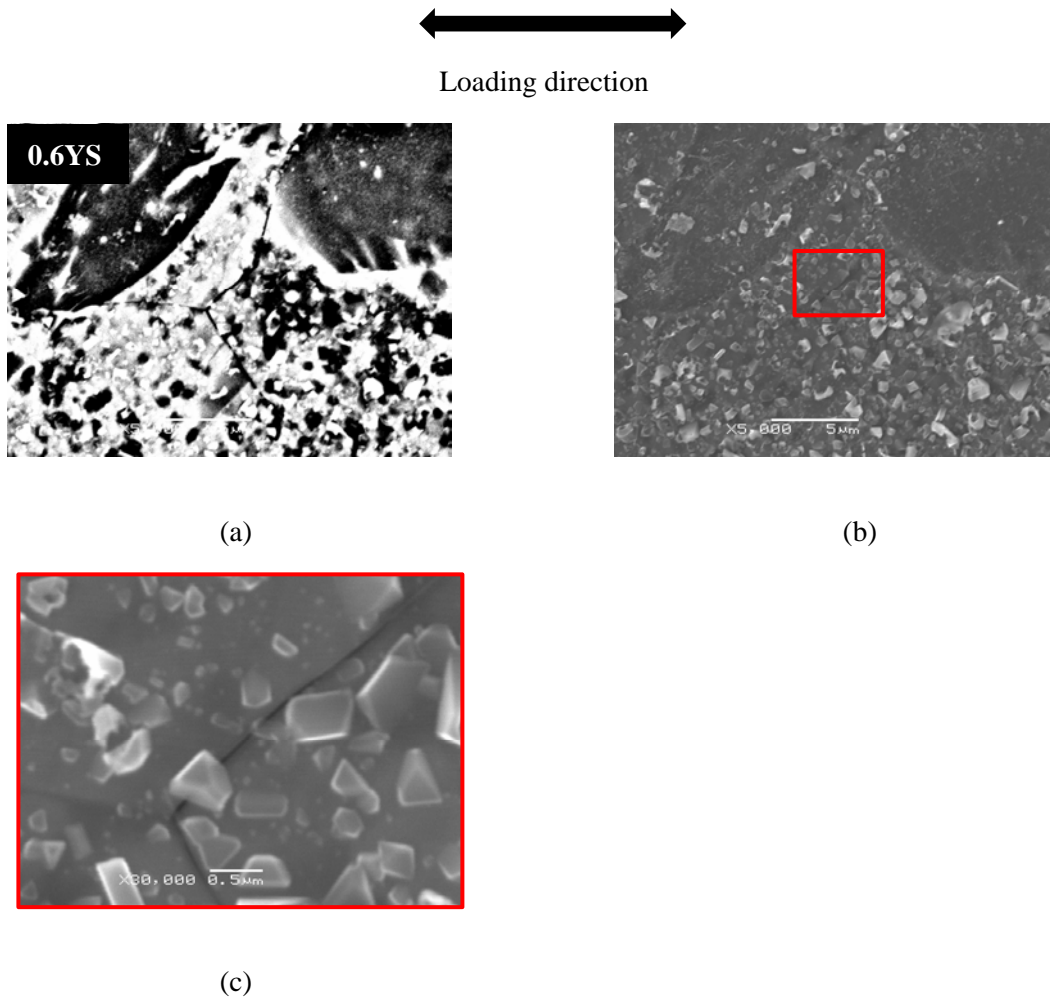


Figure 5-4: A representative crack from sample S-R6C6-H-4_18.4 at 0.6 YS. (a) BSE image, (b) SE image of the same region, (c) magnified picture of the crack initiation sites (Red Box in (b)).

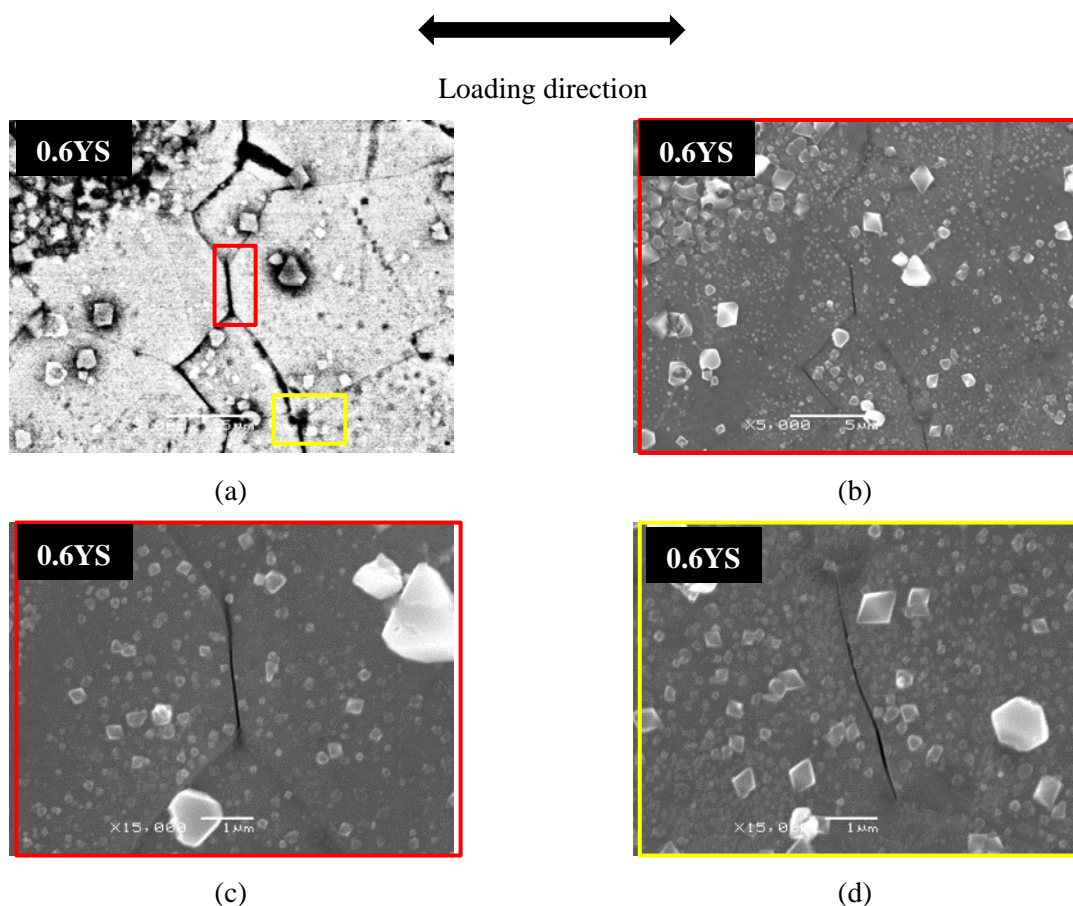


Figure 5-5: Representative cracks from sample S-R6C6-T-5_11.5 at 0.6 YS. (a) BSE image (b) SE image of the same region, (c) and (d) magnified SE image of the crack initiation sites.

Figure 5-6 shows how the crack initiated on S-R6C6-T-3_11.5 in KOH water chemistry. At 0.7YS, GBs are visible in the oxidized form (indicated by the black arrow in Figure 5-6 (b)). A careful tracking of the same GB but at 0.8YS revealed a very small IG crack as shown in Figure 5-6 (d). In addition, some of the particles formed at 0.7YS dissolved after further exposure.

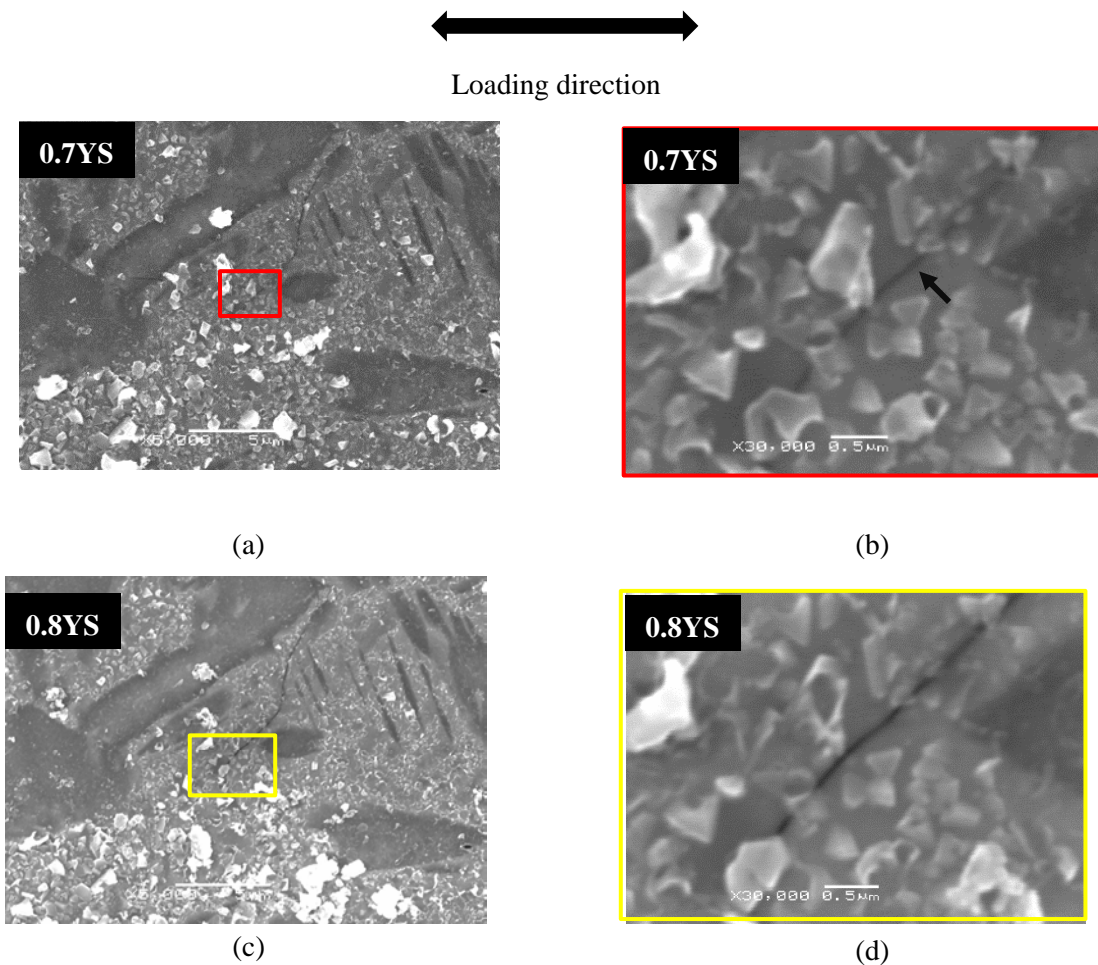


Figure 5-6: Representative cracks from sample S-R6C6-T-3_11.5 at 0.6 YS. (a) BSE image (b) SE image of the same region, (c) and (d) magnified SE image of the crack initiation sites.

Figure 5-7 shows the condition of a crack in a sample with non-uniform thickness. The crack is relatively large with length of 200 μm (the largest one in this study) starting at the edge of the sample, indicating that its initiation was likely caused by the stress concentration at the edge.

It was found that S-R2C6-T-1 has a transverse linear profile thickness of 0.02 mm difference between the two edges (using SEM measurements on the edges). To understand the stress profile at this sample surface, an FEA analysis was performed to simulate this sample condition using ANSYS 2021 R2 ®. The result of the FEA, Figure 5-8, supports the experimental result as the total equivalent stresses are concentrated at one edge, obviously the thicker one. The results show that during the 4PB testing, the thicker edge was exposed to a load that was higher than the target load by 10 – 20% of the irradiated YS. For example, this sample had been exposed to 0.6YS (~ 598 MPa) but due to the non-uniform thickness, when the target load of 0.6YS is reached it will not be distributed uniformly along the transverse direction of the sample. The stress would likely be 0.6YS at the thinner edge while it may reach 0.8 – 0.9YS or more at the thicker edge where plastic deformation might be expected. Even if the load did not reach the plastic level, it is still

expected that the thicker edge would show cracks if actual loading reached 0.8YS (The upper limit of IASCC initiation in this study). Moreover, the comparison between this sample and the repeated one (S-R2C6-T-2) the sample with a uniform thickness showed that the repeated one showed IASCC starting from 0.8YS (number 3 cracks were observed). Therefore, the crack densities along with the FEA result could indicate that the S-R2C6-T-1 sample was exposed to a loading of magnitude of at least 80-90% of the YS of the material.

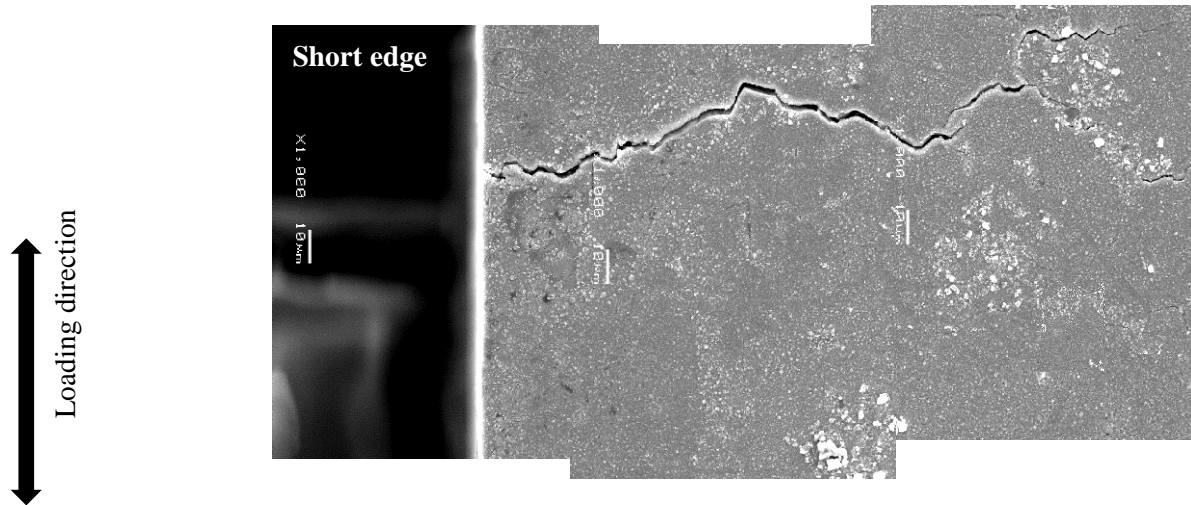


Figure 5-7: The largest crack from sample S-R2C6-T-1_7.8 dpa at 0.6 YS.

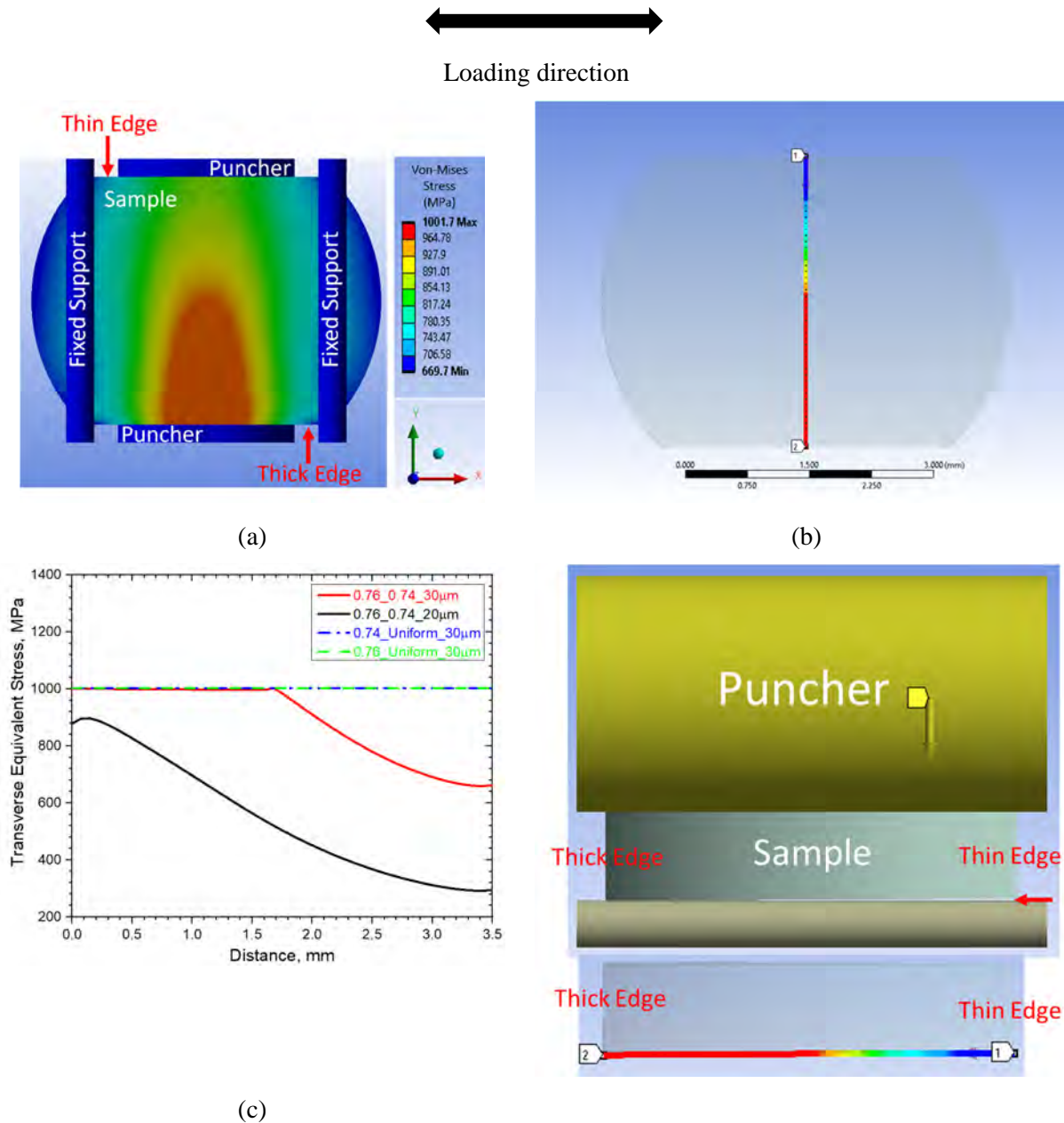


Figure 5-8: (a) the total equivalent stresses at the surface of a non-uniform 4PB samples (S-R6C6-T-1_7.8 simulated) with a change in thickness of 20 μm between short edges, (b) the equivalent stresses profile along the transverse edge, and (c) the transverse equivalent stresses as a function of distance for uniform (dashed blue and green lines) and the non-uniform thickness (solid red for the loading condition in (a) and (b) and solid black for another loading condition).

The crack initiation stress in sample R2C6-T-2_7.8 in KOH water chemistry was 0.8YS. Only 3 cracks were found in the uniform strain region and all of them are very small. A representative crack is shown in Figure 5-9. The oxidation at this crack was propagated to the neighbor grain but the crack opening is only several tens of nanometers, indicating the crack initiation was due to the grain boundary oxidation.

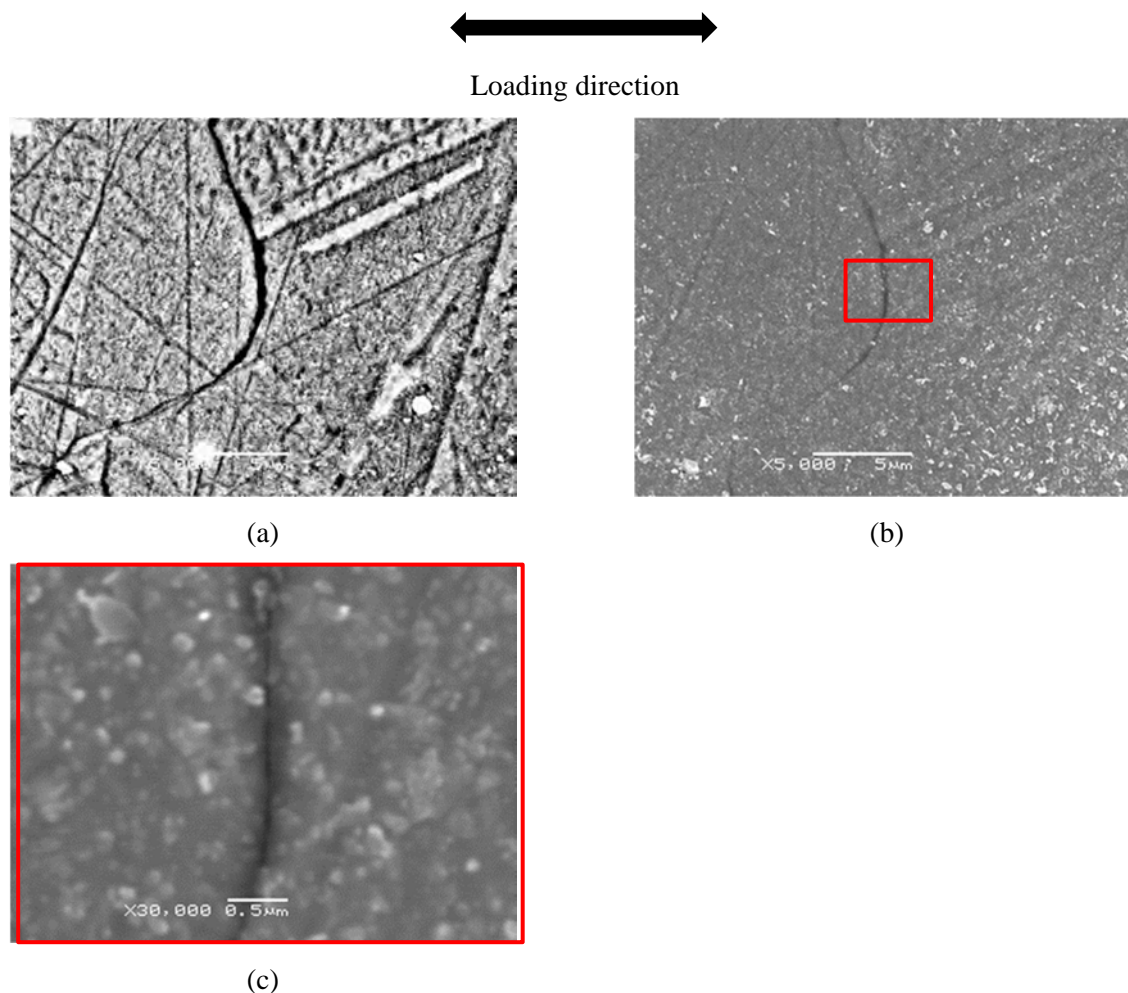


Figure 5-9: A representative crack from sample S-R2C6-T-2 at 0.8 YS. (a) BSE image, (b) SE image of the same region, and (c) a magnified SE image of the crack initiation site.

The crack initiation stress in sample D28-T-2_16.5 in KOH water was 0.7YS. Three cracks were found in the uniform strain region and Figure 5-10 shows one of these cracks.

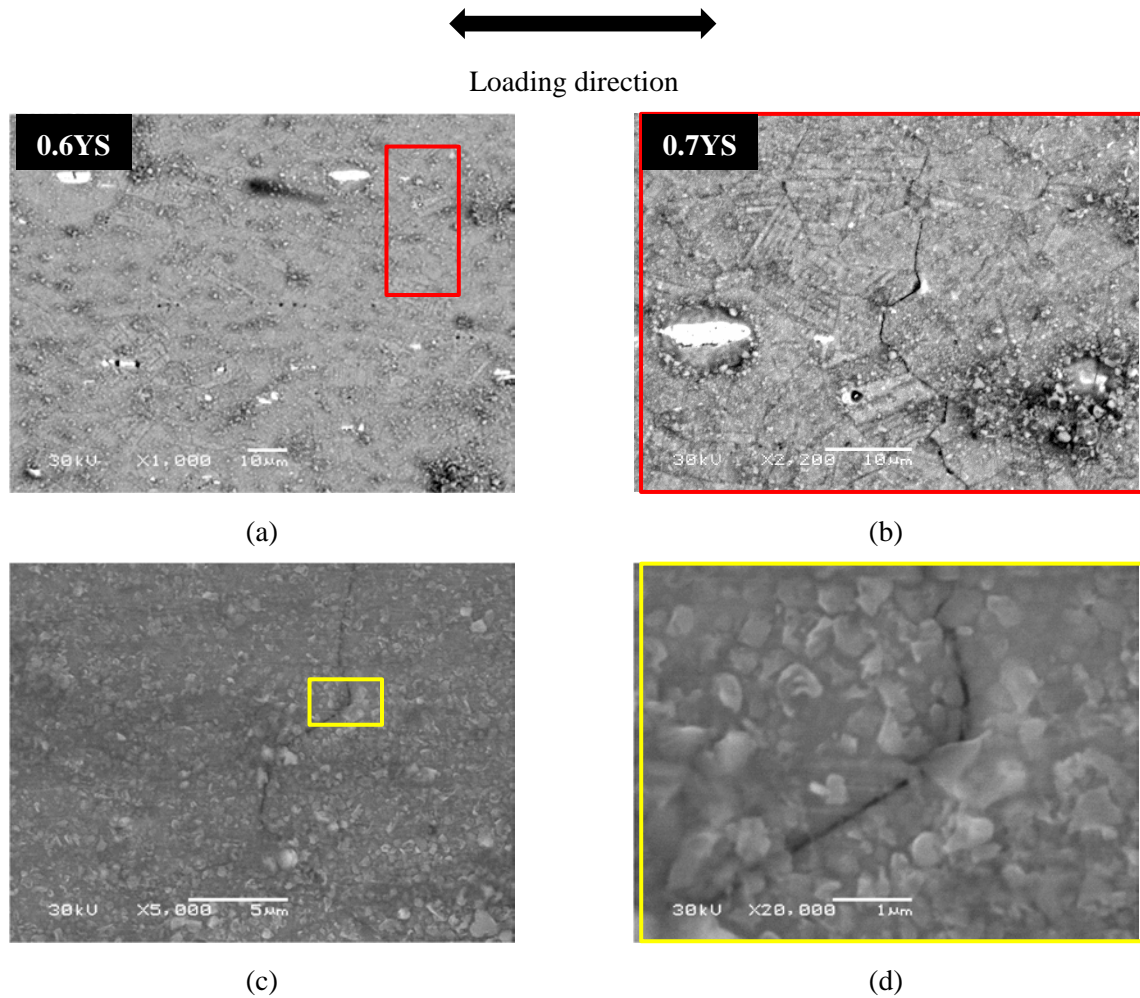


Figure 5-10: A representative crack from sample D28-T-2 at 0.7 YS. (a) BSE image, (b) magnified SE image of the same region, and (c) a magnified SE image of the crack initiation site, (d) a higher-magnification view of the yellow box in (c).

5.2 FOUR-POINT BEND TEST RESULTS OF 347 SS IN LIOH WATER CHEMISTRY

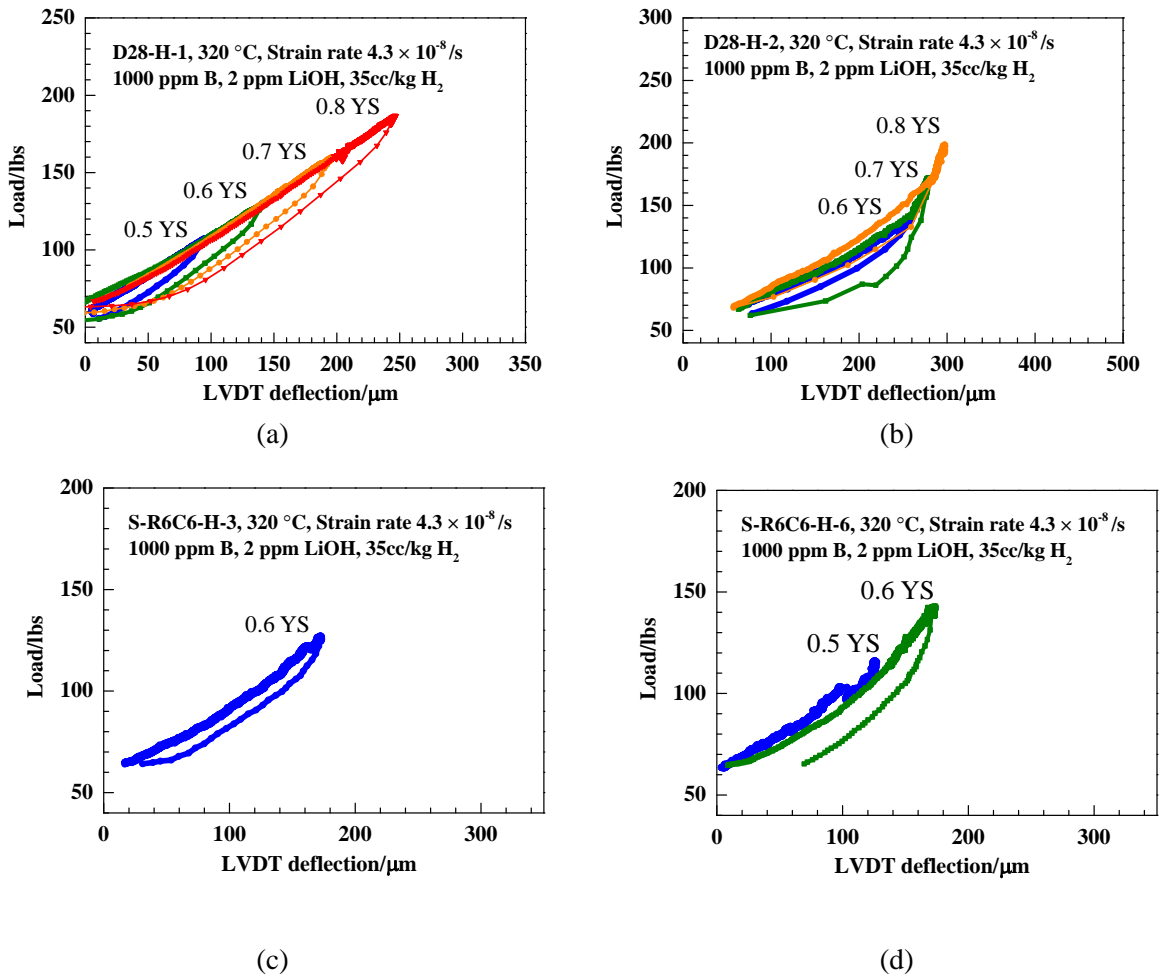
5.2.1 Sample loading history

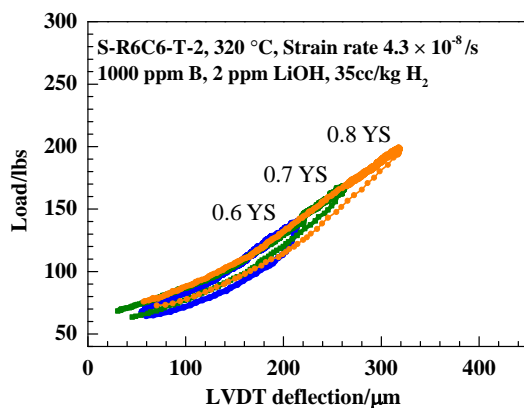
Seven samples were tested in LiOH water chemistry using the same procedure as those tested in KOH. Figure 5-11(a) shows the load versus LVDT displacement of D28-H-1_26.4. This sample was strained first to 0.5YS and no IASCC initiation was observed in the uniform strain region. Further straining to 0.6YS and 0.7YS did not show any IASCC initiation. However, 5 cracks initiated in the uniform region after straining to 0.8YS. Since the crack initiation stress in LiOH water chemistry was obviously higher than that in the KOH water chemistry for the same irradiation damage level, the test was repeated using D28-H-2_26.4 as shown in Figure 5-11(b). The replica was strained up to 0.7YS without any evidence IASCC initiation but the initiation was observed after straining to the 0.8YS which agrees with the results of D28-H-1_26.4 that had been tested first in the LiOH.

Figure 5-11(c) shows the interrupted test results of S-R6C6-H-3_18.4. Since the same damage level in KOH did not show IASCC initiation below 0.8YS, the test on this sample was started at 0.6YS. However, 4 cracks were found in the uniform strain region of this sample after straining to 0.6 YS, which is also lower than the crack initiation stress for D28-H-1_26.4 and D28-H-2_26.4 (in LiOH). To check the reproducibility of the 4PB test results, another interrupted test was repeated in LiOH using the sample S-R6C6-H-6_18.4, as shown in Figure 5-11(d). IASCC initiation was observed at 0.6YS, which is in consistent with sample S-R6C6-H-3_18.4 result.

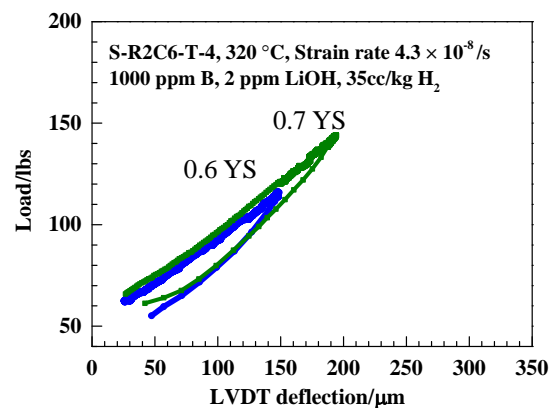
The remaining 4PB interrupted tests followed the same procedure and the IASCC initiation was observed at: 0.8YS in S-R6C6-T-2_11.5 as shown in Figure 5-11(e), 0.7YS in S-R6C6-T-4_7.8 as shown in Figure 5-11(f), and 0.7YS in D28-T-1_16.5 as shown in Figure 5-11(g).

Figure 5-12 shows the morphology of 4PB samples after the interrupted step that led to IASCC initiation. In general, the observed cracks in the uniform strain regions were less than 10 cracks per sample. The distribution of cracks is uniform on all bending samples, indicates the good dimensions of the sample and reliability of the crack initiation stress.

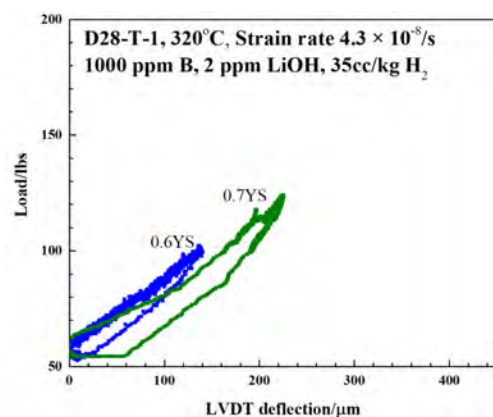




(e)



(f)



(g)

Figure 5-11: Load versus LVDT displacement for the samples tested in the LiOH water chemistry. The IASCC initiation in (a) D28-H-1_26.4 were observed after straining to 0.8YS, (b) D28-H-2_26.4 were observed after straining to 0.8YS (c) S-R6C6-H-3_18.4 were observed after straining to 0.6YS (d) S-R6C6-H-6_18.4 were observed after straining to 0.6YS (e) S-R6C6-T-2_11.5 were observed after straining to 0.8YS (f) S-R2C6-T-4_7.8 were observed after straining to 0.7YS (g) D28-T-1_16.5 were observed after straining to 0.6YS.

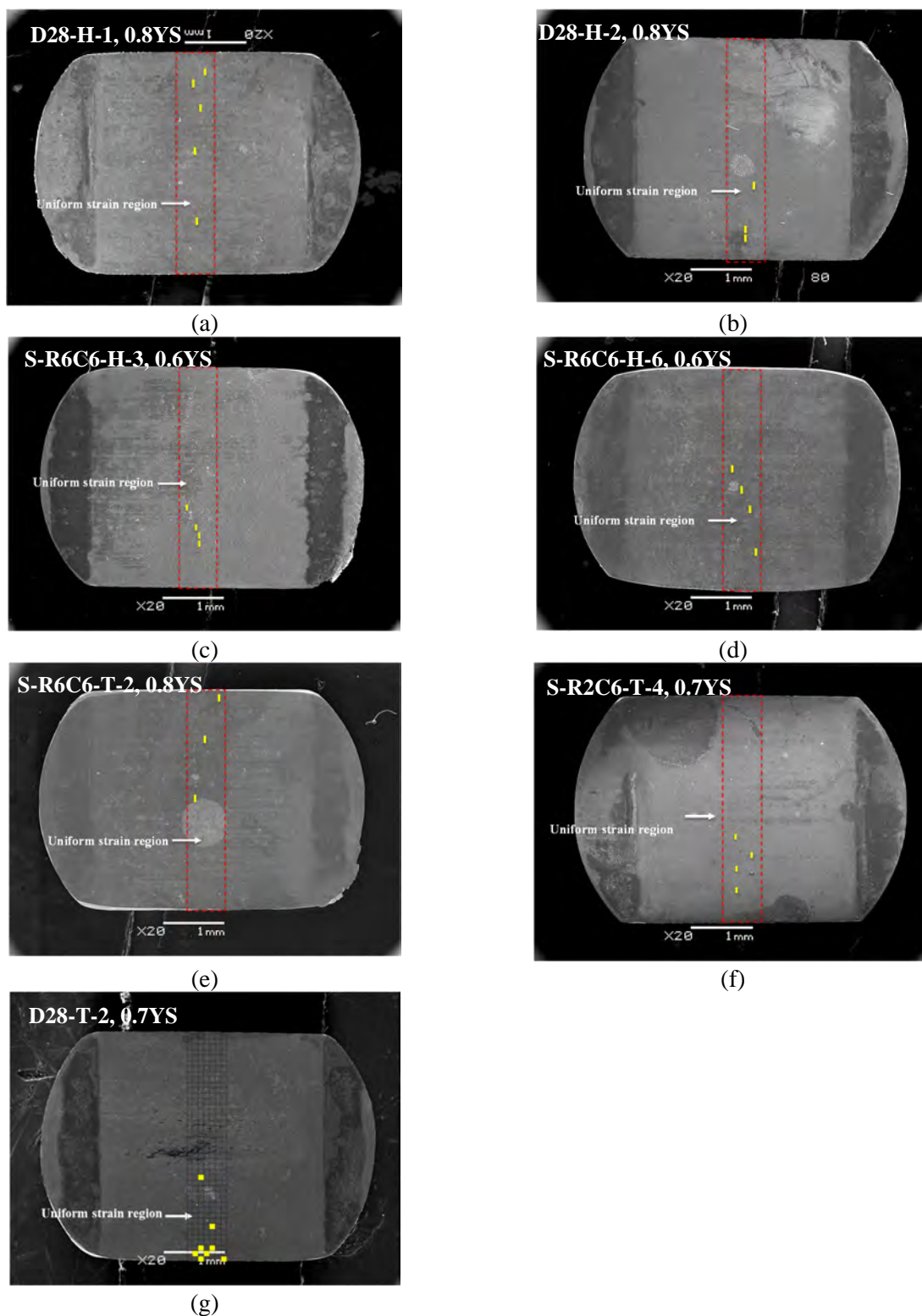


Figure 5-12: Morphologies of four-point bend samples after final bending tests in LiOH water chemistry.

5.2.2 Crack characterization

Table 5-2 summarizes the crack initiation stress, number of cracks, average of crack length, crack density and crack length per unite area of samples D28-H-2, D28-H-1, S-R6C6-H-3, S-R6C6-H-6, S-R6C6-T-2, S-R2C6-T-4 and D28-T-2 in LiOH water chemistry. The table shows that only 5 cracks were observed on sample D28-H-2_26.4 after straining to 0.8YS. The average crack length is 32.3 μm , which is almost equal to that of D28-H-3_26.4 in the KOH water chemistry, so the initiation stress is corrected to be 0.75YS for this sample as the average crack length is larger than the size of grain in this material. Nevertheless, the crack initiation stress of the 26.4 dpa sample in LiOH water chemistry is higher than that in KOH water chemistry. A repeat test on the 26.4 dpa sample was performed on D28-H-2_26.4 and the initiation stress was confirmed at 0.8YS but relatively lower average length of 10.6 μm compared to previous results in LiOH and KOH for the same damage level. Sample S-R6C6-H-3_18.4 cracked at 0.6YS with 4 cracks and an average crack length of 8.75 μm , while the repeat sample S-R6C6-H-6_18.4 showed similar response as it was failed at 0.6YS with 4 cracks and average crack length of 10.25 μm which is comparable with the previous one in the same damage level. For the sample S-R6C6-T_11.5, 3 small cracks were found after straining to 0.8YS with an average crack length of 13.7 μm , while the crack initiation stress in sample R2C6-T-4_7.8 is higher than that of sample S-R6C6-T-2_7.8 by 0.1 YS, while the average crack length and crack density are similar.

Table 5-2: Statistics of cracks in samples D28-H-2, D28-H-1, S-R6C6-H-3, S-R6C6-H-6, S-R6C6-T-2 and S-R2C6-T-4 after crack initiation in LiOH.

Sample ID	D28-H-2	D28-H-1	S-R6C6-H-3	S-R6C6-H-6	D28-T-2	S-R6C6-T-2	S-R2C6-T-4
Thickness (mm)	0.82	0.81	0.785	0.804	0.815	0.835	0.785
dpa	26.4	26.4	18.4	18.4	16.5	11.5	7.8
Yield stress (MPa)	1089	1089	1082	1082	1077	1050	996
Crack initiation Stress	0.8	0.8	0.6	0.6	0.7	0.8	0.7
Applied stress (% YS)	0.8	0.8	0.6	0.6	0.7	0.8	0.7
Number of cracks	3	5	4	4	3	3	4
Average crack length (μm)	10.6 \pm 0.28	32.3 \pm 0.88	8.75 \pm 0.50	10.25 \pm 0.57	9	13.7 \pm 0.42	11.3 \pm 0.48
Crack density (#cracks/mm ²)	1.7	2.9	2.3	2.3	1.74	1.7	2.3
Crack length/unit area ($\mu\text{m}/\text{mm}^2$)	18.02 \pm 2.5	93.7 \pm 5.4	20.1 \pm 2.2	23.6 \pm 2.8		23.3 \pm 3.5	26 \pm 3.1

Figure 5-13 shows a representative crack initiated at 0.8YS on D28-H-2_26.4. Similar to the surface morphology in KOH water chemistry, the surface was covered by dense oxide particles, making it was hard

to identify the microstructural features associated with crack initiation such as DCs. The penetration of oxidation into the neighboring grains is clear as shown in Figure 5-13(b) and (d) which could be an evidence of oxidation role in the IASCC initiation. It can be seen that ~~the~~ even though the oxidized GBs looks thick in the BSE image (Figure 3.13 (b)) only the cracks were observed in the SEI image (Figure 3.13 (d)) which might indicate that the oxide formed first (whether in this straining level or the previous one) then it had been cracked due to the loading.

The morphology of the crack shown in Figure 5-14 on D28-H-1_26.4 was similar to that on D28-H-2.

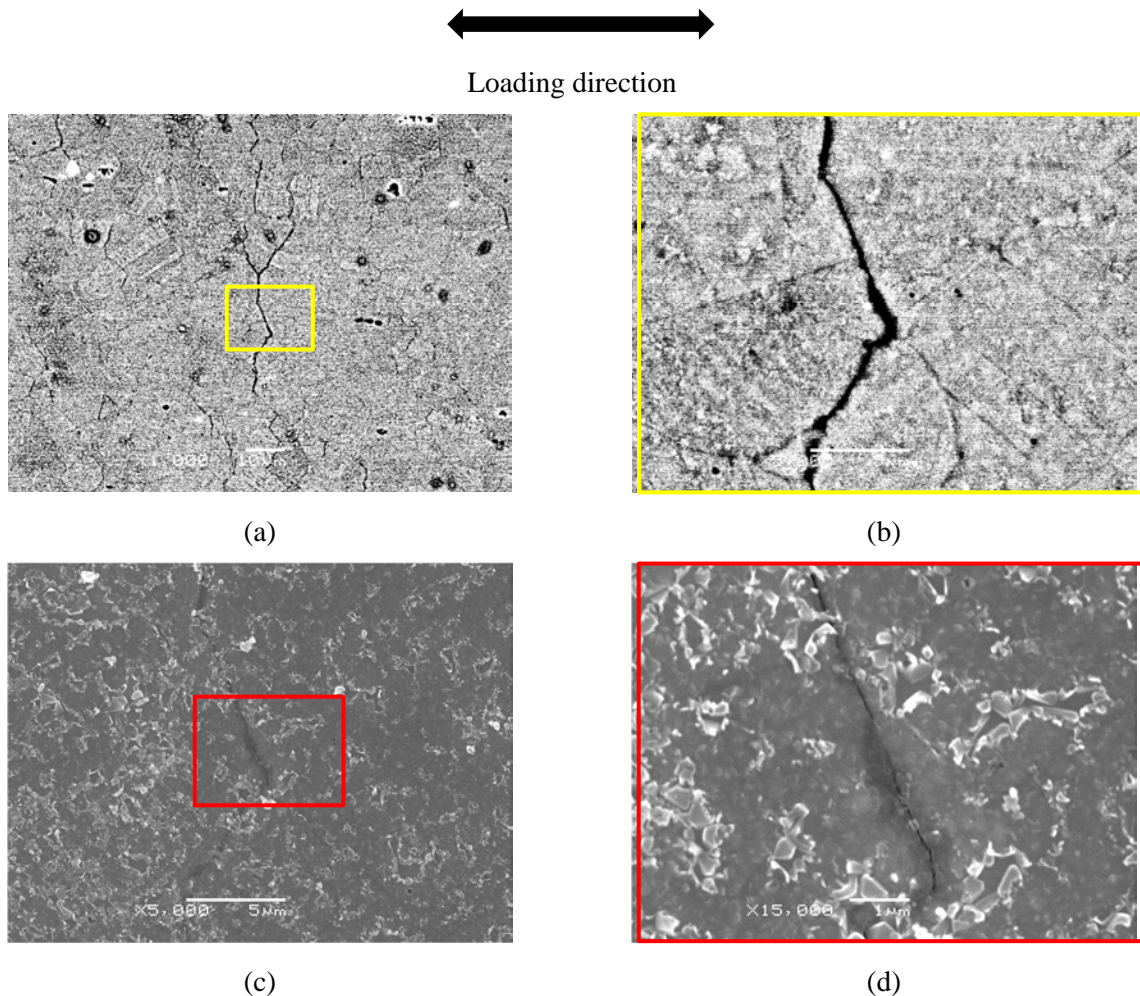


Figure 5-13: A representative crack from sample D28-H-2 at 0.8 YS in LiOH. (a) BSE image, (b) magnified BSE image, (c) SE image of the same region, and (d) magnified SE image of the crack initiation site.

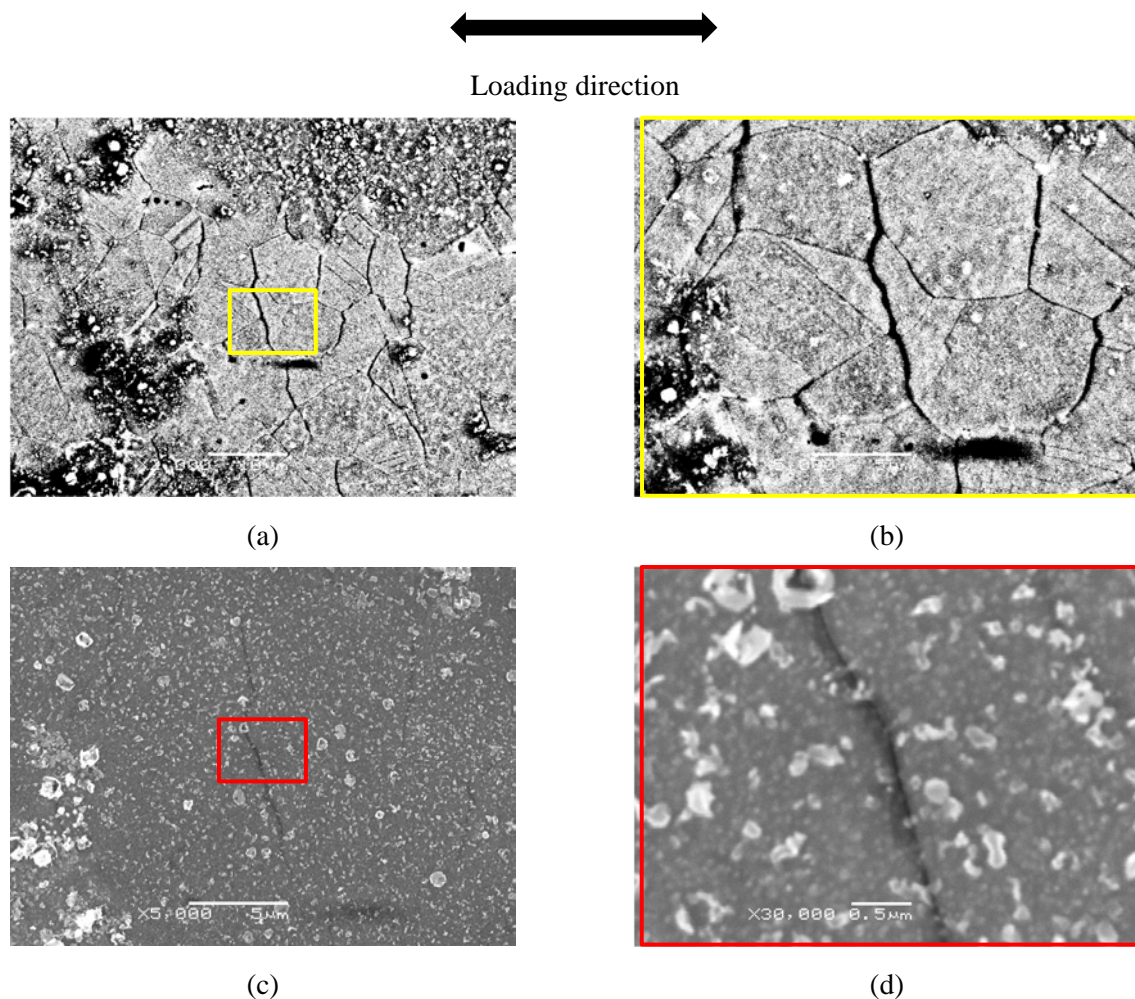


Figure 5-14: A representative crack from sample D28-H-1 at 0.8 YS in LiOH. (a) BSE image, (b) magnified BSE image, (c) SE image of the same region, and (d) magnified SE image of the crack initiation site.

A representative crack initiated in sample S-R6C6-H-3_18.4 at 0.6YS is shown in Figure 5-15. The crack is shallow with width less than 100 nm. Similar crack features were found in sample S-R6C6-H-6_18.4 and shown in Figure 5-16.

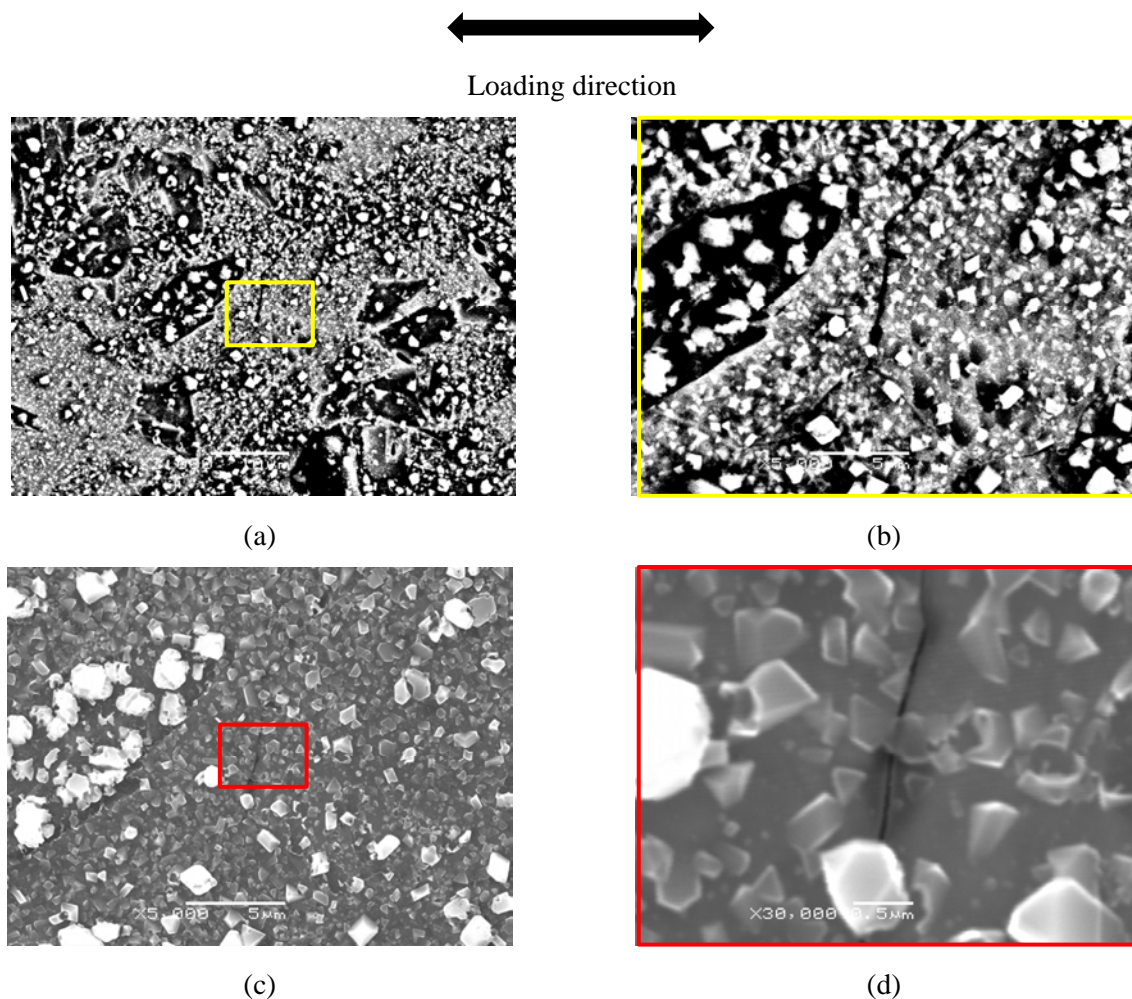


Figure 5-15: A representative crack from sample S-R6C6-H-3 at 0.6 YS in LiOH. (a) BSE image, (b) magnified BSE image, (c) SE image of the same region, and (d) magnified SE image of the crack initiation site.

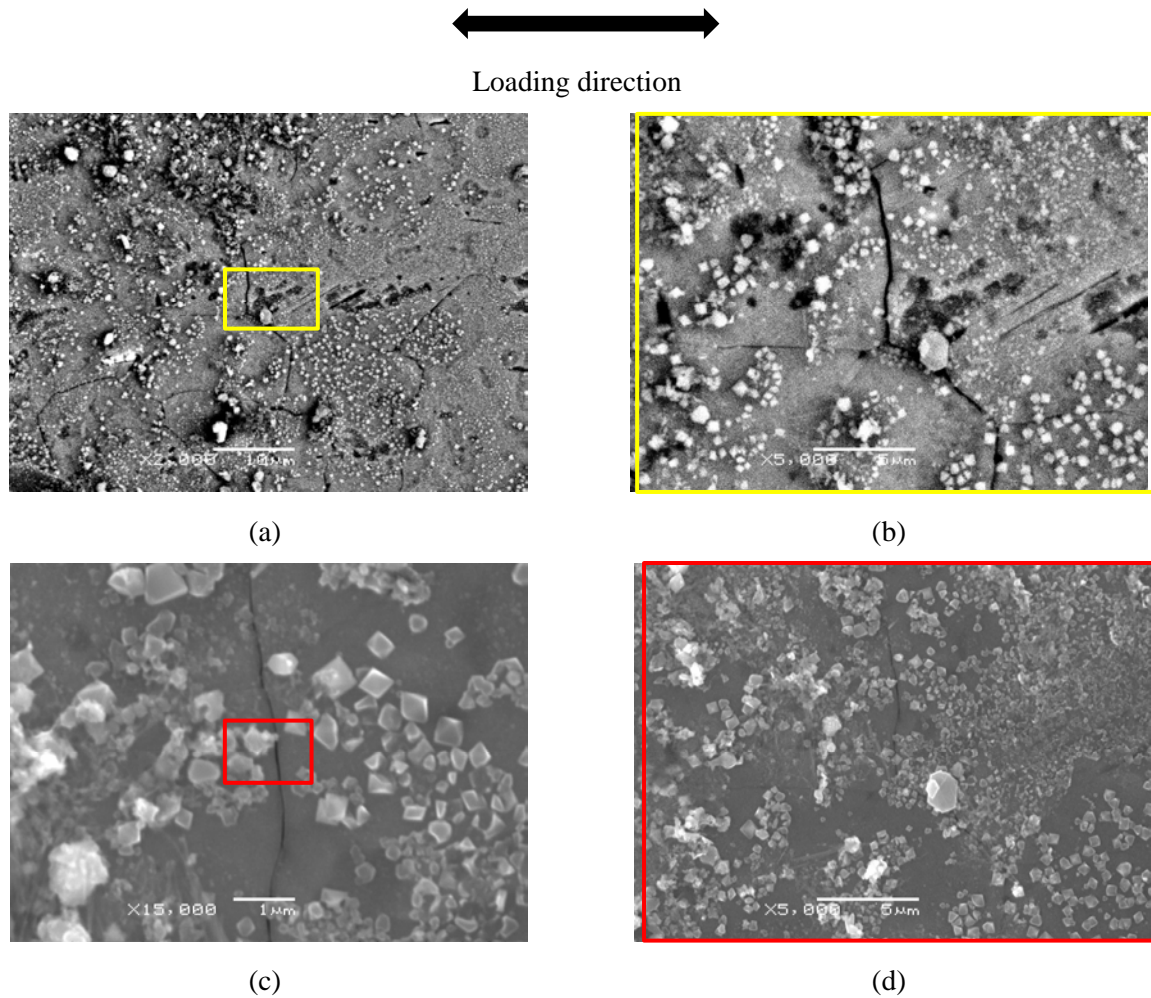


Figure 5-16: A representative crack from sample S-R6C6-H-6 at 0.6 YS in LiOH. (a) BSE image, (b) magnified BSE image, (c) SE image of the same region, and (d) magnified SE image of the crack initiation site.

For the sample S-R6C6-T-2_11.5, the largest crack generated from the edge at 0.8YS has a length of about 25 μm (Figure 5-17). The morphology of this crack is similar to the cracks on the samples with higher damage levels. In addition, deformation bands due to hot forging and the edge effect can be clearly observed by the BSE image. However, these bands did not show any role in the IASCC initiation regardless their density at the surface where it's the maximum. These bands might have increased the stress at certain points on the GBs but due to their high density the stress will likely be distributed along the GB which will reduce the local stress concentration.

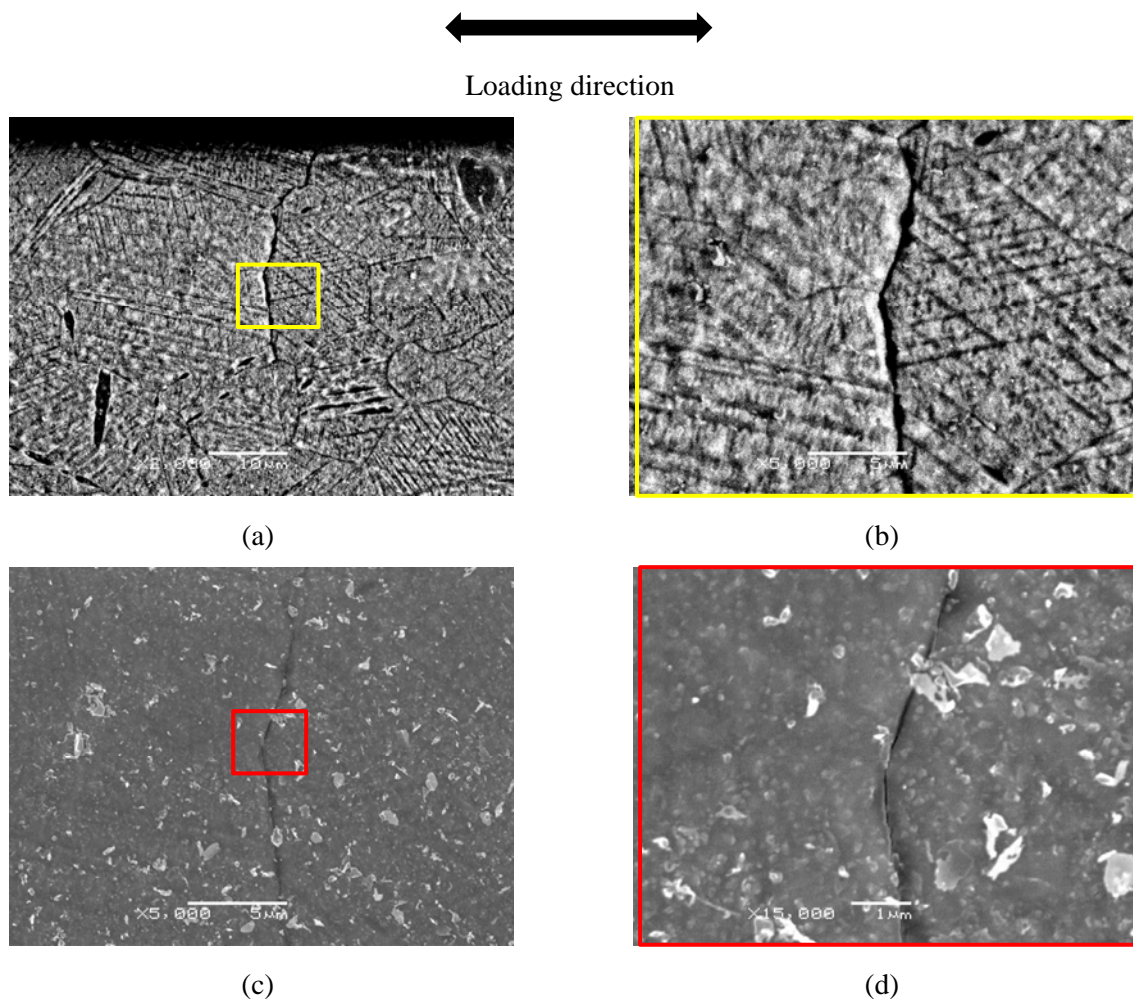


Figure 5-17: A representative crack from sample S-R6C6-T-2 at 0.8 YS in LiOH. (a) BSE image, (b) magnified BSE image, (c) SE image of the same region, and (d) magnified SE image of the crack initiation site.

A representative crack initiated in sample S-R2C6-T-4_7.8 at 0.7 YS is shown in Figure 5-18. No penetration of oxidation into the neighboring grain was found on all of four cracks in the uniform region.

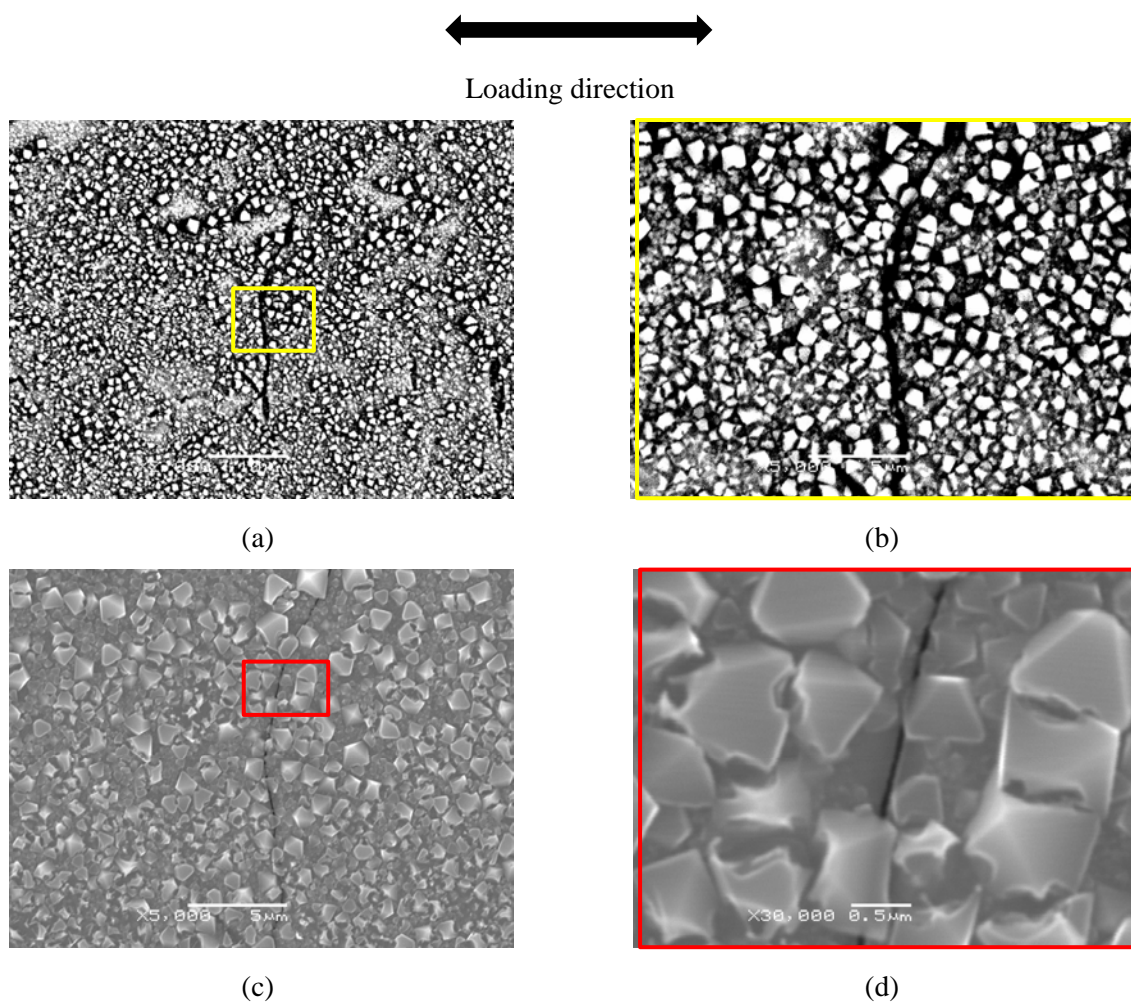


Figure 5-18: A representative crack from sample S-R2C6-T-4 at 0.7 YS in LiOH. (a) BSE image, (b) magnified BSE image, (c) SE image of the same region, and (d) magnified SE image of the crack initiation site.

The last sample which was tested in this condition was the D28-T-1_16.5 and a representative crack is shown in Figure 5-19. This sample has failed at 0.7YS and part of GB is still oxidized but not cracked while the other is cracked which could indicate that the oxidation of GB usually takes place first and then the areas with high localized stress cracks.

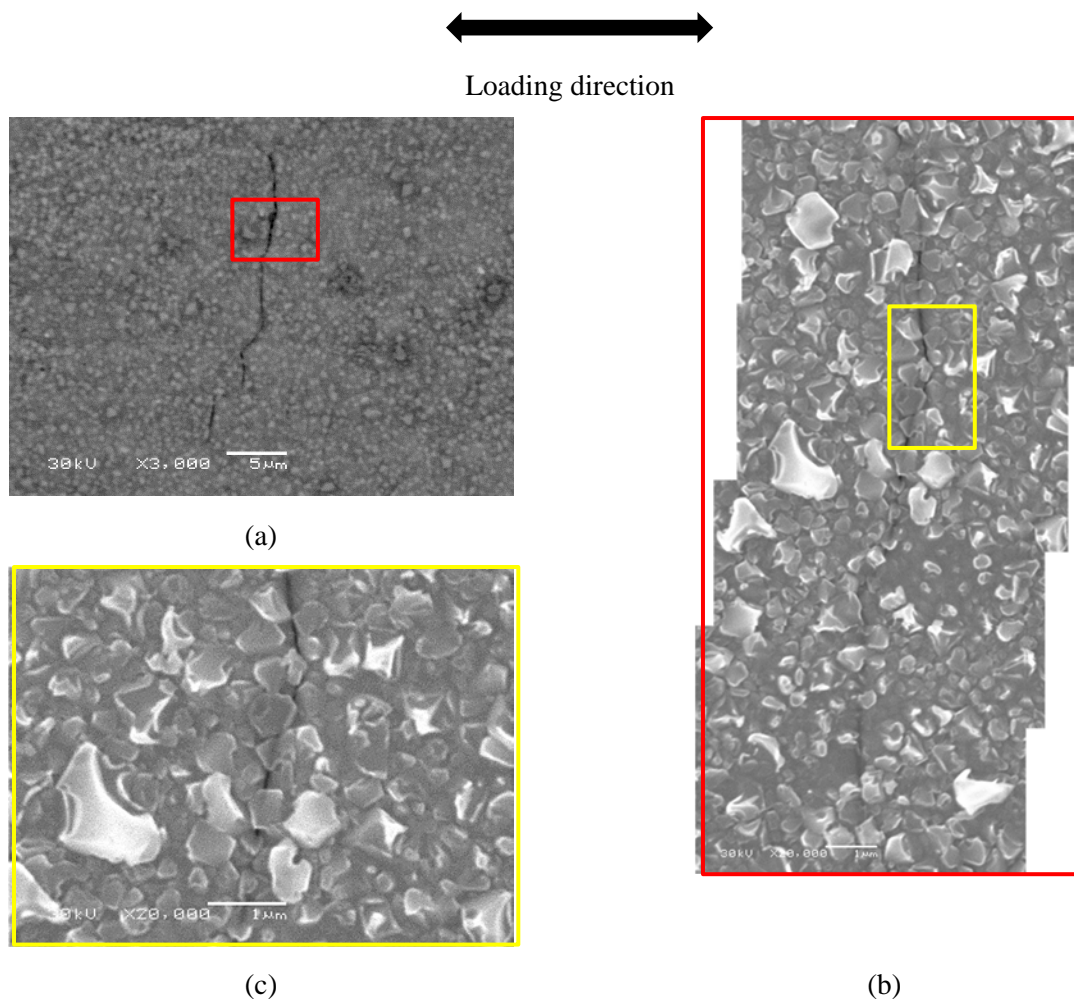


Figure 5-19: A representative crack from sample D28-T-1 at 0.8 YS in LiOH. (a) BSE image, (b) SE image of the same region, and (c) a magnified SE image of the crack initiation site.

Specimen S-R2C6-T2 underwent the oxide removal process described in subsection 4.3. The sample surface after the oxide removal is shown in Figure 5-20. While a slightly greater extent of cracking was observed after oxide removal, the difference was rather small.

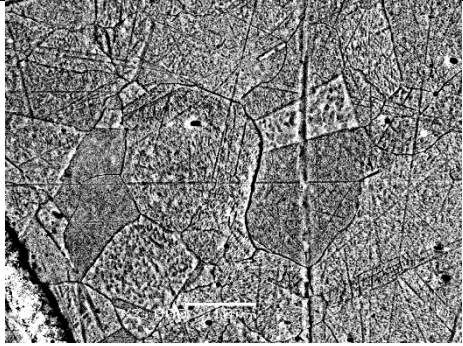
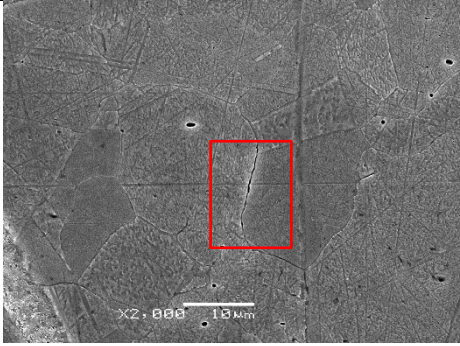
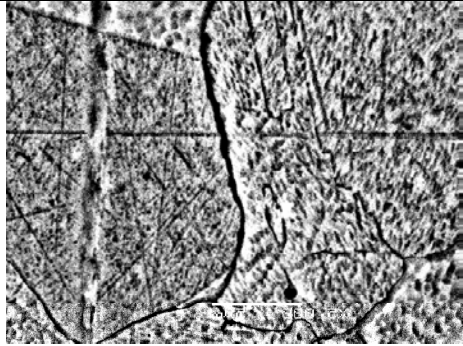
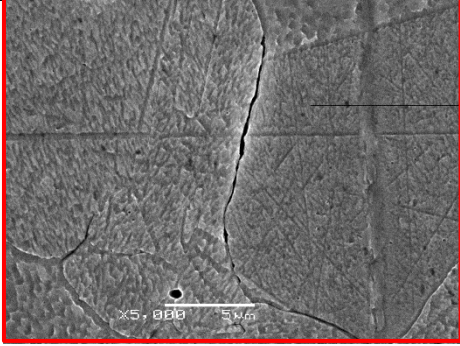
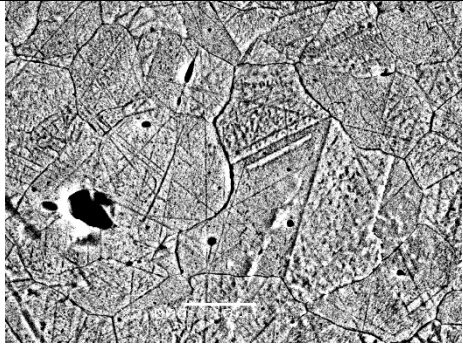
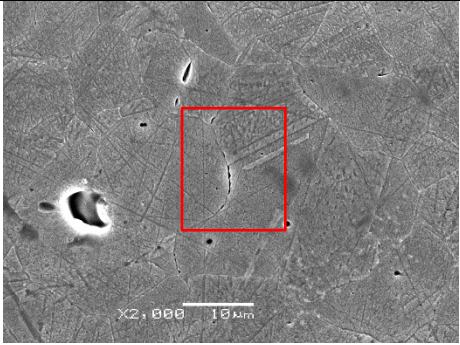

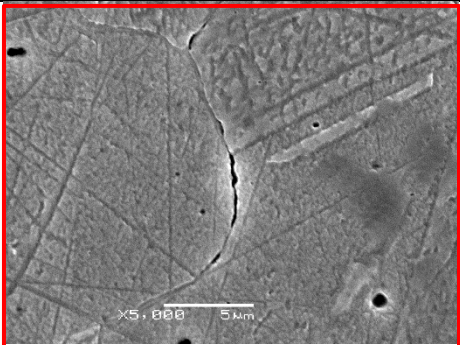
Position	BSE	SEM
1-3		
		
1-7		
		

Figure 5-20: BSE (left) and SEM (right) images of specimen S-R2C6-T2 after oxide removal.

5.3 THE INCLINATION ANGLES OF THE CRACKED GBS.

The grain boundaries with orientation perpendicular to the loading direction are the preferable crack initiation sites. The inclination angle of 19 and 23 cracks that initiated in KOH and LiOH water chemistry was measured. The result of statistical analysis showed that the majority of the cracks have a trace inclination greater than 70° (Figure 5-21 (a)), which is consistent with the reported results in literature (References 19, 21) and agreed with the fact that GBs with perpendicular inclination to the applied stress have a higher susceptibility to IASCC.

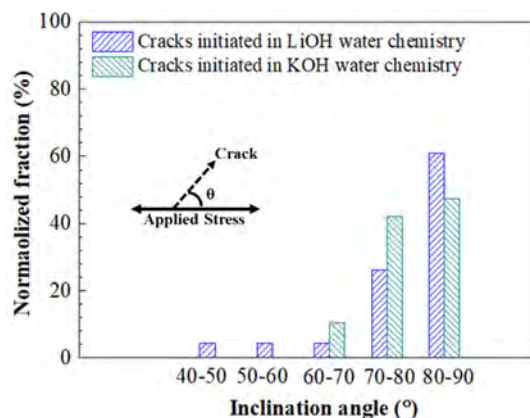


Figure 5-21: The comparison of trace inclination angle of cracks for testes in PWR KOH and PWR LiOH water chemistries.

5.4 OXIDATION BEHAVIOR ON SURFACE AND AT GRAIN BOUNDARIES

Figure 5-22 shows the surface morphology and EDX analyses of oxides on sample S-R6C6-T-3 in the KOH water chemistry. The surface of the sample has a dense oxide layer which mainly contains two forms. The first one which is distributed sporadically with low density at the surface have an irregular shape and containing higher Ni content, while the other has a polyhedral shape and containing lower Ni content and depleted in Cr. In addition, the composition of the inner layer is dominated by Fe and Cr (Figure 5-22 (c)).

Figure 5-23 shows the surface morphology and EDX analyses of oxides on sample D-28-H-2 in LiOH water chemistry. Similar oxides morphologies to sample S-R6C6-T-3 were also observed in D28-H-2_26.4. The inner layer of the film also shows enrichment of Fe and Cr (Figure 5-23 (c)).

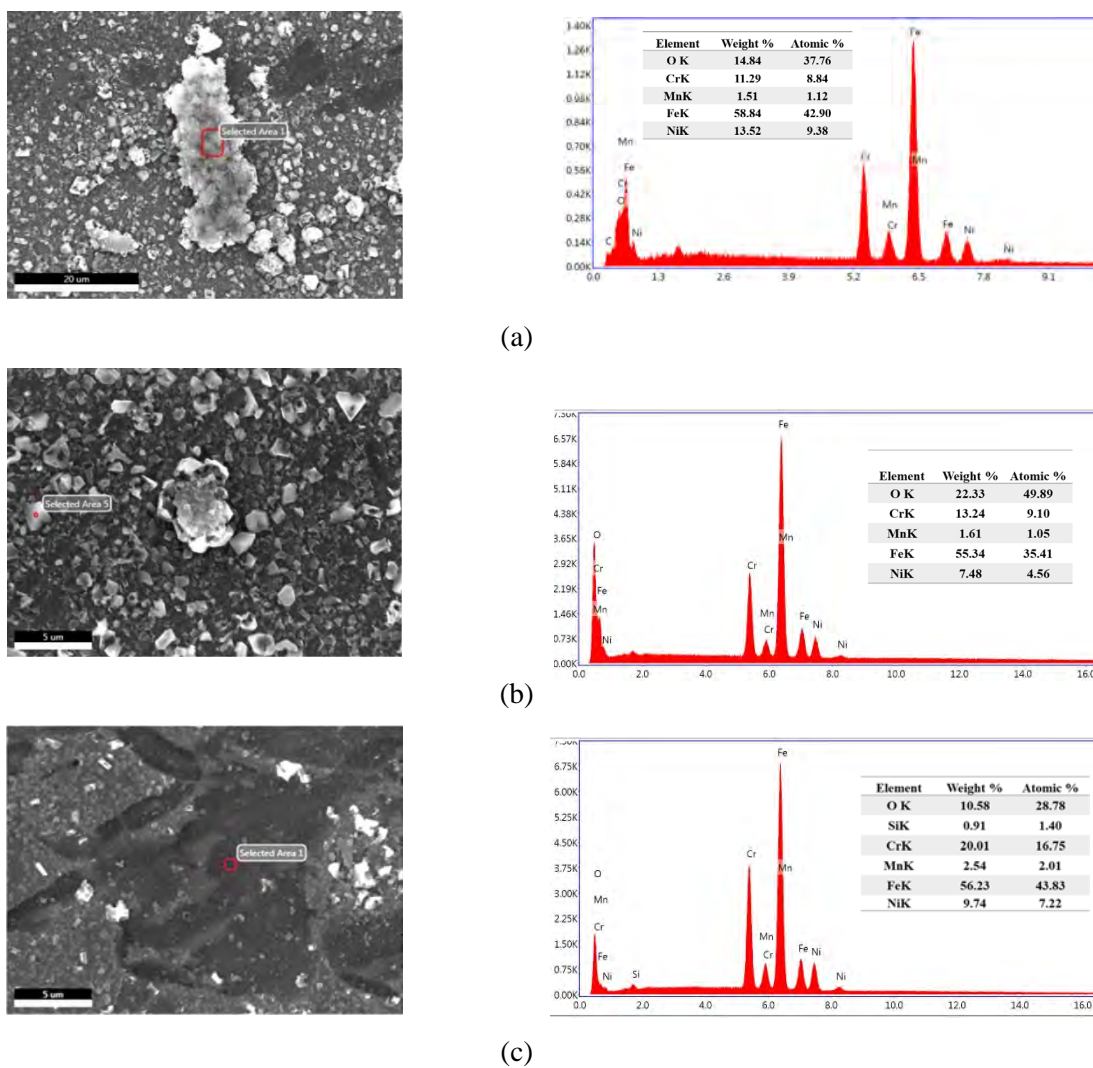


Figure 5-22: The surface morphology and EDX analyses of the surface oxides of the sample S-R6C6-T-3 in KOH water chemistry.

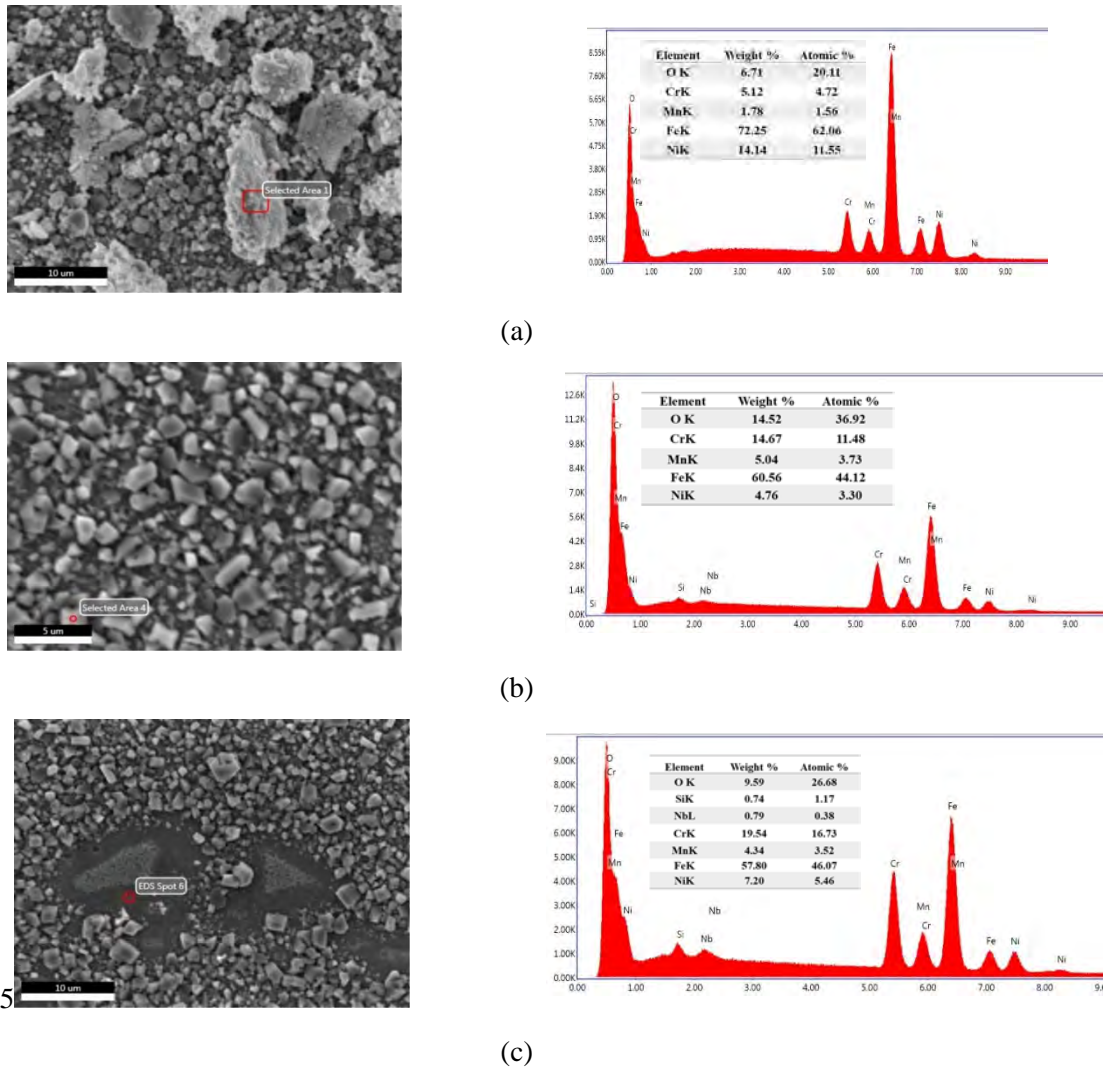


Figure 5-23: The surface morphology and EDX analyses of the surface oxides of the sample D-28-H-2 in LiOH water chemistry.

The surface oxide film thickness was measured using TEM HAADF as shown in Figure 5-24 (a) for LiOH for the sample D28-H-1_26.5 and (b) for KOH for the sample D28-H-3_26.5. The thickness in couples hundreds of nanometers in both cases. One of the reasons for a thick surface film is the high oxidation rate of this material. For instance, the sample D28-H-1_26.5 was exposed to 243 hours in total in the autoclave and resulted in an average surface inner oxide thickness of 207.6 nm (or 0.85 nm/h). While in case of D28-H-3_26.5, the total exposure was 245 hours with an average surface inner oxide thickness of 199.1 nm (or 0.81 nm/h). Table 5-3 summarizes the surface oxide film of the selected samples and conditions.

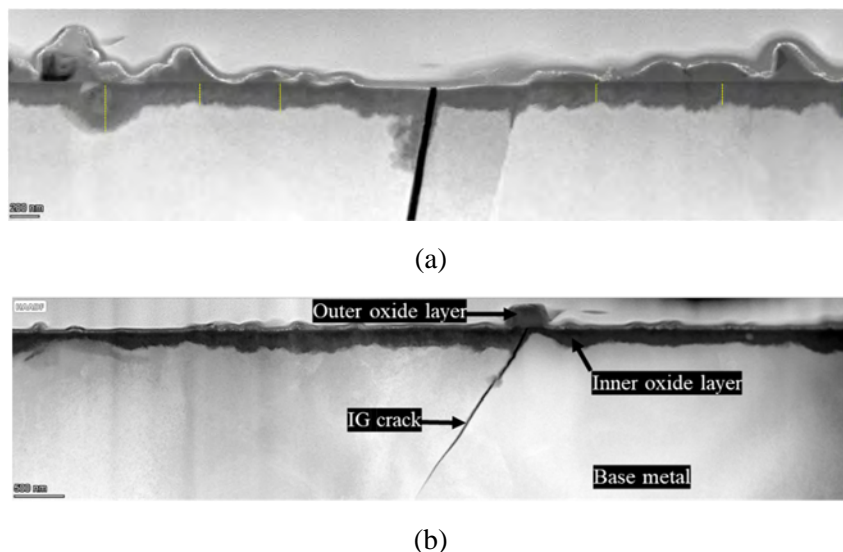


Figure 5-24: TEM-HAADF analysis for the inner layer surface oxide film thickness measurement of (a) D28-H-1_26.5 in LiOH and (b) D28-H-3_26.5 in KOH. The dashed yellow lines indicating the locations of measurements.

Table 5-3: The summary of the surface oxide film of the selected samples and conditions.

	S-R2C6-T-1_7.8	S-R2C6-T-4	D28-H-3_26.4	D28-H-1
Environment	KOH	LiOH	KOH	LiOH
Averaged inner oxide film thickness (nm)	182.6	187.9	199.1	207.6
Compactness	Isolated spinel (NiFe) ₃ O ₄ /continuous Cr ₂ O ₃ /continuous NiO _x	Isolated spinel (NiFe) ₃ O ₄ /continuous Cr ₂ O ₃ /continuous NiO _x	Isolated spinel (NiFe) ₃ O ₄ /continuous Cr ₂ O ₃ /continuous NiO _x	Isolated spinel (NiFe) ₃ O ₄ /continuous Cr ₂ O ₃ /continuous NiO _x
Oxide Structure	spinel (NiFe) ₃ O ₄ /Cr ₂ O ₃ /NiO _x	spinel (NiFe) ₃ O ₄ /Cr ₂ O ₃ /NiO _x	spinel (NiFe) ₃ O ₄ /Cr ₂ O ₃ /NiO _x	spinel (NiFe) ₃ O ₄ /Cr ₂ O ₃ /NiO _x

In general, no difference was noted between the oxidized surfaces in LiOH and KOH as both have the same corrosion products density, particle sizes, shape, and thickness which means that the surface corrosion process is still the same in both water chemistries as expected due to the similar water parameters in both water chemistry conditions.

5.5 MICROSTRUCTURE AND MICROCHEMISTRY OF NEUTRON IRRADIATED SAMPLES

5.5.1 Dislocation loops

TEM rdDF images of dislocation loops in the 8 dpa, 18 dpa and 26 dpa irradiated samples are shown in Figure 5-25(a), (b) and (c), respectively. These rdDF images show only half of all the loops in each sample. The average loop size is 9.78 nm for the 8 dpa sample and 9.03 nm for the 18 dpa sample and 9.45 nm for the 26 dpa sample, respectively. The measured number density is $1.05 \times 10^{22}/\text{m}^3$, $2.33 \times 10^{22}/\text{m}^3$, $2.14 \times 10^{22}/\text{m}^3$, respectively.

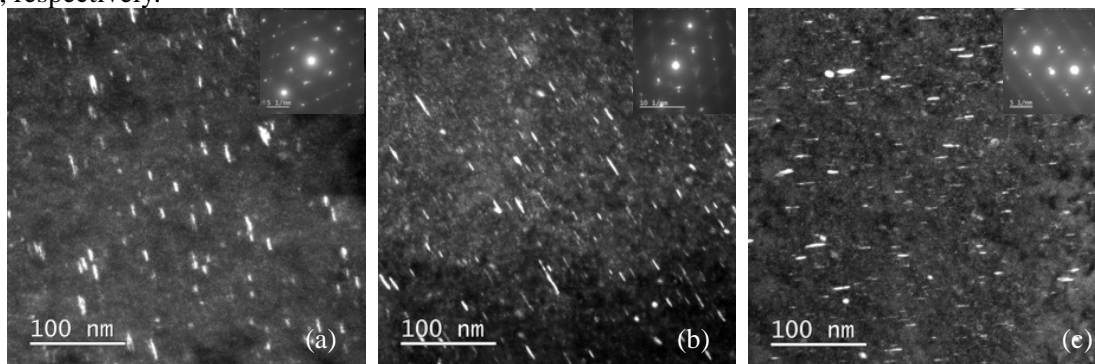


Figure 5-25: (a), (b) and (c) are rdDF images taken from the 8 dpa, 18 dpa and 26 dpa irradiated samples, respectively, using the $\frac{1}{2}\{311\}$ diffraction showing dislocation loops in the materials. The insets are SAED patterns showing the $\{311\}$ 2B condition for the rdDF imaging.

5.5.2 Precipitates

The precipitates in the neutron irradiated 347 samples were found to be mainly a Ni-Si rich phase depleted in Fe and Cr, i.e., $\gamma' - \text{Ni}_3\text{Si}$. The sizes and distributions, of those precipitates were measured from Ni-maps collected by STEM-SI EDS as shown in Figure 5-26. The measured size of the precipitates is, 4.52 nm, 7.03 nm, and 7.15 nm, and the density is $2.23 \times 10^{22}/\text{m}^3$, $2.78 \times 10^{22}/\text{m}^3$ and $2.53 \times 10^{22}/\text{m}^3$ for the 8 dpa, 18 dpa and 26 dpa samples, respectively.

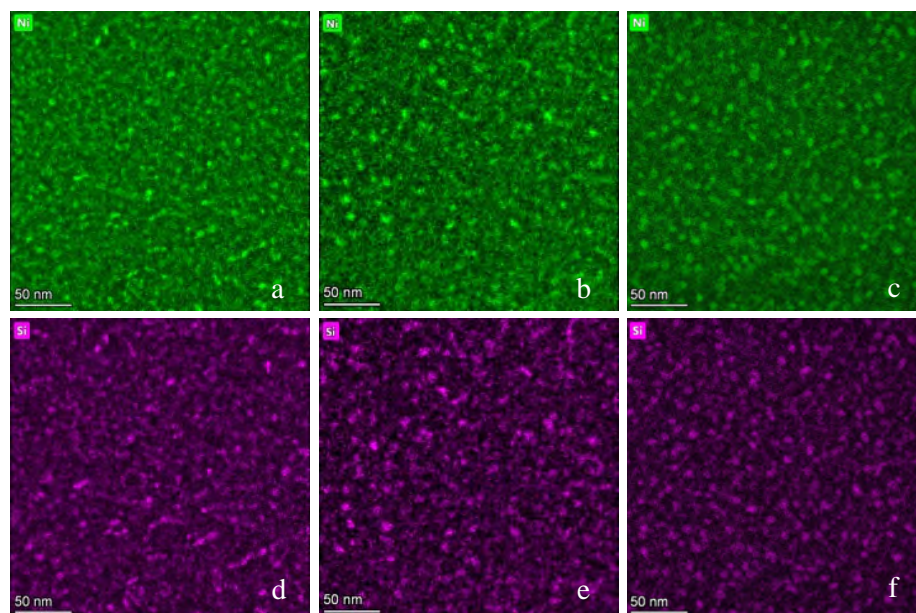


Figure 5-26: Ni-maps (a-c) and Si-maps (d-f) collected from the 347-alloy materials irradiated by neutron at dose levels of a-d: 8 dpa, b-e: 18 dpa and c-f: 26 dpa, respectively.

Very interestingly, S, P, Nb and Mn start to segregate to the Ni-Si rich precipitates with the increase of the damage level as shown in Figure 5-27.

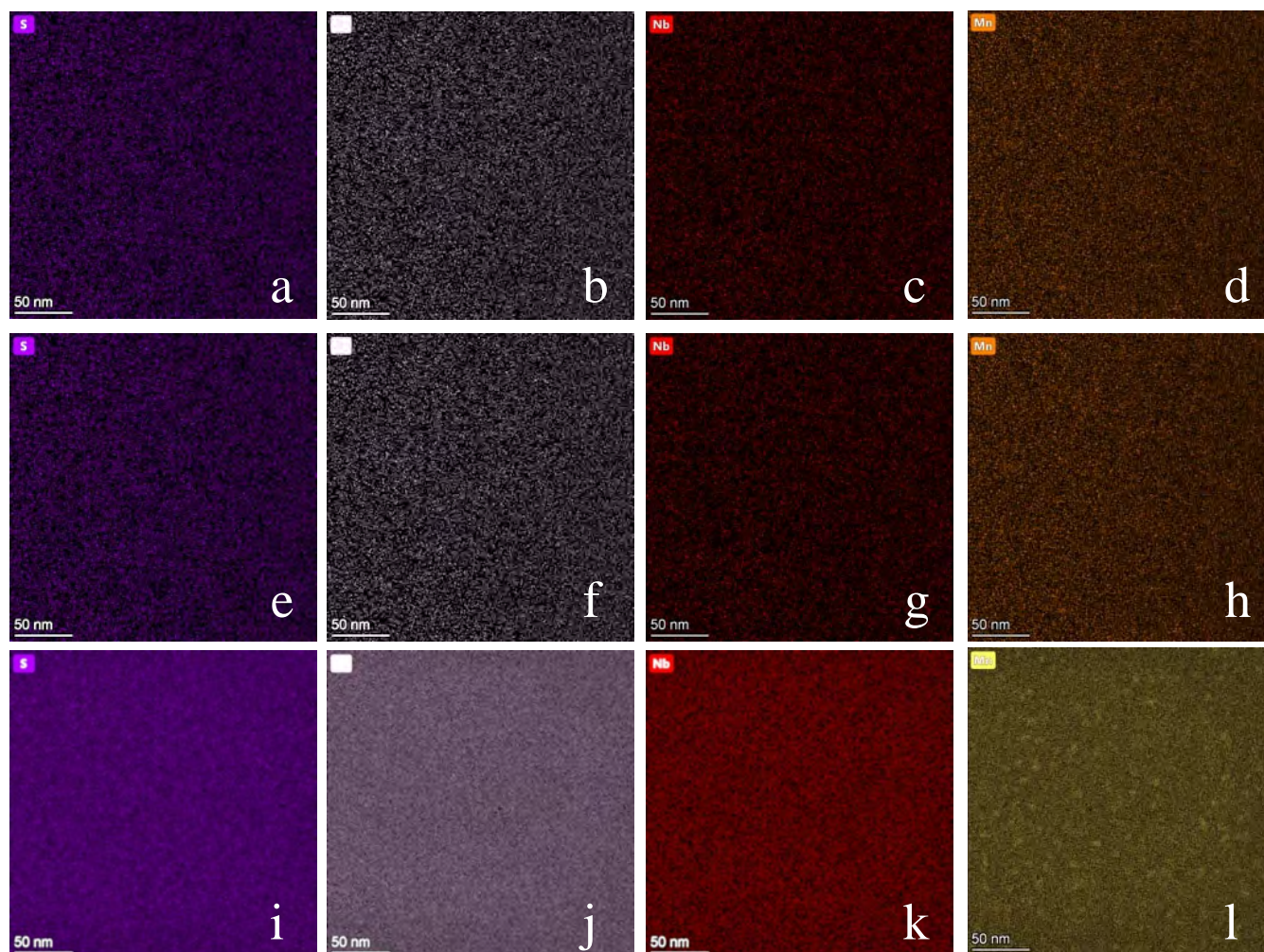


Figure 5-27: S-, P-, Nb-, and Mn-maps collected from the 347-alloy material irradiated to neutron at dose levels of a-d: 8 dpa, e-h: 18 dpa and i-l: 26 dpa, respectively.

Some large precipitates were seen in the 26 dpa damaged sample with some still being crystalline as shown in Figure 5-28. It is a carbon-nitride phases containing almost all the elements in the alloy with some dislocation loops in the precipitate (Figure 5-28a). The measured composition of the precipitate is (at%): Nb: 45.9, N: 14.3, C: 14.0, S: 6.68, Fe: 6.17, Ni: 3.36, P: 3.11, Cr: 2.58, Si: 2.50, and Mn: 1.44. However, another large precipitate was seen to have been fully amorphized (Figure 5-29). It is also a carbon-nitride precipitate with a measured composition of (at%): Nb: 25.6, N: 10.8, C: 6.14, S: 6.70, Fe: 22.7, Ni: 6.74, P: 2.97, Cr: 8.11, Si: 8.57, and Mn: 1.69. This precipitate has more Fe and Cr compared to the one that is still crystalline.

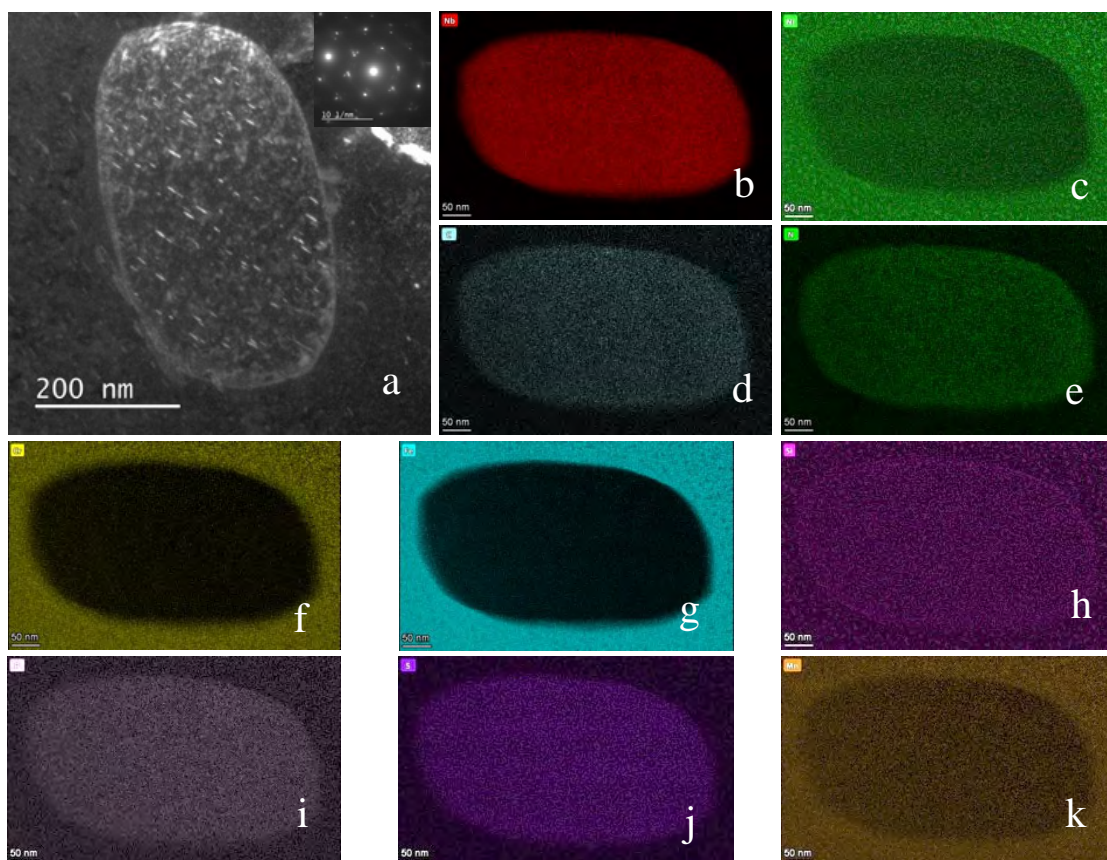


Figure 5-28: (a) rdDF image of a large precipitate in the 26 dpa irradiated sample, (b)-(k) are Nb-, Ni-, C-, N-, Cr-, Fe-, Si-, P-, S- and Mn-maps collected from the precipitate, respectively.

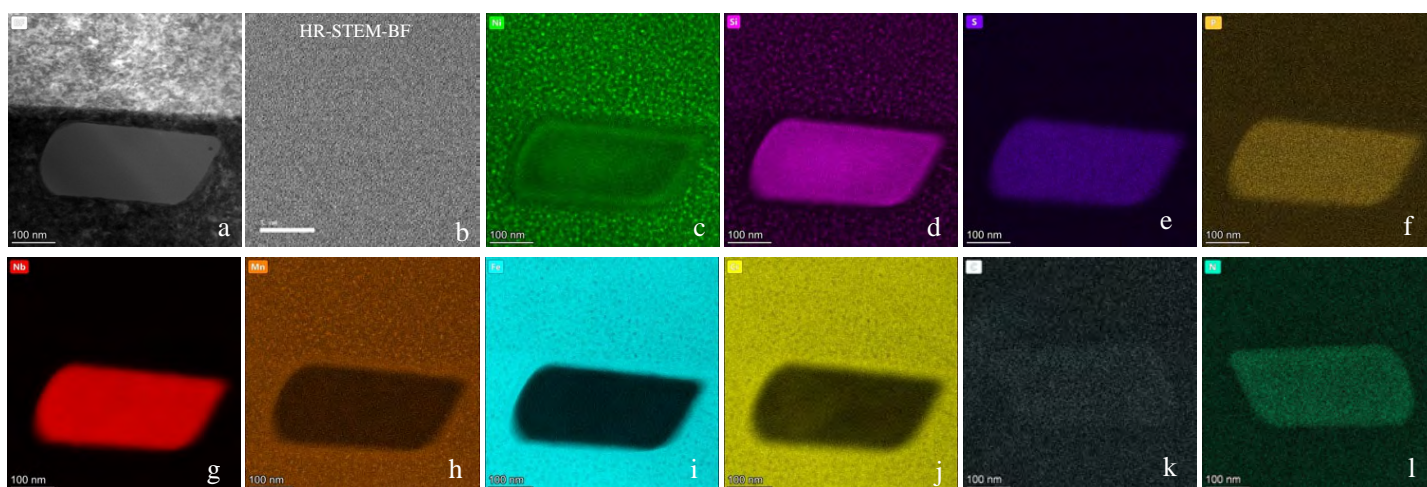


Figure 5-29: (a)-(b) STEM-BF images of a large precipitate in the 26 dpa irradiated sample, (c)-(l) are Ni-, Si-, S-, P-, Nb-, Mn-, Fe-, Cr-, C- and N-maps collected from the precipitate, respectively.

5.5.3 Radiation induced segregation (RIS)

Figure 5-30 displays STEM-SI EDS data showing the distributions of Cr, Fe, Ni, Si, S, P, Nb, N and Mn at a high-angle grain boundary (HAGB) in the 347SS 8 dpa sample. In Figure 5-31a, an orange arrow (the frame highlights the width of the line) across the GB was drawn along which element profiles across the GB were extracted as shown in Figure 5-31b and Figure 5-31c. It clearly shows that the HAGB enriches in Ni, Si, P and a little bit S and Nb and depletes in Fe, Cr and Mn.

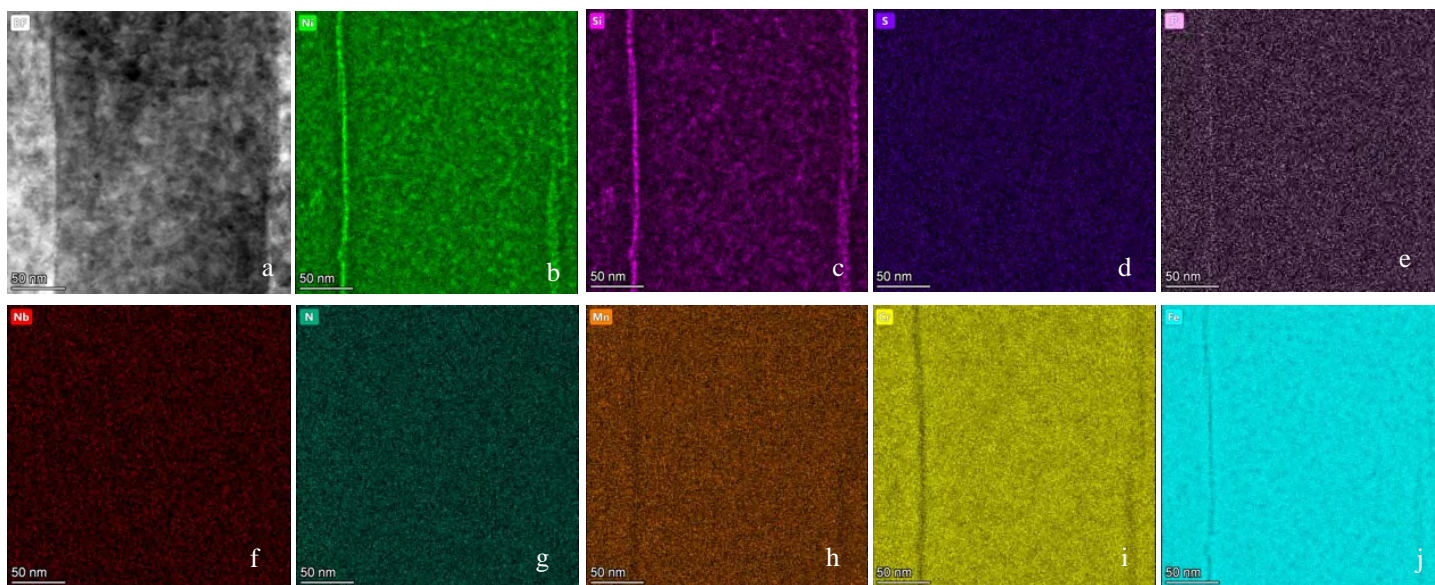


Figure 5-30: (a) STEM-BF image of a HAGB in the 8 dpa irradiated sample, (b)-(j) are Ni-, Si-, S-, P-, Nb-, N-, Mn-, Cr-, and Fe-maps, respectively.

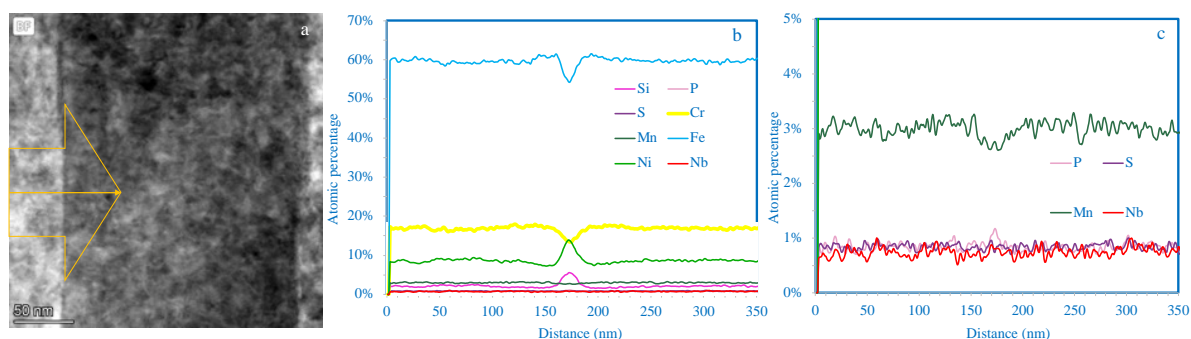


Figure 5-31: (a) STEM-BF image of a HAGB in the 8 dpa irradiated sample with an arrow drawn for element profiles; (b) displays Ni-, Si-, S-, P-, Nb-, N-, Mn-, Cr-, and Fe-profiles along the arrow drawn in (a); (c) displays magnified P-, S-, Mn- and P-profiles shown in (b).

Figure 5-32 displays STEM-SI EDS data showing the distributions of Cr, Fe, Ni, Si, S, P, Nb, N and Mn at a high-angle grain boundary (HAGB) in the 347SS 18 dpa sample. In Figure 5-33a, an orange arrow (the frame highlights the width of the line) across the GB was drawn along which element profiles across the GB were extracted as shown in Figure 5-33b and Figure 5-33c. It clearly shows that enrichment in Ni, Si, P, S, and Nb and the deficit in Fe, Cr and Mn have been enhanced. Figure 5-34 displays STEM-SI EDS

data showing the distributions of Cr, Fe, Ni, Si, S, P, Nb, N and Mn at a twinned grain boundary (TB) in the 347SS 18 dpa sample. It also clearly shows that the TB enriches in Ni, Si, P and a little bit S and Nb and depletes in Fe, Cr and Mn.

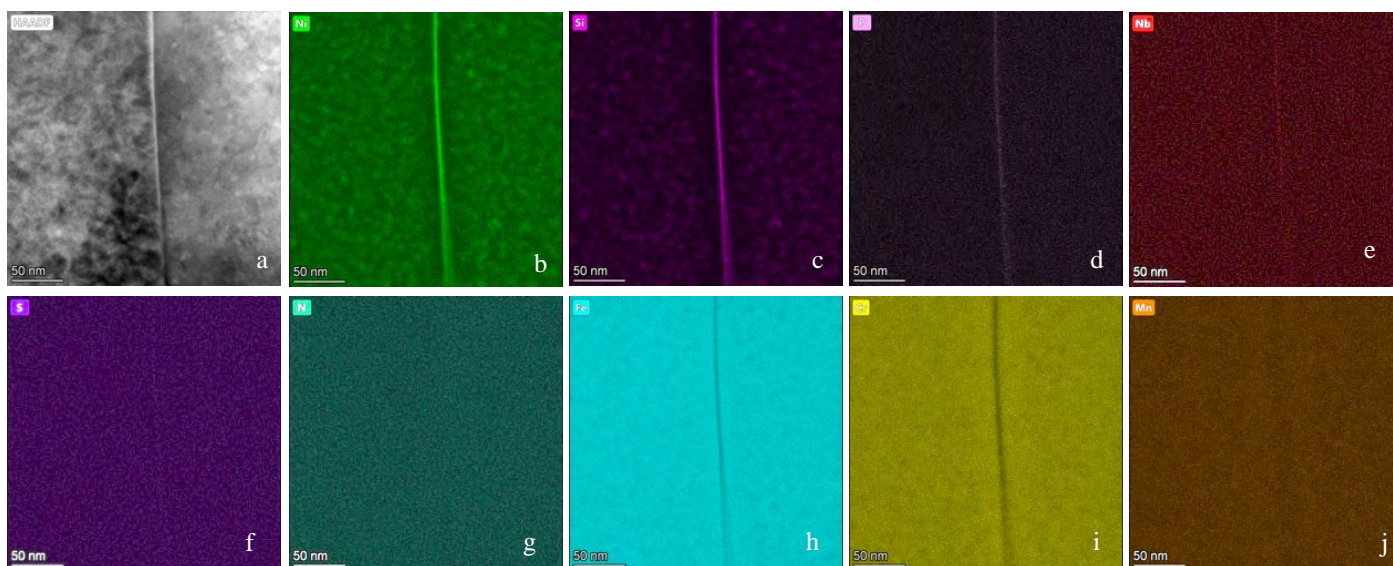


Figure 5-32: (a) STEM-BF image of a HAGB in the 18 dpa irradiated sample, (b)-(j) are Ni-, Si-, P-, Nb-, S-, N-, Cr-, Fe- and Mn -maps, respectively.

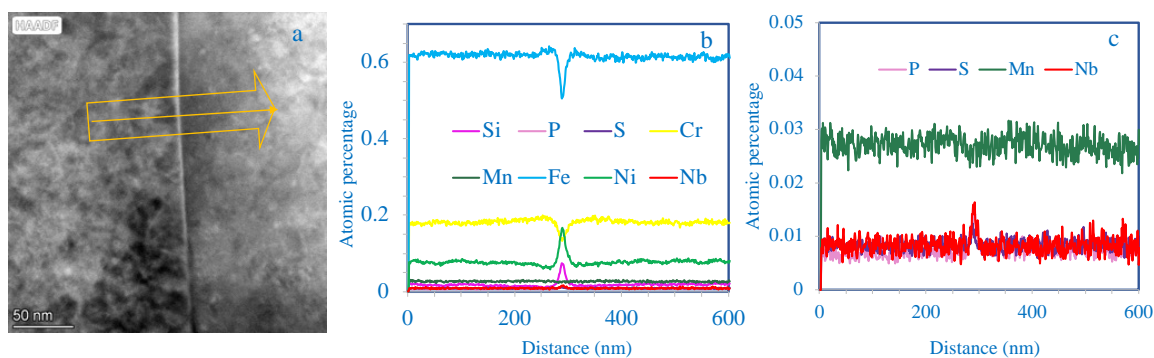


Figure 5-33: (a) STEM-BF image of a HAGB in the 18 dpa irradiated sample with an arrow drawn for element profiles; (b) displays Ni-, Si-, S-, P-, Nb-, N-, Mn-, Cr-, and Fe-profiles along the arrow drawn in (a); c) displays magnified P-, S-, Mn- and P-profiles shown in (b).

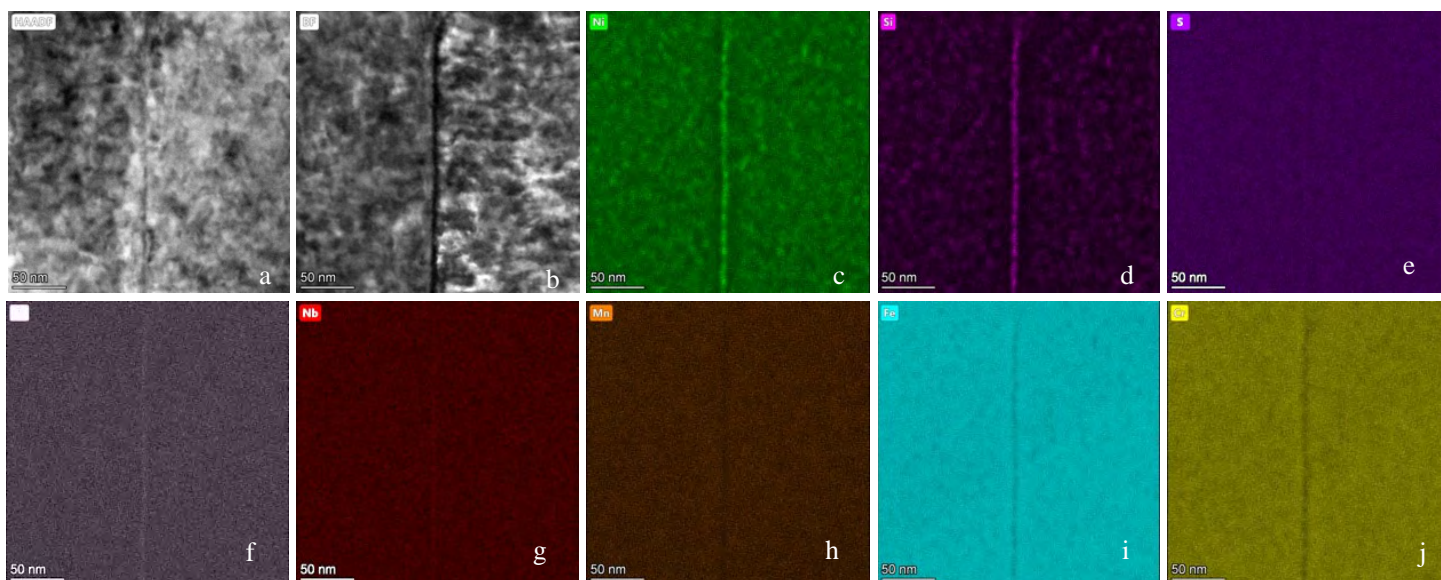


Figure 5-34: (a) and (b) are STEM-HAADF and BF images of a TB in the 18 dpa irradiated sample, (b)-(j) are Ni-, Si-, S-, P-, Nb-, Mn-, Fe- and Cr -maps, respectively.

Figure 5-35 displays STEM-SI EDS data showing the distributions of Cr, Fe, Ni, Si, S, P, Nb, and Mn maps at a HAGB in the 347SS 26 dpa sample. In Figures 3.35a, a yellow arrow (the frame highlights the width of the line) across the GB was drawn along which element profiles across the GB were extracted as shown in Figure 3.35b and Figure 3.35c. It also clearly shows that the enrichment in Ni, Si, P, S, and Nb and deficit in Fe, Cr and Mn at the HAGB have been largely enhanced.

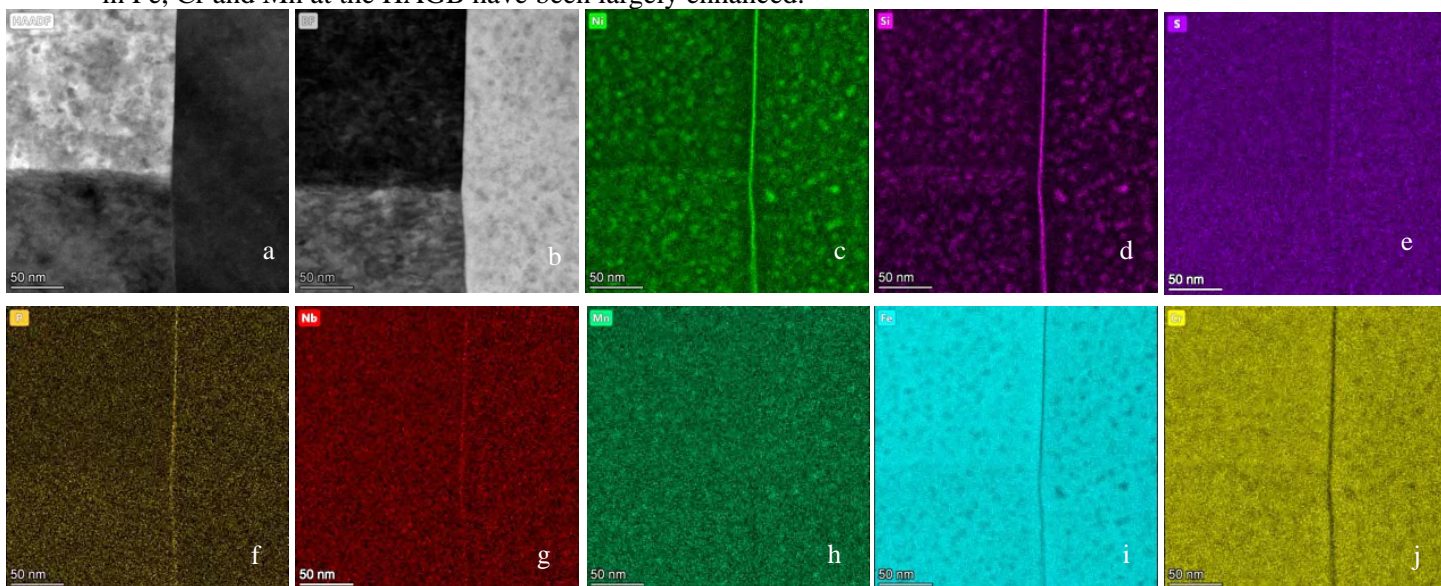


Figure 5-35: (a) and (b) STEM-HAADF and BF images of a HAGB in the 26 dpa irradiated sample, (c)-(j) are Ni-, Si-, S-, P-, Nb-, Mn-, Fe-, and Cr-maps, respectively.

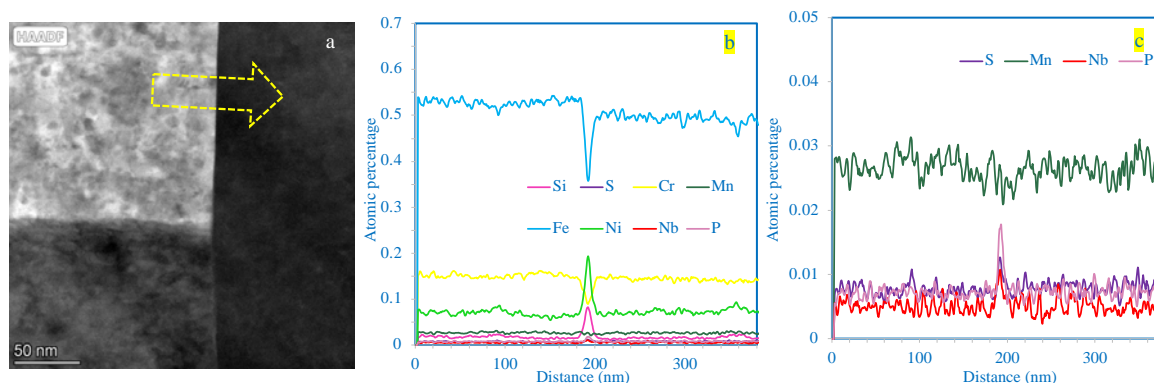


Figure 5-36: (a) STEM-HAADF image of a HAGB in the 18 dpa irradiated sample with an arrow indicating location of element profiles; (b) displays Ni-, Si-, S-, P-, Nb-, N-, Mn-, Cr-, and Fe-profiles along the arrow in (a); (c) displays magnified P-, S-, Mn- and P-profiles shown in (b).

5.5.4 Voids

Figure 5-37(a) –(c) are TEM bright-field (BF) images taken from the 347 alloy materials irradiated at 8 dpa, 16 dpa and 26 dpa, respectively. From the images, some voids showing bright contrast in the images are seen. The measured average size of the voids is 3.11 nm, 5.06 nm, and 7.21 nm, respectively, in the 8 dpa, 18 dpa and 26 dpa damaged samples. The number density of the voids in the three samples is $2.24 \times 10^{21}/\text{m}^3$, $2.44 \times 10^{21}/\text{m}^3$ and $1.85 \times 10^{21}/\text{m}^3$ for the 8 dpa, 18 dpa and 26 dpa samples, respectively.

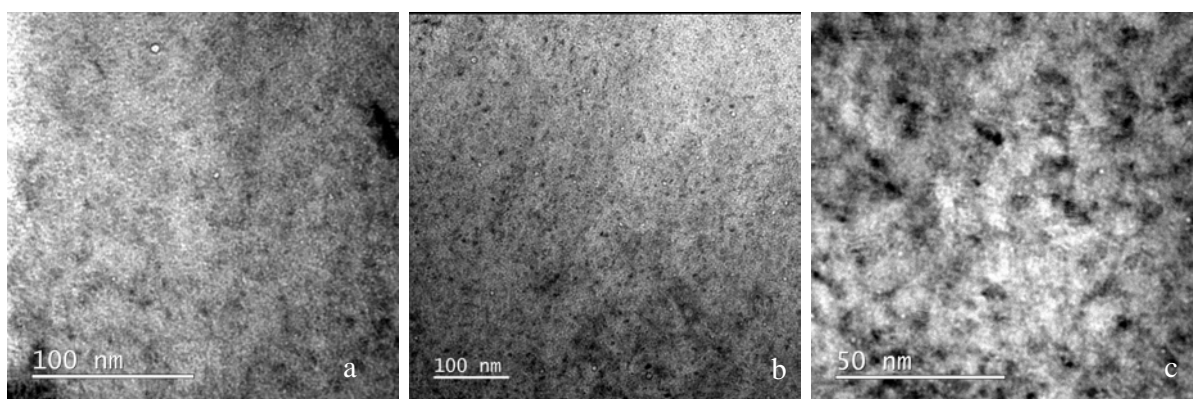


Figure 5-37: (a) –(c) BF images showing voids in 8 dpa, 18 dpa and 26 dpa irradiated samples, respectively.

Table 5-4: Summary of microstructures of neutron irradiated 347SS at different doses.

	Dislocation loops		Precipitates		Voids		Swelling	RIS (Compositions at the GBs, at.%)							
	Size (nm)	#x10 ² 2/m ³	Size (nm)	#x10 ² 2/m ³	Size (nm)	#x10 ² 1/m ³	%	Fe	Cr	Mn	Ni	Si	P	S	Nb
8 dpa	9.78	1.05	4.52	2.23	3.11	2.24	0.004%	54.4	13.5	2.7	13.9	5.5	1.1	0.8	0.8
18 dpa	9.03	2.33	7.03	2.78	5.06	2.44	0.017%	50.5	13.2	2.5	16.5	7.4	1.5	1.1	1.6
26 dpa	9.45	2.14	7.15	2.53	7.21	1.85	0.036%	35.7	8.9	2.6	19.3	8.2	1.7	1.3	1.1

5.6 MICROSTRUCTURE AND MICROCHEMISTRY OF IG CRACKS IN NEUTRON IRRADIATED AND STRAINED SAMPLES

5.6.1 Sample D28-H-1 (26.4 dpa in LiOH)

Figure 5-38 displays STEM-SI EDS data showing the distributions of Cr, Fe, Ni, O, and C maps of a region centering to a cracked GB in the 347SS 26.4 dpa damaged and strained in LiOH sample. The data indicate that the surface was oxidized forming large, isolated Fe(Ni)-rich oxide particles which might be the spinel phase and a continuous Cr-rich oxide layer with a Ni-rich oxide layer underneath.

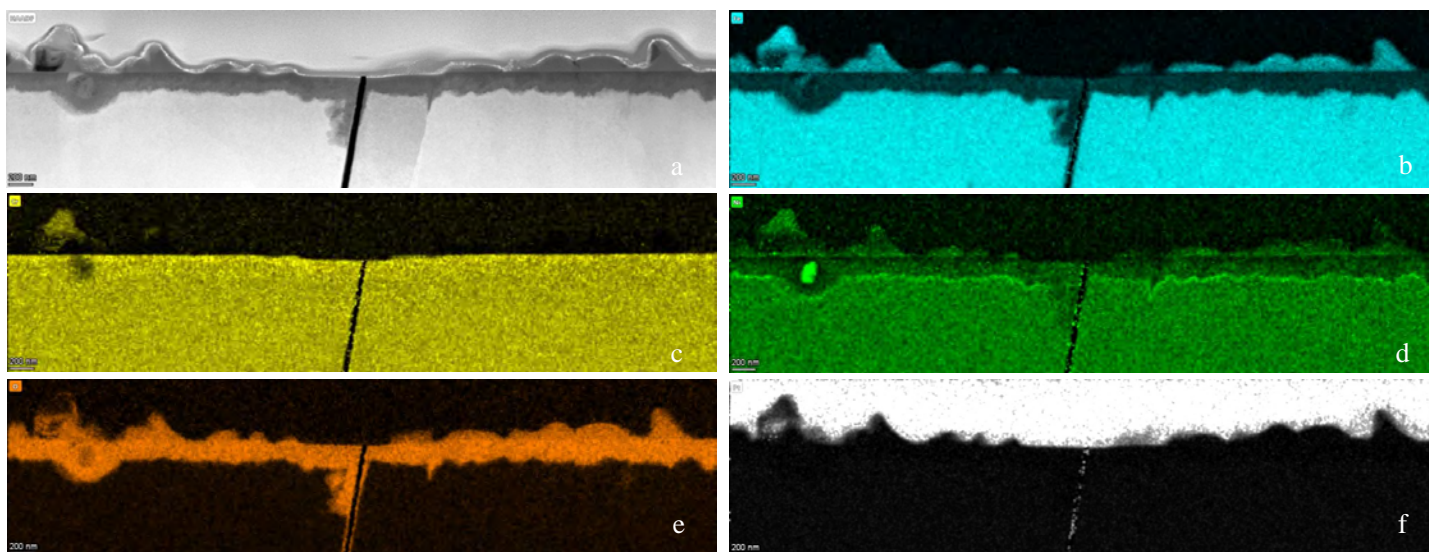


Figure 5-38: (a) is a STEM-HAADF image of a cracked GB in the 26.4 dpa irradiated and strained in LiOH sample, (b)-(f) are corresponding Fe-, Cr-, Ni-, O-, and C-maps, respectively.

Figure 5-39 displays STEM-SI EDS data showing the distributions of Cr, Fe, Ni, and O maps of a region centering to the top surface of the cracked GB (shown in also Figure 5-38) in the 347SS 26.4 dpa damaged and strained in LiOH sample. The data show that the GB was oxidized asymmetrically and the flanks of the cracked GB consist of island-like Fe(Ni)-rich spinel oxide particle layer and a thin Cr-rich layer followed by a Ni-rich oxide layer.

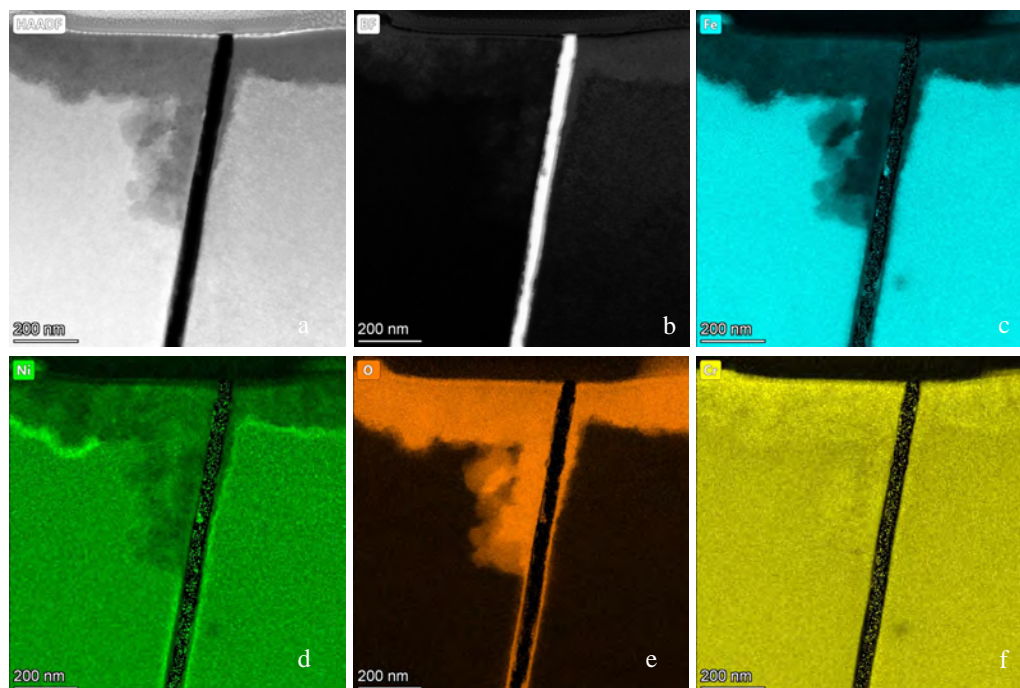


Figure 5-39: (a) and (b) are STEM-HAADF and BF images of the cracked GB shown in Figure 5-38 in the 26.4 dpa irradiated and strained in LiOH sample, (c)-(f) are corresponding Fe-, Ni-, O-, and Cr-maps, respectively.

Figure 5-40 displays STEM-SI EDS data showing the distributions of Cr, Fe, Ni, Si, P, Nb, S and O maps of the crack tip region of the cracked GB (shown in also Figure 5-38) in the 347SS 26.4 dpa damaged and strained in LiOH sample. The data shows that there is an enrichment in Ni at the crack tip and some Nb-rich precipitates nearby.

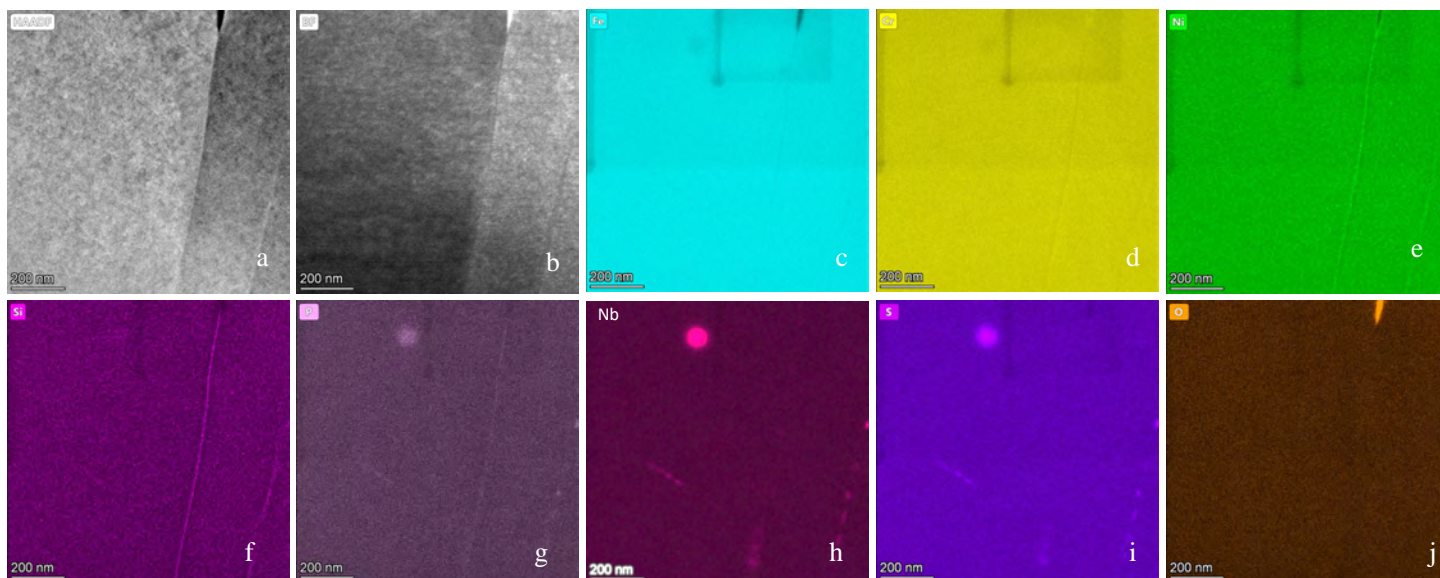


Figure 5-40: (a) and (b) are STEM-HAADF and BF images of the crack-tip region of the cracked GB shown in Figure 5-38 in the 26.4 dpa irradiated and strained in LiOH sample, (c)-(f) are corresponding Fe-, Cr-, Ni-Si-, P-, Nb-, S- and O-maps, respectively.

5.6.2 Sample D28-H-3 (26.4 dpa in KOH)

Figure 5-41 displays STEM-SI EDS data showing the distributions of Cr, Fe, Ni, O, and Nb maps of a region centering to a cracked GB in the 347SS 26.4 dpa damaged and strained in KOH sample. The data indicate that the surface was oxidized forming large, isolated Fe(Ni)-rich oxide particles which might be the spinel phase and a continuous Cr-rich oxide layer with a Ni-rich oxide layer underneath.

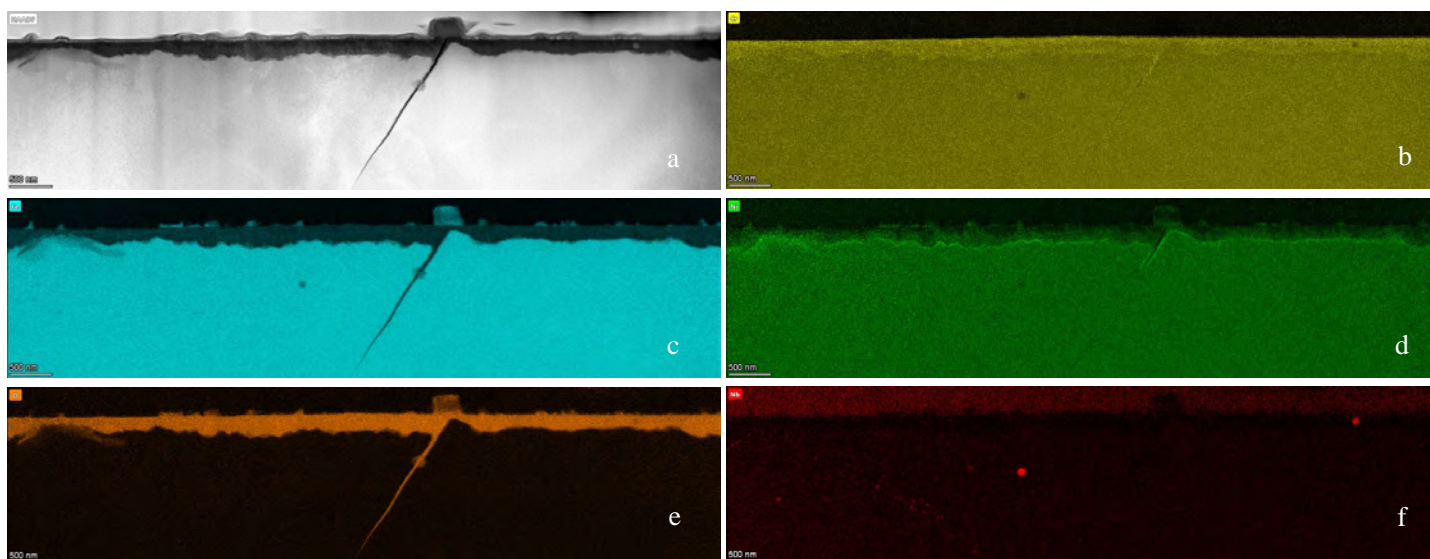


Figure 5-41: (a) is a STEM-HAADF image of cracked GB in the 26.4 dpa irradiated and strained in KOH sample, (b)-(f) are corresponding Cr-, Fe-, Ni-, O- and Nb-maps, respectively.

Figure 5-42 displays STEM-SI EDS data showing the distributions of Cr, Fe, Ni, and O maps of a region centering to the top surface of the cracked GB (shown in also Fig. 3.40) in the 347SS 26.4 dpa damaged and strained in KOH sample. The data show that the GB was oxidized asymmetrically and the oxidized surface and the flanks of the cracked GB consist of island-like Fe(Ni)-rich spinel oxide particle layer and a thin Cr-rich layer followed by a Ni-rich oxide layer.

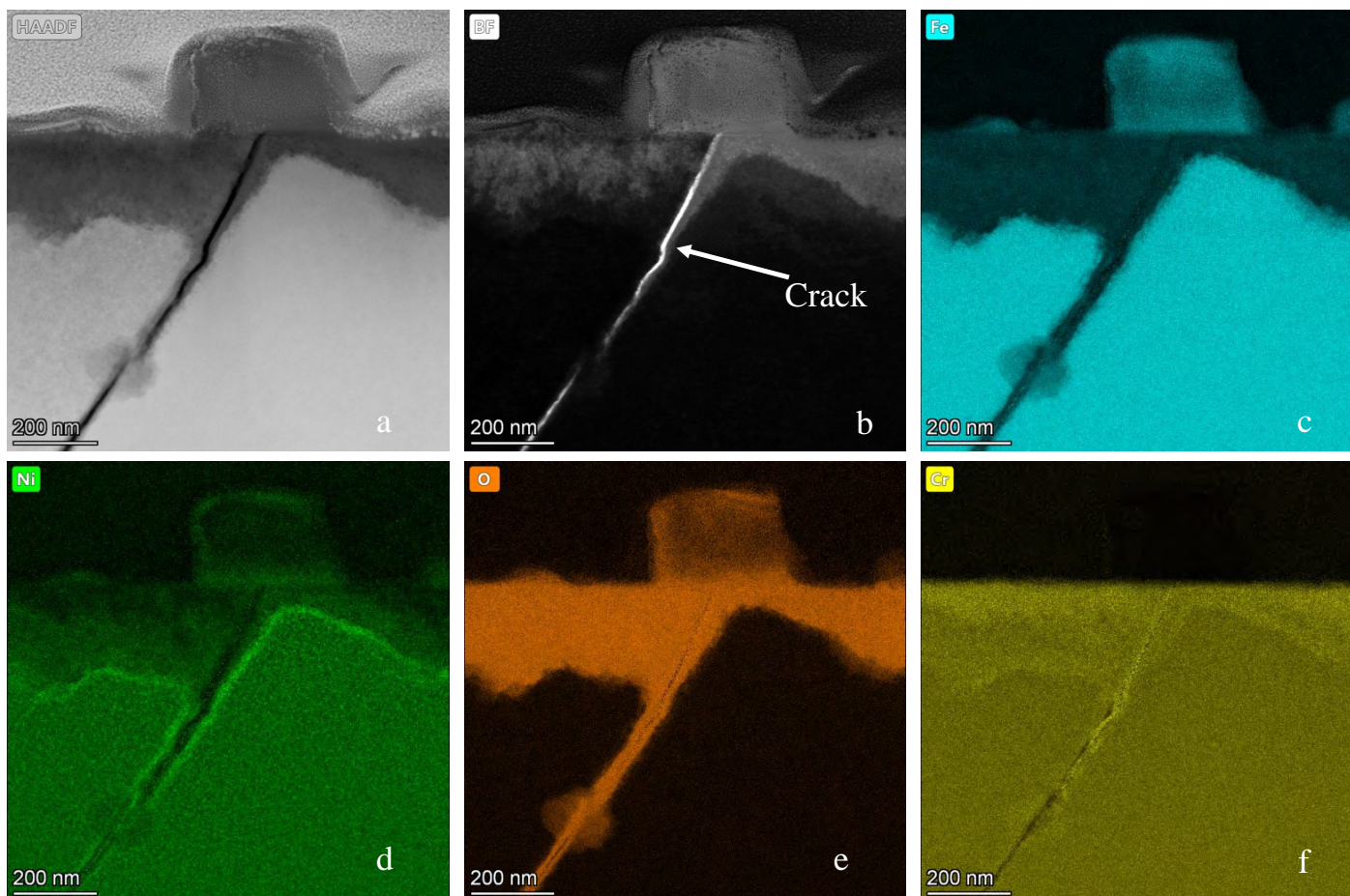


Figure 5-42: (a) and (b) are STEM-HAADF and BF images of the cracked GB shown in Fig. 19 in the 26.4 dpa irradiated and strained in KOH sample, (c)-(f) are corresponding Fe-, Ni-, O-, and Cr-maps, respectively.

Figure 5-43 displays STEM-SI EDS data showing the distributions of Cr, Fe, Ni, Si, and O maps of the crack tip region of the cracked GB (shown in also Fig. 3.40) in the 347SS 26.4 dpa damaged and strained in KOH sample. The data shows that there is an enrichment in Ni at the crack tip.

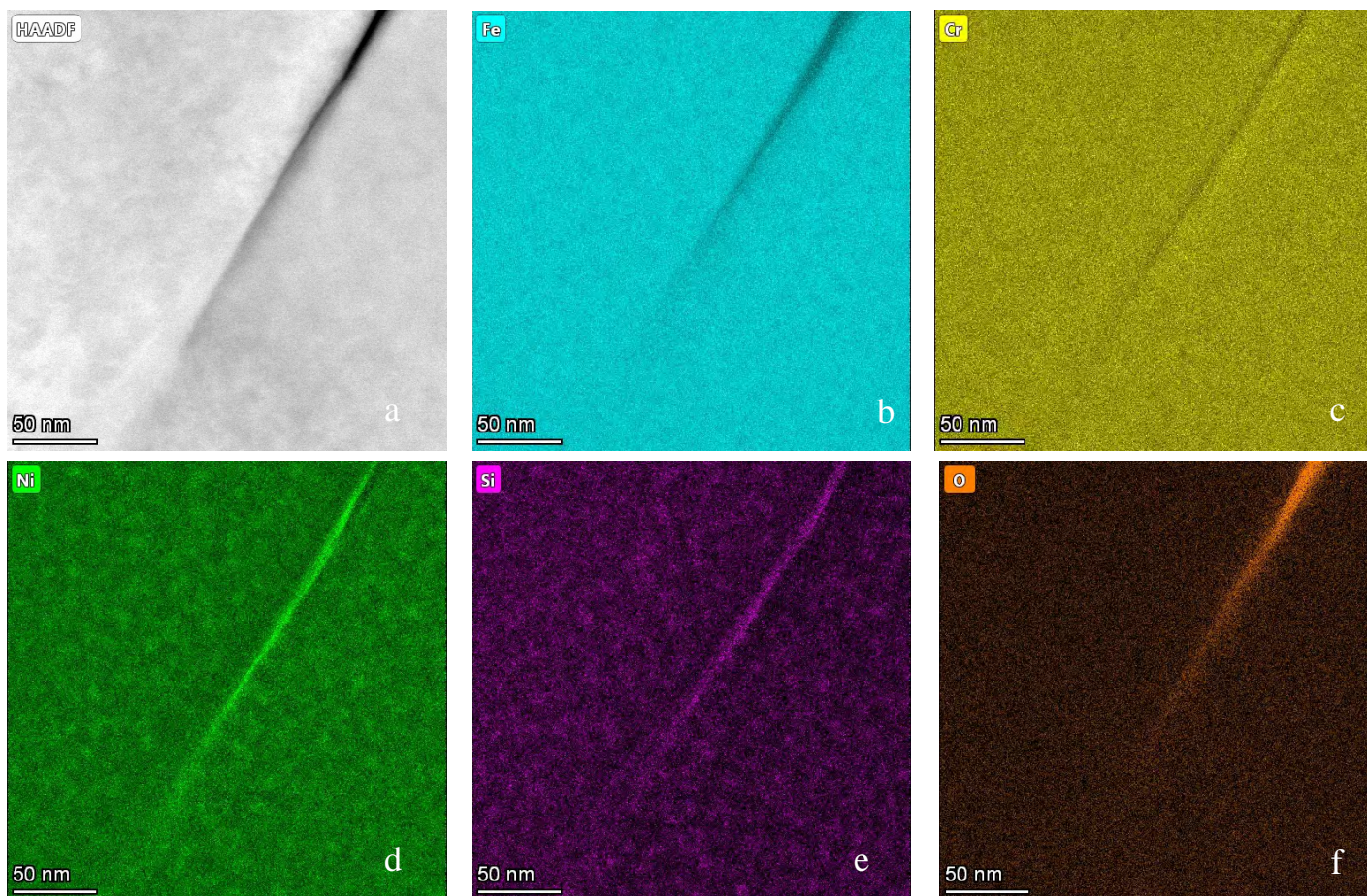


Figure 5-43: (a) is a STEM-HAADF image of the crack-tip region of the cracked GB shown in Fig. 19 in the 26.4 dpa irradiated and strained in KOH sample, (b)-(f) are corresponding Fe-, Cr-, Ni-, S- and O-maps, respectively.

Figure 5-44 displays STEM-SI EDS data showing the distributions of Cr, Fe, Ni, O, and Nb maps of another region centering to a cracked GB in the 347SS 26.4 dpa damaged and strained in KOH sample. The data indicate that the surface was oxidized forming large, isolated Fe(Ni)-rich oxide particles which might be the spinel phase and a continuous Cr-rich oxide layer with a Ni-rich oxide layer underneath. The data also shows that the crack stopped propagation at a Nb-rich precipitate before reaching the triple junction.

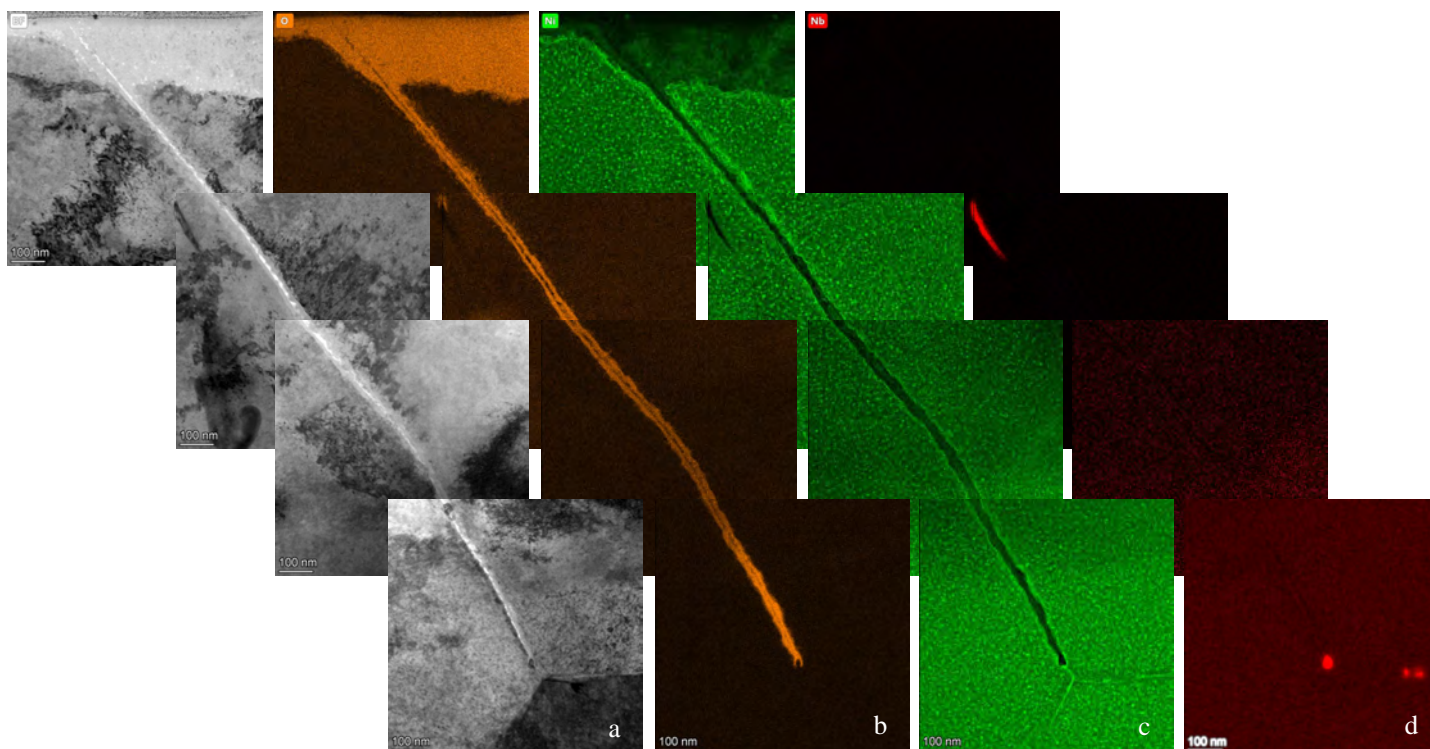


Figure 5-44: (a) is a series of STEM-BF images taken along a cracked GB in the 26.4 dpa irradiated and strained in KOH sample, (b)-(d) are corresponding series of O-, Ni- and Nb-maps, respectively.

Figure 5-45 displays STEM-SI EDS data showing the distributions of Cr, Fe, Ni, O, and Nb maps of a third region centering to a cracked GB in the 347SS 26.4 dpa damaged and strained in KOH sample. The data indicate that the surface was oxidized forming large, isolated Fe(Ni)-rich oxide particles which might be the spinel phase and a continuous Cr-rich oxide layer with a Ni-rich oxide layer underneath. The data also shows that the crack bypassed a Nb-rich precipitate and propagating deeply.

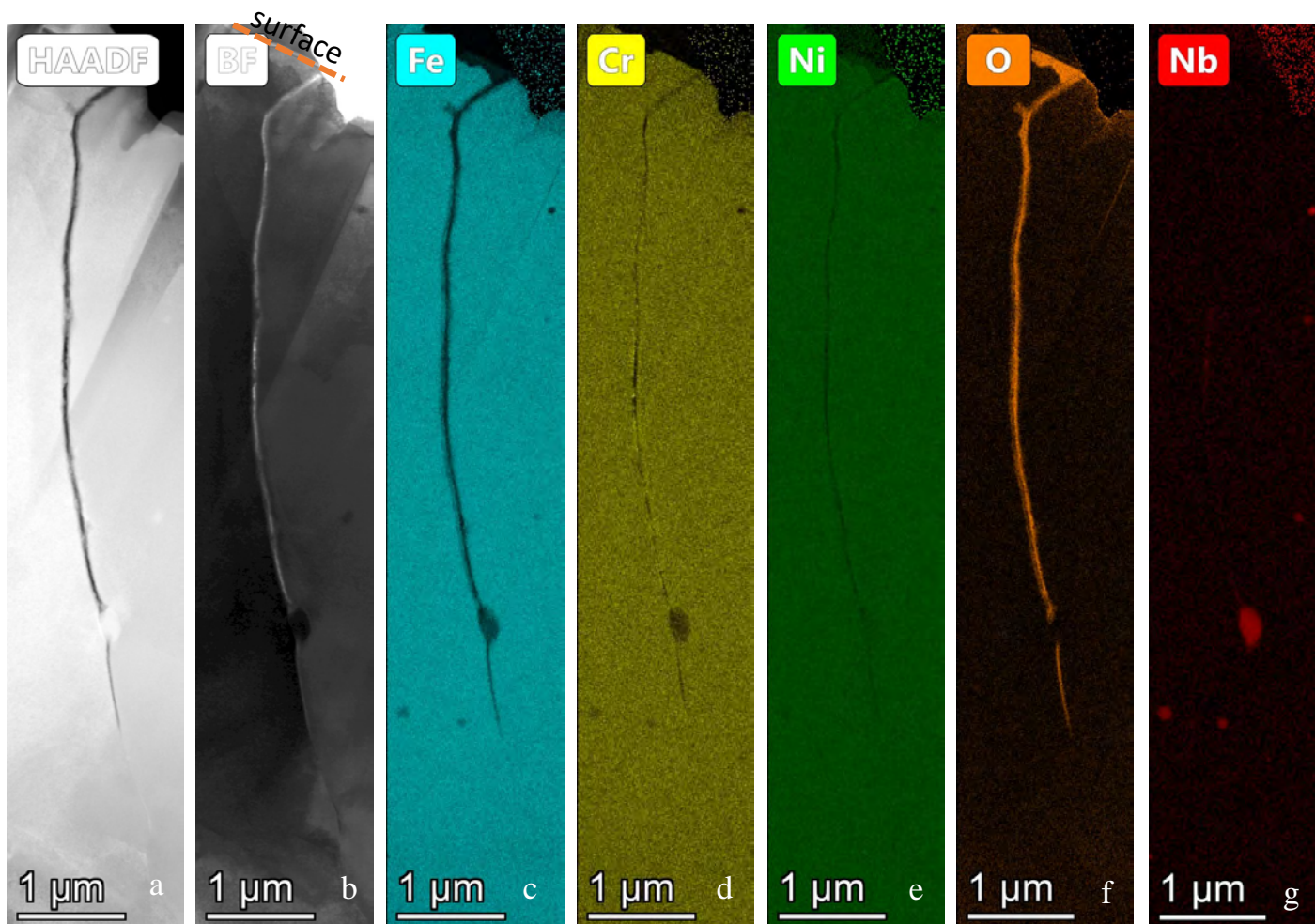


Figure 5-45: (a) and (b) are STEM-HAADF and BF images taken from a long-cracked GB in the 26.4 dpa irradiated and strained in KOH sample, (c)-(g) are corresponding series of Fe-, Cr-, Ni-, O-, and Nb-maps, respectively.

5.6.3 Sample S-R2C6-T-1 (7.8 dpa in KOH)

Figure 5-46 displays STEM-SI EDS data showing the distributions of Cr, Fe, Ni, and O maps of a region centering to the top surface of a cracked GB in the 347SS 7.8 dpa damaged and strained in KOH sample. The data show that the GB was oxidized asymmetrically and the oxidized surface consist of island-like Fe(Ni)-rich spinel oxide particle layer and a thin Cr-rich layer followed by a Ni-rich oxide layer. The flanks of the cracked GB also consist of island-like Fe(Ni)-rich spinel oxide particle layer and a thin Cr-rich layer followed by a Ni-rich oxide layer as can be seen from the element profile analysis of the cracked flanks (shown in Figure 5-47).

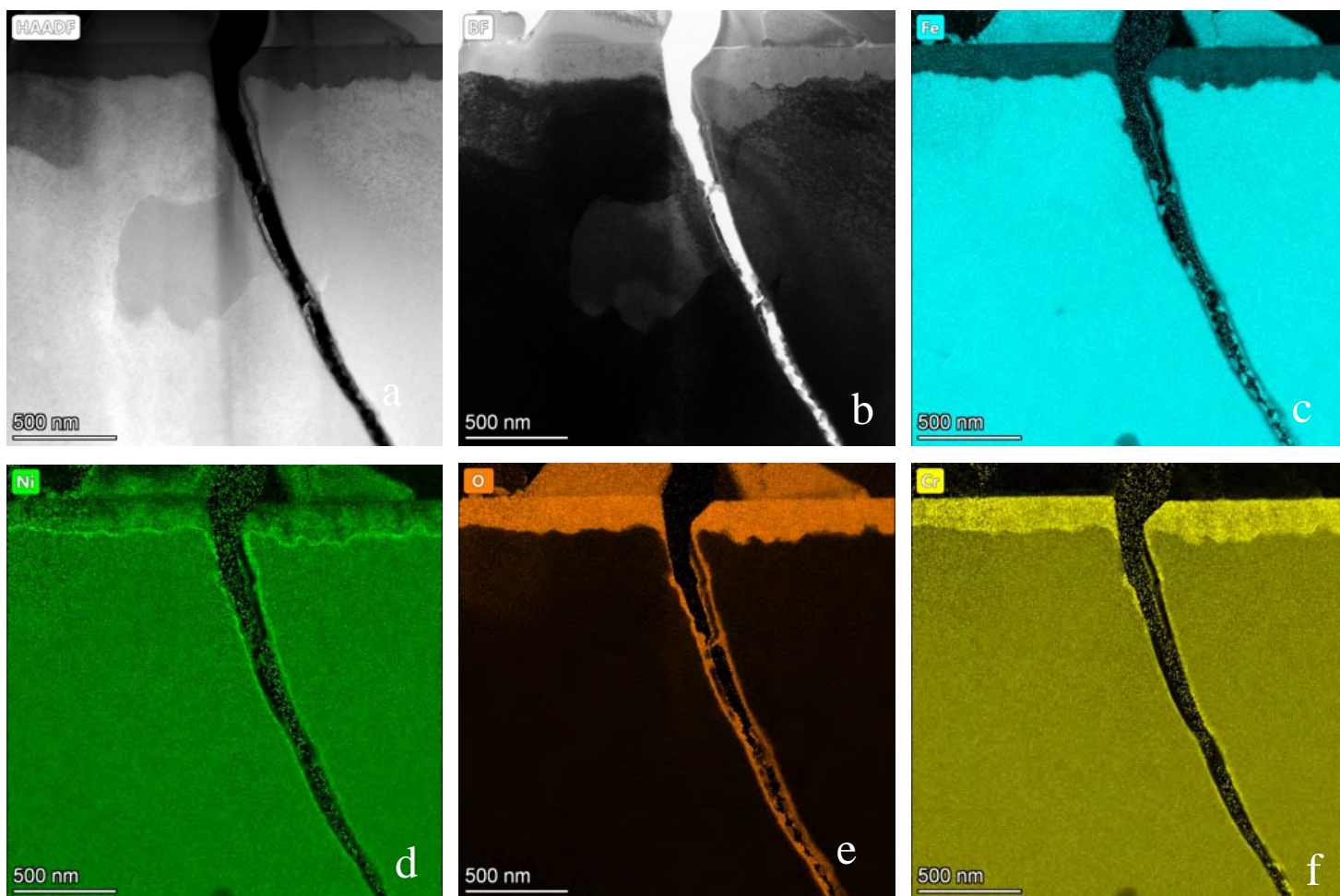


Figure 5-46: (a) and (b) are STEM-HAADF and BF images of a cracked GB in the 7.8 dpa irradiated and strained in KOH sample, (c)-(f) are corresponding Fe-, Ni-, O-, and Cr-maps, respectively.

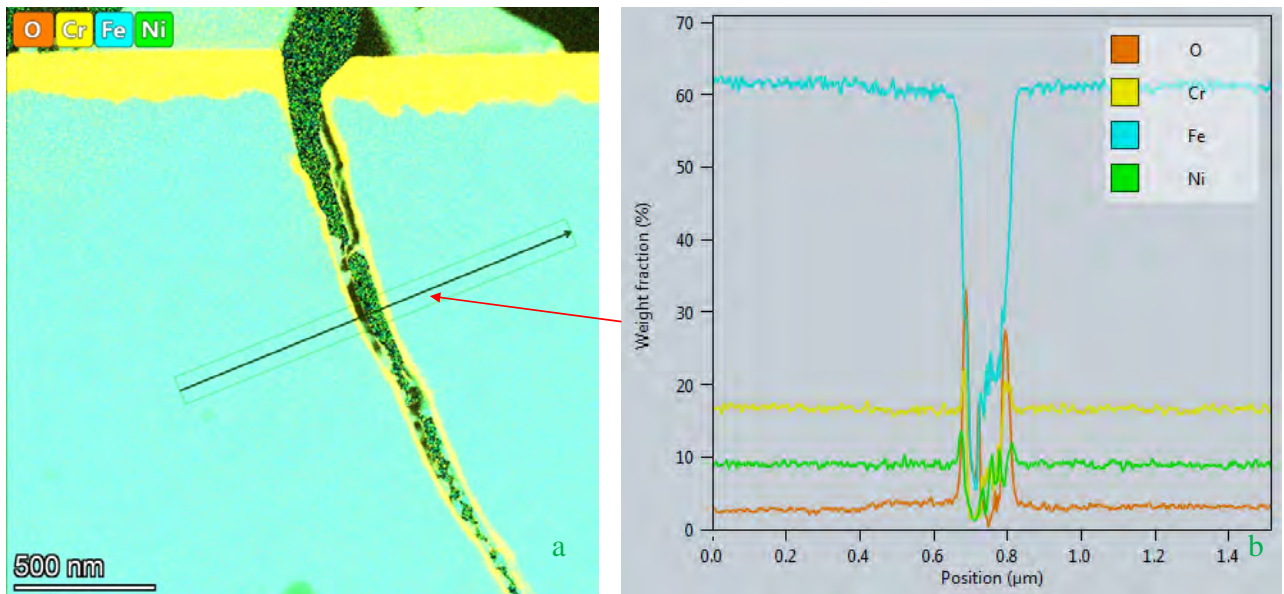


Figure 5-47: (a) are overlaid O-, Fe, Cr- and Ni-element maps of a cracked in the 7.8 dpa irradiated and strained in KOH sample with an arrow drawn for extracting element profiles along the arrow; (b) displays corresponding Fe-, Ni-, O-, and Cr-element profiles, respectively.

Figure 5-48 and Figure 5-49 display STEM-SI EDS data showing the distributions of Cr, Fe, Ni, O, and Nb maps of two regions centering to two long cracked GBs in the 347SS 7.8 dpa damaged and strained in KOH sample. The data indicate that the surface was oxidized forming large, isolated Fe(Ni)-rich oxide particles which might be the spinel phase and a continuous Cr-rich oxide layer with a Ni-rich oxide layer underneath. The data also shows that the crack could pass through a precipitate and continue propagating deeply.

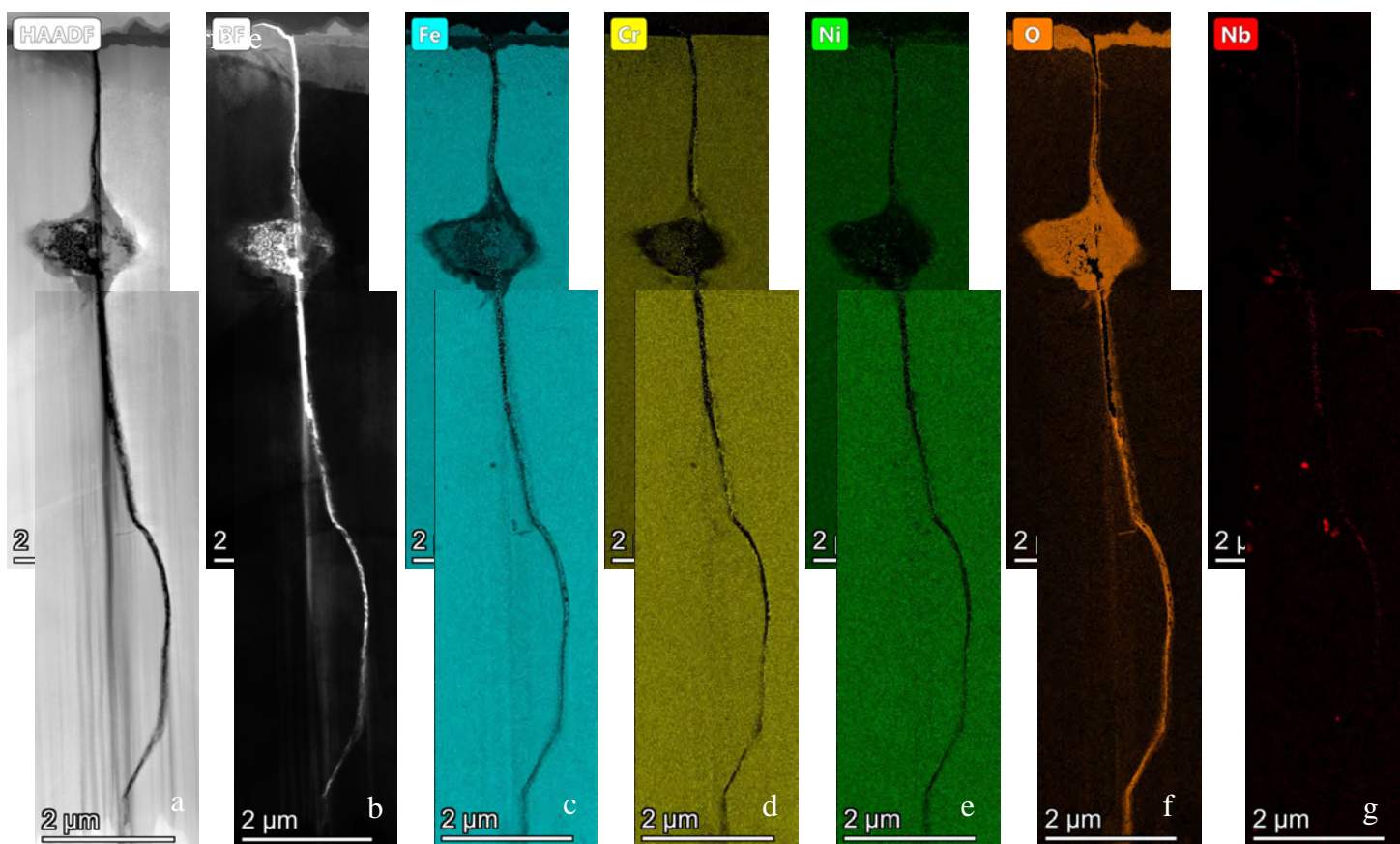


Figure 5-48: (a) and (b) are STEM-HAADF and BF images taken from a long-cracked GB in the 7.8 dpa irradiated and strained in KOH sample, (c)-(g) are corresponding series of Fe-, Cr-, Ni-, O-, and Nb-maps, respectively.

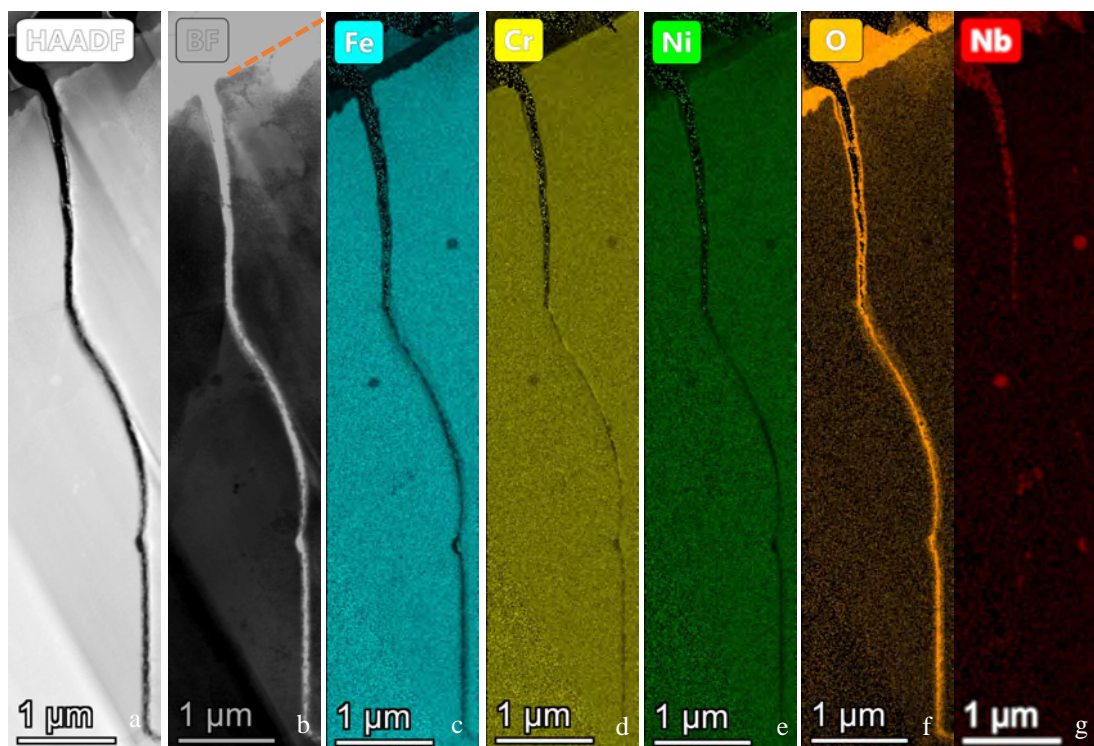


Figure 5-49: (a) and (b) are STEM-HAADF and BF images taken from a long-cracked GB in the 7.8 dpa irradiated and strained in KOH sample, (c)-(g) are corresponding series of Fe-, Cr-, Ni-, O-, and Nb-maps, respectively.

5.6.4 Sample S-R2C6-T-4 (7.8 dpa in LiOH)

Figure 5-50 and Figure 5-51 display STEM-SI EDS data showing the distributions of Cr, Fe, Ni, and O maps of two regions centering to the top surfaces of two long-cracked GBs in the 347SS 7.8 dpa damaged and strained in LiOH sample. The data show that the GB was oxidized asymmetrically and the oxidized surface consist of island-like Fe(Ni)-rich spinel oxide particle layer and a thin Cr-rich layer followed by a Ni-rich oxide layer. The flanks of the cracked GB also consist of island-like Fe(Ni)-rich spinel oxide particle layer and a thin Cr-rich layer followed by a Ni-rich oxide layer as can be seen from the element profile analysis of the cracked flanks (shown in Figure 5-47).

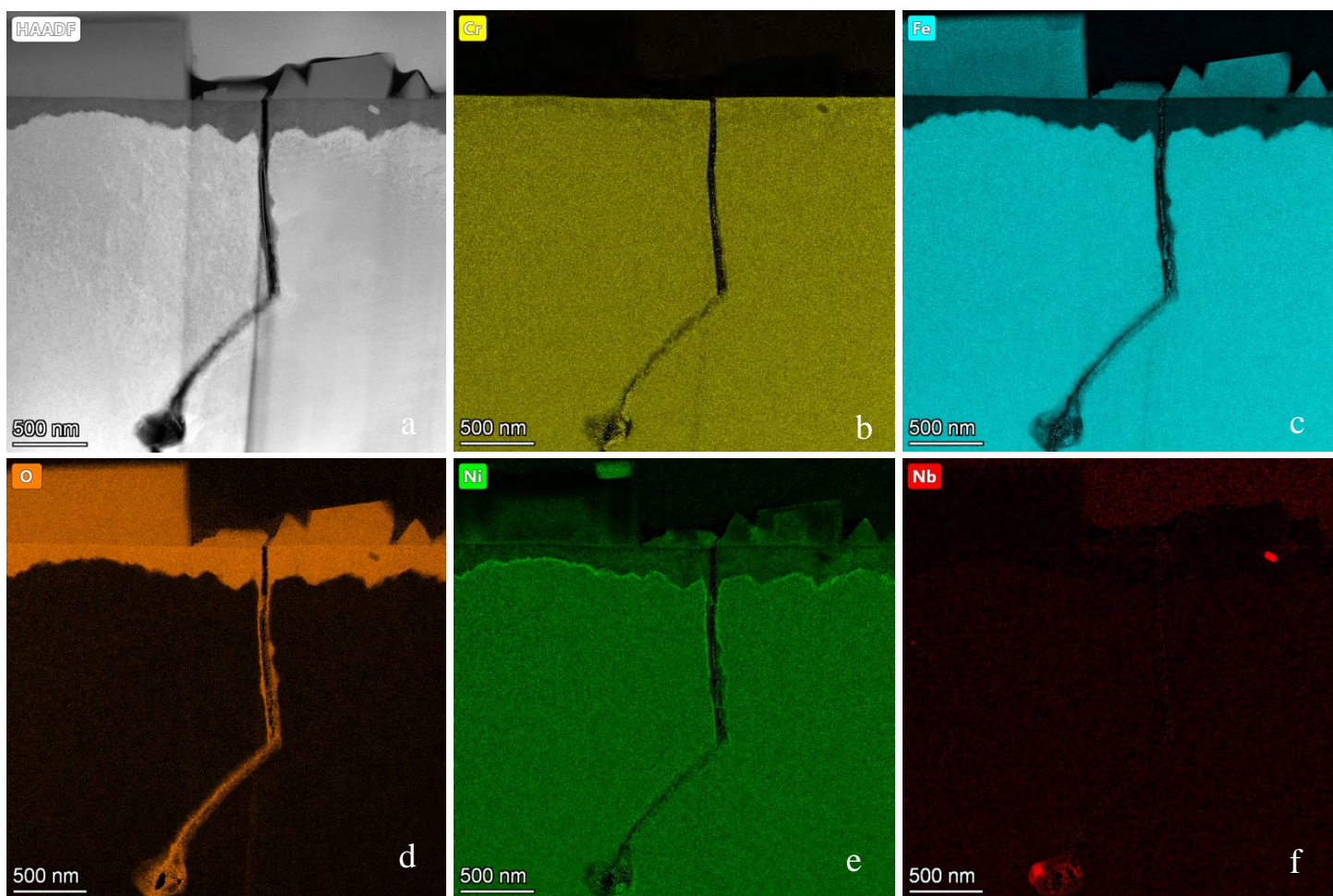


Figure 5-50: (a) is a STEM-HAADF of a cracked GB in the 7.8 dpa irradiated and strained in LiOH sample, (c)-(f) are corresponding Fe-, Ni-, O-, and Cr-maps, respectively.

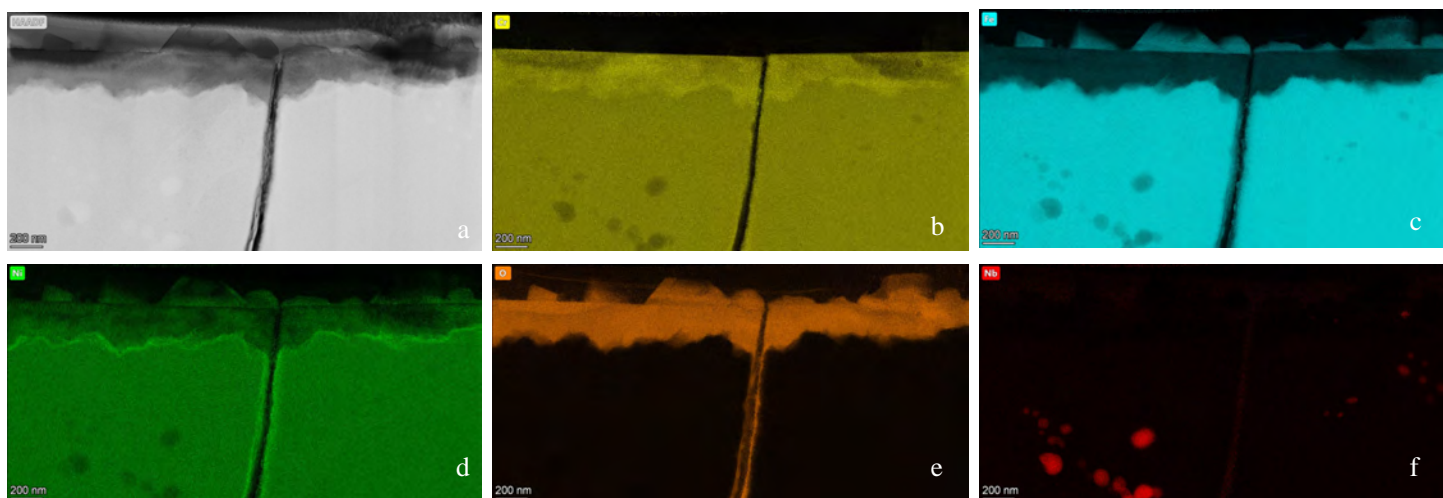


Figure 5-51: (a) is a STEM-HAADF of a cracked GB in the 7.8 dpa irradiated and strained in LiOH sample, (c)-(f) are corresponding Fe-, Ni-, O-, and Cr-maps, respectively.

Figure 5-52 displays STEM-SI EDS data showing the distribution of O of the region centering to a long-cracked GBs in the 347SS 7.8 dpa damaged and strained in LiOH sample. The data indicate the crack even could pass through a precipitate and propagating deeply.



Figure 5-52: (a) a STEM-HAADF image showing a long-cracked GB; and (b)~(e) are STEM-LAADF, BF, and HAADF images and O-map, respectively, taken from a long-cracked GB in the 7.8 dpa irradiated and strained in LiOH sample.

Results of the characterization of cracks on the four samples strained in KOH or LiOH are summarized in Table 5-5. In summary, the following can be stated:

- In the 8 dpa sample, RIS was observed in some HAGBs in which Ni, Si, S, P and Nb were enriched while Mn, Fe and Cr were depleted. There are some Ni-rich clusters with several nanometers in size. Nb-rich carbides were also observed in the sample, which have been partially amorphized.
- In the 18 dpa sample, more nanometer sized clustered enriched in Ni, Si and Mn were seen. RIS at HAGBs increased in magnitude.
- In the 26 dpa sample, many clusters enriched in Ni, Si, Mn and some S were observed. RIS induced Ni-, Si-, S-, P- and Nb- enrichments at HAGBs was greater. A large particle rich in Nb-, Ni-, P-, S- and Si was observed to be fully amorphized.
- Dislocations loops were seen together with some small voids in all the samples with different damage levels.

Table 5-5: Summary of cracked GBs studied in the neutron irradiated and strained Type 347 samples.

Samples	DPA	Environment	GB Labels	GB conditions	Cracked/Attacked GB Length (nm)
D28-H-1	26.4	LiOH	Loc.7x4	Cracked	~9700 vertical
			Loc. 7x4 new	Long-cracked	6450 along GB/6233 vertical
D28-H-3	26.4	KOH	Loc 24x7	Attacked/cracked	~500(attacked)/2800 (cracked)
			Loc 24x7- new	Cracked	2537(along GB) /2166 vertical
			Loc 12x3	Long cracked	2197(along GB)/1843 vertical
S-R2C6-T-1	7.8	KOH	Loc 31x6	Long cracked	5181 vertical
			Loc 33x5	Long cracked	6407 vertical
			Loc 35x4	Long cracked	12833 vertical
			Loc 35x6	Long cracked	12467 vertical
S-R2C6-T-4	7.8	LiOH	Loc 24x3	Long cracked	8613 vertical
			Loc 27x4	Long cracked	5905 vertical
			Loc 29x3	Long cracked	9176 vertical
			Loc 35x3	Long cracked	8351 vertical

6 DISCUSSION

6.1 EFFECT OF DAMAGE LEVEL AND ENVIRONMENT ON IASCC INITIATION

The initiation stress as a percent of the irradiated yield strength of the 347SS as a function of the irradiation damage (in dpa) and the environment (LiOH in blue, KOH in red) is shown in Figure 6-1. The results from the literature (References 15, 22, 23, 24) are plotted for comparison. It should be noted here that the data reported from the literature came from experiments conducted in simulated PWR environments with some variation in temperature (300 – 340°C) and water chemistry (boron concentration varied between 500 – 1200 ppm). Also, these data are from different types of initiation testing including O-ring, C-ring, and constant load tensile tests. This plot does not account for the exposure hours which is an important factor, for instance, many of O-ring and C-ring tests span several hours (less than 20 h) to several thousands of hours of exposure to the simulated environment which may affect the minimum stress to initiate IASCC. However, 80% of O-ring specimens that were going to fail did so within the first 150 hours of testing during tests that have run out to over 3900 hours (Reference 15). 150 hours is comparable to the exposure time at temperature of the 4-point bend specimens.

The only 4PB test data included in Figure 6-1 are that from this program. The literature data are mostly from Type 316 samples in the cold worked condition. Lastly, because the tests were conducted in discrete steps of 0.1YS, the stress to initiate a crack will lie somewhere between that at which it was observed, and the previous stress step, 0.1YS lower. Therefore, all 4PB data points are at the stress where cracks were first observed, with an error bar down to a value 0.1YS below that stress. The black dashed lines were constructed to represent the threshold of the minimum stress to initiate IASCC in the PWR environment.

It is evident from Figure 6-1 that the initiation stress tends to decrease with the damage level up to 10-20 dpa. The experiments in this project showed that the initiation stress plateaus at between 0.5YS and 0.6YS out to 26.4 dpa as no data in this study is available beyond that damage level. This is quite consistent with the literature data out through about 44 dpa.

As for the effect of water chemistry, the data are mostly indistinguishable. There were three repeatability tests performed. One in KOH at 11.5 dpa, two in LiOH at 18 dpa and 26.4 dpa. Of these three repeatability tests, the two in LiOH had exactly the same result for the stress a crack initiation and the KOH repeat tests differed by 0.2YS. Therefore, it was judged that results are generally repeatable.

Comparing results in KOH with that in LiOH, there was agreement on the crack initiation stress (within the error bounds of 0.1YS) in 5 cases and disagreement in two. One of these two was at 11.5 dpa and one at 26.4 dpa. In the 11.5 dpa case two tests were performed in KOH and one in LiOH. One KOH result and the LiOH result showed crack initiation between 0.7 and 0.8YS. The second KOH result showed crack initiation between 0.5 and 0.6YS. At 26.4 dpa, two tests in LiOH both exhibited crack initiation between 0.7 and 0.8YS and the one test in KOH initiated a crack between 0.5 and 0.6YS. As such, the results do not show any systematic difference between crack initiation stress in KOH and that in LiOH.

It should be noted that the high values of initiation stress at 26.4 dpa for the LiOH condition were not expected. However, it is known that significant data scatter can occur in IASCC initiation testing. For example, Reference 15 tested six identical O-ring samples cut from the same tube at 51 dpa and a constant load equivalent to 70% of the irradiated yield stress. Four of the specimens failed; two did not.

There are also several other variables which might have contributed to scatter in the data. One is that samples at this dose came from a BFB from a different PWR (Salem Unit 1) than those at the previous doses (D.C. Cook Unit 2). Despite the fact the PWRs are mostly similar in term of water chemistry and

operation conditions, there are numerous differences that could account for this result, including differing heats, bolt fabrication routes, reactor water chemistry, temperature, neutron spectrum, operating history, etc.

Substantial scatter also exists in the industry operating experience with baffle-former bolts. Data on operating experience with baffle-former bolts has been collected from inspection and replacement campaigns (References 25, 26, 27, and 28). Cracking does not always follow a clear dependence on dose and temperature. For example, it was found that some of BFBs were cracked at low dose and low temperature while others that are adjacent to these cracked BFBs and were exposed to similar operating conditions did not show any signs of cracks.

6.2 EFFECT OF MICROSTRUCTURE ON IASCC INITIATION

Crack initiation in irradiated stainless steels is believed to be triggered by high local stress caused by the termination of dislocation channels (DCs) at grain boundaries (Reference 19). In this work, the role of DCs was not directly observable due to the thick oxide film at the surface of all samples, which made the tracking process of these structural defects from lower loading steps to the initiation loading step convoluted. However, deformation bands or deformation twins were evident in these samples. DBs may also result in localized stress/strain at grain boundaries and it has been postulated that oxidation of these bands contributes to IASCC (Reference 29). Figure 5-16(b) shows the separation of GBs at the DBs-GBs intersection at which there is a greater amount of oxidation. The DBs may not only increase the localized stress at the GBs due to dislocation pile-up, but also act as preferential paths for oxygen diffusion to accelerate the oxidation process. The localized stresses at GBs resulting from the DBs may reach double the value of the macroscopic stress (References 30, 31) which would facilitate cracking.

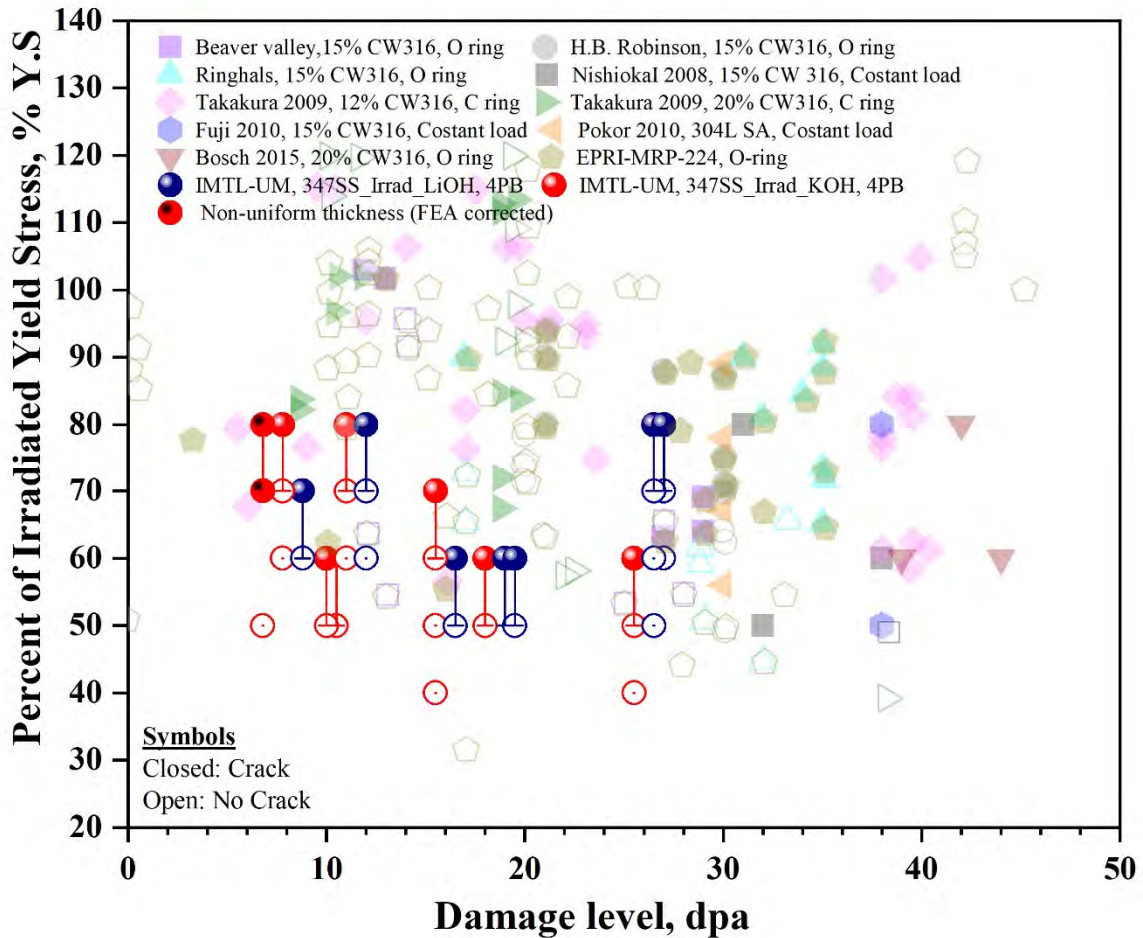


Figure 6-1: Stress as a percent of the irradiated yield strength versus displacement damage for crack initiation in austenitic stainless steels in PWR primary water environments. Data for 347SS in this study are offset along the abscissa to avoid overlap. The solid line is a power-law fit of this study data points and the dashed line is the literature data points.

6.2.1 IG cracking and GB oxidation

TEM images confirmed that the cracking morphology was IG in all samples in both LiOH and KOH. The cracks were mostly short and shallow and distributed at the strain uniform region indicating an early growth right after the initiation process. In case of samples with non-uniform thickness, some cracks were coalesced into one main crack as in sample S-R2C6-T1_7.8. The cracking characterization is summarized in Figure 6-2(a) shows the number of cracks and their number densities as a function of damage level in both water chemistries. It can be observed that there is no difference between KOH and LiOH conditions. Figure 6-2(b) shows the average crack lengths as a function of YS and no difference can be observed as well. Figure 6-2(c) shows the average crack lengths as a function of the damage level and the difference between the conditions cannot be observed though there is some kind of scatter in the data at higher damage level in both conditions. The scatters might be attributed to the heat-to-heat effect. Examining the data at 26.4 in LiOH system we can observe that at the same damage level and water chemistry there is 25 μm difference between the two samples.

The oxidation of grain boundaries at high temperature process is one of the most important factors in the degradation of the GBs (Reference 32). The average GB oxidation depth is usually correlated with the damage level indicating the promotion of GB oxidation due to irradiation (Reference 19). However, in this study no significant difference in the oxidation attack at GBs between the various damage levels is observed. This behavior is consistent with Fukumura et. al. (Reference 32) who showed that the GB oxidation process is similar between 3 and 73 dpa. The formation of the oxide along the GB usually reduces its strength (Reference 32). Fuji et al. (Reference 33) showed that the grain boundary strength of Alloy 600 grain boundaries was progressively degraded with increasing exposure time in PWR primary water. IASCC initiation test results from O-ring testing were found to be compatible with a mechanism of grain boundary oxidation and fracture (Reference 34). This finding was supported by examination of IASCC cracks in O-ring samples which identified evidence of grain boundary oxidation and oxide fracture similar to this work (Reference 35).

The grain boundary oxide is an Fe-Cr spinel; $\text{Fe}_x\text{Cr}_{3-x}\text{O}_4$ (FeCr_2O_4) which is brittle in nature and is believed to reduce the strength of the grain boundary when it forms. It also appears to be similar in both water chemistries indicating that the local environment condition within the crack is similar between the KOH and LiOH conditions. The images of GB cracks in the figures shown in section 5.6 clearly indicate that oxidation occurred well down the grain boundary – several micrometers – prior to cracking. That is, the tortuous crack path is evidence that oxide was present well before the cracking occurred and was not formed just ahead of the progressing crack tip. In the latter case, a smooth crack surface would be expected as opposed to the highly faceted surfaces shown here. Results also confirm that cracking is occurring in the oxide rather than at the oxide-metal interface, indicating that the interface strength is greater than that of the oxide.

In general, there was no evidence of any significant difference in cracking behavior between KOH and LiOH water chemistry. Similar results were concluded by crack growth tests in the literature. Studies of the crack initiation and growth of Alloy 600/182 have shown an indiscernible effect of KOH (Reference 36 and 37). Recently published results from an Electric Power Research Institute (EPRI) program (Reference 38) identified no effect of KOH vs. LiOH on crack initiation and growth of Alloy A286 (Reference 39) or on the crack initiation behavior of sensitized stainless steel (Reference 40). A more relevant investigation explored the effect of KOH water chemistry on crack growth behavior of irradiated stainless steels and concluded that there was no significantly measurable effect of KOH vs. LiOH on the crack growth rate (Reference 41) which is consistent with this study's conclusion.

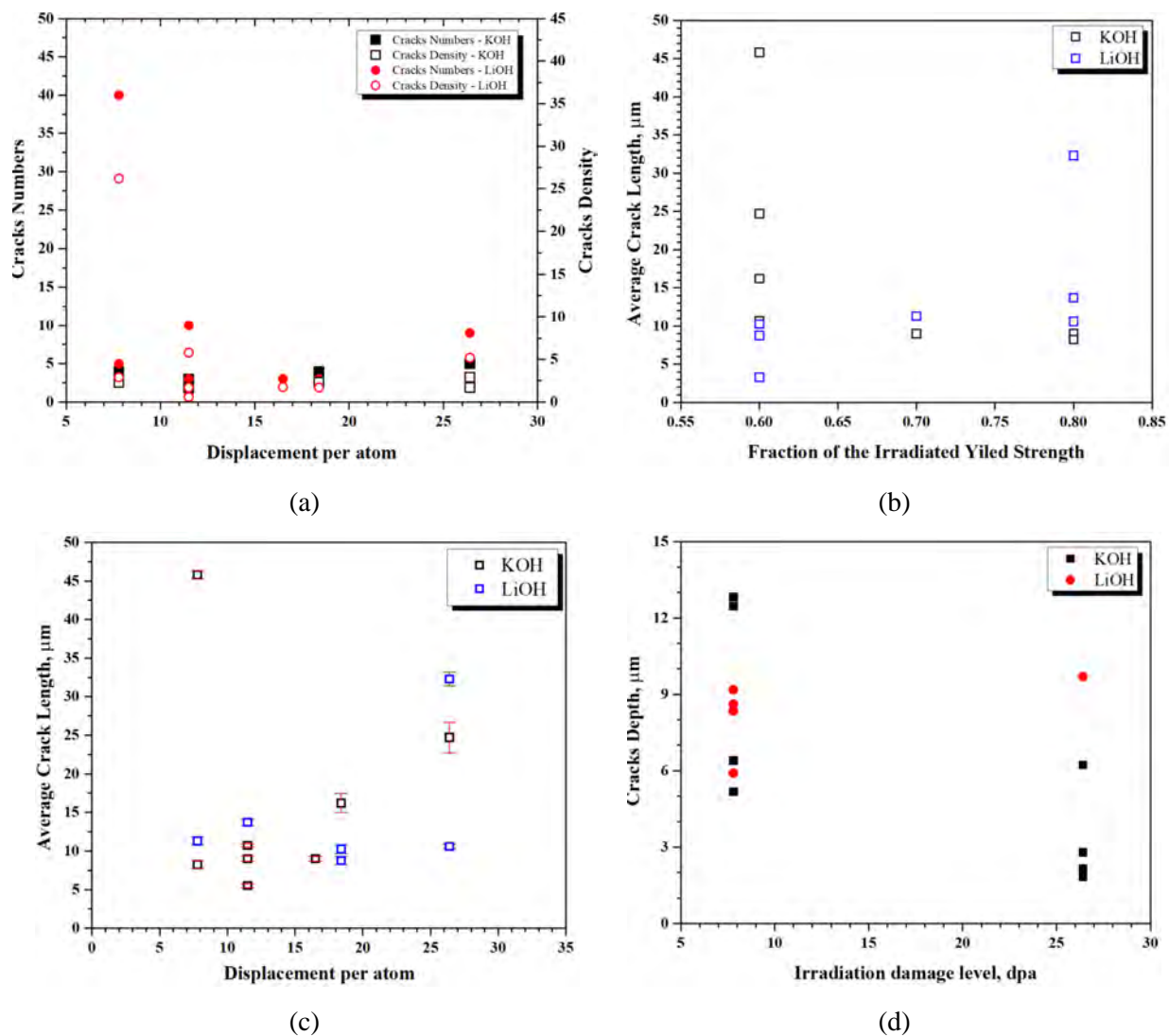


Figure 6-2: (a) Crack numbers and densities in both water chemistries, average length (b) as function of the damage level, (c) as a function of the fraction of the irradiated YS, and (d) the crack depth as a function of damage level.

7 CONCLUSIONS

This project was successful in completing its objectives and documents the most extensive IASCC initiation testing of neutron-irradiated Type 347 SS to date. The following are the major technical conclusions of the study:

- The minimum stress to initiate IASCC in the neutron-irradiated Type 347 SS was approximately 50% of the irradiated YS and was relatively insensitive of dpa and environment.
 - Assuming the miniature 4-point bend specimen results are comparable to results from other test methods, this value agrees well with the existing IASCC initiation data which are largely based on Type 316 SS.
 - No significant difference in IASCC initiation behavior is apparent between neutron irradiated Type 347 and Type 316 stainless steel.
- The cracking mechanism appeared to be similar in both KOH and LiOH water environments. Oxidation of grain boundaries was an important precursor to cracking in both environments.
 - This matches similar recent investigations into IASCC behavior of Type 316 stainless steel, indicating the IASCC mechanism is similar in neutron irradiated Type 347 and Type 316 stainless steel.
- No significant difference in IASCC initiation behavior was observed between the LiOH and KOH water chemistries. In addition to the points above, this conclusion is further supported by the observations that:
 - No statistically significant difference was observed in the minimum stress to initiate IASCC between LiOH and KOH.
 - There was no statistically significant difference in the crack length and depth between water chemistries.
 - No difference in the GB oxidation behavior down the crack tip was observed between water chemistries.

8 REFERENCES

1. Idaho National Laboratory Non-Proprietary User Agreement, User Facility Agreement No. 19-16567 between Battelle Energy Alliance, LLC and Westinghouse Electric Company, October 28, 2019.
2. Battelle Energy Alliance, LLC Contract No. 00231774, January 27, 2020.
3. Battelle Energy Alliance LLC Standard Research Contract No. 237485, June 24, 2020.
4. Westinghouse Technical Report RT-TR-20-42, "Fabrication of Miniature 4-point Bend Specimens for IASCC Initiation Testing," September 24, 2020.
5. Westinghouse Test Plan RT-TP-19-24, "Test Plan for NSUF Project 19-16567 Irradiation-assisted Stress Corrosion Cracking of PWR-irradiated Type 347 Stainless Steel," July 28, 2020.
6. Report from Office of Nuclear Reactor Regulation (NRR) Office, "Degradation of Baffle-former Bolts in Pressurized-Water Reactors," NRC ADAMS Accession Number ML16225A341, October 20, 2016. <https://www.nrc.gov/docs/ML1622/ML16225A341.pdf>
7. M. Ickes, J. McKinley, J.K. Lee, J. Smith, A. Ruminski, M. Burke, "Irradiation-assisted stress corrosion cracking of Type 347 and Type 316 steels irradiated in commercial pressurized water reactors," Journal of Nuclear Materials, Volume 536, 1 August 2020. <https://doi.org/10.1016/j.jnucmat.2020.152182>
8. U.S. Government Accountability Office Report, GAO-13-716, "Managing Critical Isotopes: Stewardship of Lithium-7 Is Needed to Ensure a Stable Supply," October 17, 2013. <https://www.gao.gov/products/GAO-13-716>
9. Effect of Boron Concentration on Alloy 690 Corrosion Product Release Rates -Results at 325°C and 285°C. EPRI, Palo Alto, CA: 2001. 1011744. <https://www.epri.com/#/pages/product/1011744/?lang=en-US>
10. J.K. McKinley, R.G. Lott, J.B. Hall, K. Kalchik, "Examination of Baffle-former Bolts from D.C. Cook Unit 2," 16th International Conference on Environmental Degradation of Materials in Nuclear Power Systems – Water Reactors, August 11-15, 2013, Asheville, North Carolina, USA.
11. ASTM A193-66, "Standard Specification for Alloy-steel Bolting Materials for High Temperature Service," ASTM International, 1966.
12. M. Ickes, J. McKinley, C. Cmar, K. Amberge, J. Smith, "Hot Cell Failure Analysis of Thermal Shield Support Block Bolts and Baffle-former Bolts from a US 4-loop PWR," Fontevraud 10 Conference: Contribution of Materials Investigations and Operating Experience to Light Water NPPs' Safety, Performance and Reliability, 19 – 22 September 2022 Avignon, France.
13. Materials Reliability Program: Hot Cell Testing of Baffle/Former Bolts Removed from Two Lead PWR Plants (MRP-51), EPRI, Palo Alto, CA: 2001. 1003069. <https://www.epri.com/#/pages/product/000000000001003069/?lang=en-US>
14. Oak Ridge National Laboratory Report ORNL/TM-2019/1251, "Post-Irradiation Examination of High Fluence Baffle-Former Bolts Retrieved from a Westinghouse Two-Loop Downflow Type PWR," July 2019.

15. Materials Reliability Program: Characterizations of Type 316 Cold Worked Stainless Steel Highly Irradiated Under PWR Operating Conditions (International IASCC Advisory Committee Phase 3 Program Final Report) (MRP-214). EPRI, Palo Alto, CA and the International IASCC Advisory Committee: 2007. 1015332.
<https://www.epri.com/#/pages/product/000000000001015332/?lang=en-US>
16. Materials Reliability Program Determination of Operating Parameters of Extracted Bolts (MRP-52), EPRI, Final Report, 2001.
17. ASTM E112-13, “Standard Test Methods for Determining Average Grain Size,” ASTM International, 2013.
18. ASTM Standard B912-02, “Standard Specification for Passivation of Stainless Steels Using Electropolishing,” American Society of Testing and Materials International, 2018
19. Kale J. Stephenson and Gary S. Was, “The Role of Dislocation Channeling in IASCC Initiation of Neutron Irradiated Stainless Steel,” *Journal of Nuclear Materials* 481, 214-225, September 128, 2016. <http://dx.doi.org/10.1016/j.jnucmat.2016.09.001>.
20. G.W. Hollenberg, G.R. Terwilliger, R.S. Gordon, Calculation of Stresses and Strains in Four-Point Bending Creep Tests, *Journal of the American Ceramic Society*, 54 (1971) 196 – 199.
21. D. Du, K. Sun, G.S. Was, IASCC of neutron irradiated 316 stainless steels to 125 dpa, *Materials Characterization*, 173 (2021) 110897.
22. R.W. Bosch, M. Vankeerberghen, R. Gérard, F. Somville, Crack initiation testing of thimble tube material under PWR conditions to determine a stress threshold for IASCC, *Journal of Nuclear Materials*, 461 (2015) 112121.
23. H. Nishioka, K. Fukuya, K. Fuji, T. Torimaru, IASCC Initiation in Highly Irradiated Stainless Steels under Uniaxial Constant Load Conditions, *Journal of Nuclear Science and Technology*, 45 (2008) 1072-1077.
24. Materials Reliability Program: Characterizations of Type 316 Cold-Worked Stainless Steel Highly Irradiated Under PWR Operating Conditions (MRP-73), EPRI, Final Report, 2002.
25. EPRI Letter MRP 2014-009, “Biennial Report of Recent MRP-227-A Reactor Internals Inspection Results,” May 12, 2014. <https://www.nrc.gov/docs/ML1522/ML15223A460.pdf>
26. EPRI Letter MRP 2016-008, “Biennial Report of MRP-227-A Reactor Internals Inspection Results,” May 18, 2016. <https://www.nrc.gov/docs/ML1614/ML16144A789.pdf>
27. EPRI Letter MRP 2018-025, “2018 Biennial Report of Recent MRP-227-A Reactor Internals Inspection Results” July 19, 2018. <https://www.nrc.gov/docs/ML1820/ML18204A161.pdf>
28. EPRI Letter MRP 2020-015, “2020 Biennial Report of Recent MRP-227-A Reactor Internals Inspection Results,” August 14, 2020, <https://www.nrc.gov/docs/ML2022/ML20229A000.pdf>
29. S. Lozano-Perez, T. Yamada, T. Terachi, M. Schroder, C.A. English, G.D.W. Smith, C.R.M. Grovenor, B.L. Eyre, Multi-scale characterization of stress corrosion cracking of cold-worked stainless steels and the influence of Cr content, *Acta Materialia* 57 (2009) 5361-5381.

30. K. Fukuya, H. Nishioka, K. Fuji, T. Miura, Y. Kitsunai, Local strain distribution near grain boundaries under tensile stresses in highly irradiated SUS316 stainless steel, *Journal of Nuclear Materials* 432 (2013) 67 – 71.
31. M. Kamaya, Y. Kawamura, T. Kitamura, Three-dimensional local stress analysis on grain boundaries in polycrystalline material, *International Journal of Solids and Structures* 44 (2007) 3267 – 3277.
32. T. Fukumura, K. Fukuya, K. Fujii, T. Miura, Y. Kitsunai, Grain boundary oxidation of neutron irradiated stainless steels in simulated PWR water, in: *Proceedings of the 18th International Conference on Environmental Degradation of Materials in Nuclear Power Systems—Water Reactors*, Springer, 2019, pp. 2153-2163.
33. K. Fujii, T. Miura, H. Kishkoka, K. Fukuya, Degradation of grain boundary strength by oxidation in alloy 600, *Proc. 15th International Conference on Environmental Degradation of Materials in Nuclear Power Systems – Water Reactors*, TMS, 2011, pp. 1447-1461.
34. M.J. Konstantinovic, Internal oxidation and probabilistic fracture model of irradiation assisted stress corrosion cracking in stainless steels, *Journal of Nuclear Materials*, 495 (2017) 220 - 224. <http://dx.doi.org/10.1016/j.jnucmat.2017.08.018>.
35. A.G. Penders, M.J. Konstantinovic , T. Yang, R.-W. Bosch, D. Schryvers, F. Somville, “Microstructural investigation of IASCC crack tips extracted from thimble tube O-ring specimens,” *Journal of Nuclear Materials* 565 (2022), <https://doi.org/10.1016/j.jnucmat.2022.153727>
36. PWR Primary Chemistry KOH Qualification: Materials Testing: Alloy 600 and Alloy 182 Crack Growth, EPRI, Final Report, 2021.
37. PWR Primary Chemistry KOH Qualification: Materials Testing: Alloy 600 Crack Initiation, EPRI, Final Report, 2019.
38. K. Fruzzetti, P. Chou, D. Hussey, D. Perkins, “Potassium Hydroxide for PWR Primary Coolant pH Control: EPRI Program,” in: *Proceedings of the 20th International Conference on Environmental Degradation of Materials in Nuclear Power Systems—Water Reactors*, July 17-21, 2022.
39. P. Andresen, P. Chou, “SCC Initiation and Growth Rate Response of A-286 in B/Li and B/K Solutions 340°C,” in: *Proceedings of the 20th International Conference on Environmental Degradation of Materials in Nuclear Power Systems—Water Reactors*, July 17-21, 2022.
40. S. Medway, P. Chou, D. Tice, “Comparing Stress Corrosion Cracking Initiation Times of Sensitized 304 Stainless Steel in KOH And LiOH Primary Water Chemistries with High Levels of Dissolved Oxygen,” in: *Proceedings of the 20th International Conference on Environmental Degradation of Materials in Nuclear Power Systems—Water Reactors*, July 17-21, 2022.
41. K. Chen, M. Ickes, M. Burke, G. Was, “The effect of potassium hydroxide primary water chemistry on the IASCC behavior of 304 stainless steel,” *Journal of Nuclear Materials*, Volume 558, 2022. <https://doi.org/10.1016/j.jnucmat.2021.153323>